THE DUAL EMA-FEM APPROACH TO DYNAMIC ANALYSIS

Steven Robert Grobler

A dissertation submitted to the Faculty of Engineering, University of the Witwatersrand, Johannesburg, in fulfillment of the requirements for the degree of Master of Science in Engineering

Johannesburg, 1990

Declaration

I declare that this dissertation is my own, unaided work. It is being submitted for the degree of Master of Science in Engineering in the University of the Witwatersrand, Johannesburg. It has not been submitted before for any degree or examination in any other University.

S. Grobler

6th day of September 1990

Abstract

It has been said that experimental modal analysis (EMA) "grew to prominence because the engineering community was incapable of properly analyzing the dynamics of commercially significant structures" [24]. The advent of powerful theoretical methods, such as the Finite Element Method (FEM) has not, however, resulted in the demise of EMA. In fact both FEM and EMA have undergone rapid growth and the merging of the two into an effective design and diagnostic tool has had a major impact on the engineering community's approach to dynamics related problems. In this study, the term *dual* has no mathematical connotations and is used to describe the complementary use of the techniques of EMA and FEM. The mining industry, worldwide, has experienced dynamics related problems in the operation of conveyances in vertical shafts. A study undertaken in South Africa investigated the behaviour of shaft steelwork and skips, resulting in a set of design guidelines for future shaft steelwork designs. This work only investigated the dynamic behaviour of skips. In this project, the ABAQUS and MODEL SOLUTION FEM codes were used to construct models of a mine cage. An impact modal test was carried out on the cage, using a GenRad 2515 CAT system. An impact hammer, suitable for exciting large structures, and a strain gauge force transducer were designed and built for the purpose of the test. The natural frequencies and mode shapes obtained from both FEM and EMA are compared by means of the modal assurance criterion (MAC). The test data is used to tune the model to produce accurate results. The model could then be used (with minimal further test work) for predicting the response of the structure to dynamic loading or the effects of structural modifications.

Acknowledgments

I wish to thank Mr Charles Constancon for his guidance, supervision and encouragement throughout the project, and Mr Richard Backeberg and Mr Geoff Krige for their efforts in getting the project off the ground and in obtaining additional financial assistance. I would also like to express my gratitude to Dr Malcom Greenway and his staff at the Mechanical Engineering Department of the Anglo American Corporation of South Africa, in particular Mr Alf van Dijk and Mr Roger Lindegger. The loan of equipment and the advice and assistance rendered by them made the experimental side of the project possible.

Contents

List of Figures

List of Tables

Nomenclature

$\{x(t)\}$	vector of displacement responses
$\{\dot{x}(t)\}$	vector of velocity responses
$\{\ddot{x}(t)\}$	vector of acceleration responses
$\{f(t)\}$	vector of excitation forces
$[M]$	mass matrix
$[K]$	stiffness matrix
$[C]$	damping matrix
$[I]$	identity matrix
$[\ ]_{diag}$	diagonal matrix
$[\ ]^T$	Transpose matrix
$[\ ]^{-1}$	inverse matrix
a_r	element of diagonal matrix $[a_r]_{diag}$
ω_r	natural frequency of vibration
$\{\psi\}_r$	rth mode shape
${}_r\psi_j$	jth element of rth mode shape
$[\psi]$	matrix of mode shapes
$\{\phi\}_r$	mass normalized mode shape r
${}_r\phi_j$	jth element of rth mode shape
$[\phi]$	matrix of mass normalized mode shapes
$[\alpha(\omega)]$	frequency response function matrix
α_{jk}	element of FRF matrix relating response at j to excitation at k
${}_rA_{jk}$	modal constant for rth mode, FRF linking coordinates j and k
ζ_r, η_r	damping coefficients
MAC_{ab}	modal assurance criteria relating modes a and b
T	system kinetic energy
P	system potential energy
S	system strain energy
$[N]$	matrix of shape functions

$[B]$	strain-displacement matrix
$[E]$	matrix of material elastic properties
$\{U_1\}$	master degrees of freedom
$\{U_2\}$	slave degrees of freedom
$[K]^*$	reduced stiffness matrix
$[M]^*$	reduced mass matrix
k_b	bunton stiffness
k_g	guide mid span stiffness
k_0	average guide stiffness
μ	half amplitude of guide stiffness variation
Ω_1	average rotational natural frequency of conveyance-guide system
Ω_2	average translational natural frequency of conveyance-guide system
$\bar{k}_b$	dimensionless bunton stiffness
$\bar{h}$	dimensionless skip displacement

Chapter 1

INTRODUCTION

1.1 STRUCTURAL ANALYSIS

Structural analysis may be broadly divided into two areas, namely static and dynamic. Static analysis involves the evaluation of forces, moments, deflections, stresses and strains that arise from time invariant loads. The techniques for such analyses are relatively straight forward and although they have been in use for decades, they are still commonly used today. Dynamic analysis, on the other hand, involves determining the same variables, but under conditions of time variant loads. The techniques required are considerably more complicated and it is only with the advent of powerful computers and computation methods that these techniques are being used for structural analysis.

Historically engineers have designed excessively heavy and stiff structures to avoid the complexity of dynamic analyses. However, in the modern highly competitive engineering world, only efficiently designed products can survive. Vibration problems can no longer be solved by simply "beefing up" components. The consumer demands structural components that are light and strong (and thus more susceptible to vibration), yet fail less frequently. It is thus vitally important for the modern engineer to have a knowledge of the dynamic properties of a structure and how they affect its performance.

Ideally the static and dynamic design considerations should be accounted for in the design phase of a structure. However the operating conditions are often not known accurately, or they may be different from the design conditions. In such cases a structure, though well designed, may not perform satisfactorily and it may be necessary to modify it to change its characteristics. It is thus obvious that a knowledge of structural dynamic characteristics is essential in both the design stage as well as in trouble shooting of existing structures.

In South Africa, extensive dynamics-related problems regarding the operation of mine conveyances in vertical shafts have been experienced. These problems and the research program undertaken to rectify them are discussed briefly in the next section.

1.2 MINE CONVEYANCES

Conveyances used in South African gold mines may be broadly divided into two groups:

- SKIPS — used to remove the gold-bearing ore from the working levels.
- CAGES — used to transport men, equipment and materials to the levels where they are needed.

These conveyances (of which there are several per shaft) generally run in steel equipped, concrete-lined, vertical, circular shafts. The shaft steelwork serves the purpose of guiding the conveyance as it travels in the shaft. Each conveyance runs in its own *compartment*. Several guide configurations are used, the most popular being two and three guide systems. Figure 1.1 shows a typical shaft installation. Figures 1.2 and 1.3 show a typical skip and cage respectively.

1.2.1 Behaviour of Conveyances and Steelwork

Although gold mines in South Africa have become progressively deeper and larger, few parallel advances in the design of shaft steelwork and conveyances have been made. Greenway [1] states that the approach to the design of steelwork was to assume that a certain fraction of the total conveyance weight acted (statically) on the steelwork. The system was thus not viewed as a dynamic one. It was realized in the 1960's that this lack of understanding of the dynamic behaviour of steelwork and conveyances could lead to unsatisfactory performance. This has been the case: extensive dynamics-related problems have been experienced by a number of mines [1,2,3]. Fortunately most of the problems have not been severe — minor fatigue cracking of components, loosening of bolts, excessive guide wear and difficulty in

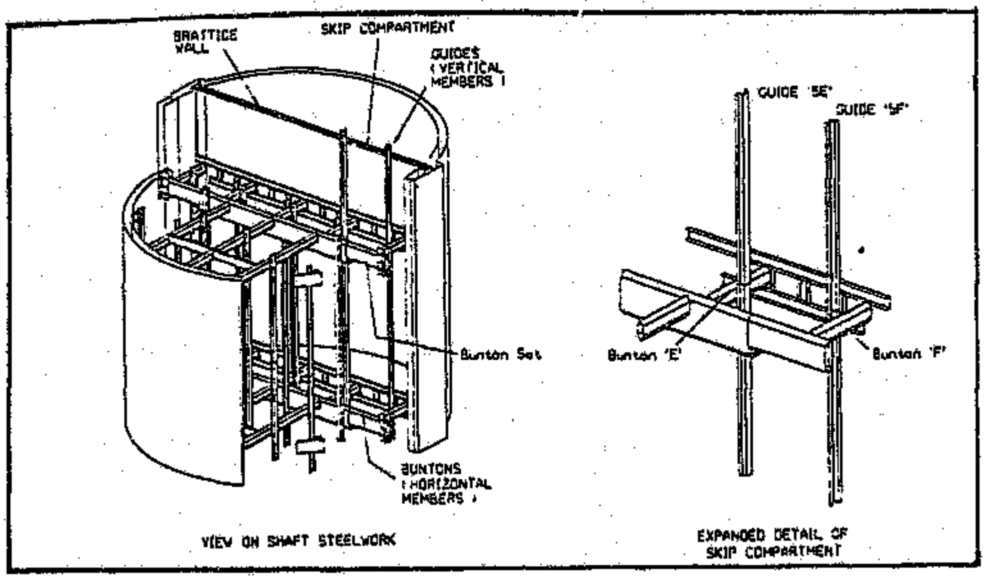

Figure 1.1: Typical modern shaft steelwork installation

maintaining accepta`` guide alignment. However one shaft has experienced bunton failur, ecessitating a costly bunton replacement and guide realignment program.

As a result of these problems an extensive research program, funded by the Chamber of Mines Research Organization (COMRO), has been pursued since 1982 [1]. The objective of this research has been to improve the understanding of the dynamic behaviour of mineshaft steelwork and conveyances and ultimately to provide design engineers with guidelines which will enable them to avoid the dynamic problems experienced in present installations.

1.2.2 COMRO Research Program

The COMRO research program set out to develop an understanding of the interaction between a skip and shaft steelwork by means of an extensive test program. Computer simulations were then used to carry out parametric studies to determine the effect of various design parameters. These parametric studies were used to develop a set of design guidelines.

The test program included the acquisition of data to fully characterize the dynamic properties of both a skip and the shaft steelwork at a shaft where problems were being experienced. It was found that the skip behaviour was mainly rigid body type and hence the dynamic properties of the skip-

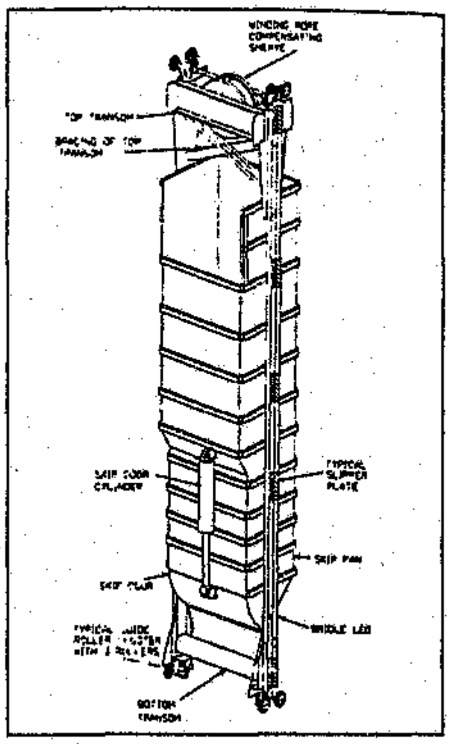

Figure 1.2: Typical SALA type skip

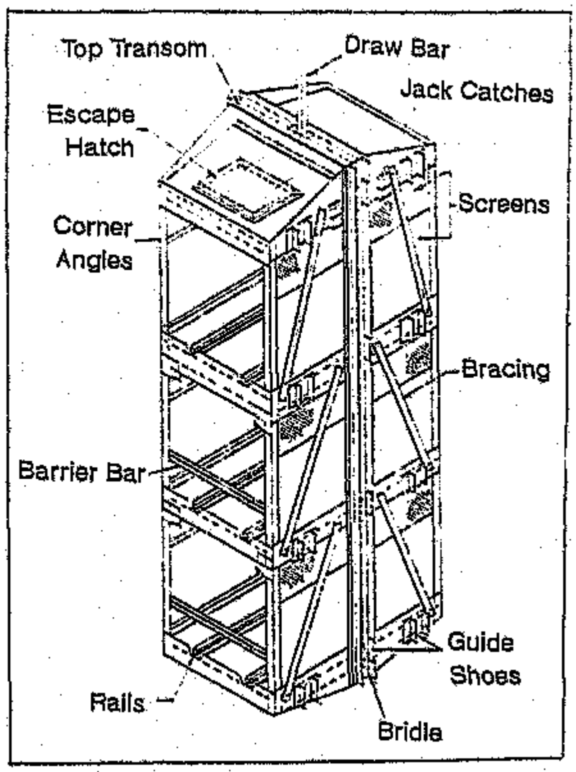

Figure 1.3: Typical three deck aluminium mine cage

steelwork system were not important to overall behaviour. However it was found that where metal to metal contact between slipper plates and guides occurred during an event known as *slamming*, both the skip and the steelwork responded in their natural flexible modes of vibration. This vibration of the steelwork and skip is the cause of fatigue cracking of components and loosening of bolts etc., mentioned above.

Slamming occurs when metal to metal contact between the skip and guides takes place at a point on the guide near a bunton. In this area the guide is very stiff in comparison to its stiffness at mid span and high impact forces result. Metal to metal contact occurs when the guide rollers do not function correctly as a result of a roller tyre failure, incorrect pre-load settings or if the guides are badly aligned. Local, rather than global, guide misalignment is of prime importance here.

Parametric studies with a computer model of the slamming phenomenon indicated that slamming forces could be reduced by increasing the stiffness of the guides and decreasing the stiffness of the buntons. In addition the behaviour of a rigid SALA type skip was compared to that of a more flexible JETO type skip and it was found that the forces in a slamming event were very much lower in the case of the JETO skip.

In all of these studies only skips were investigated. Although it is known that skips are generally stiffer than cages, no work has been carried out to quantify the dynamic characteristics of cages. The techniques of structural analysis may be used to this end.

In this study, the techniques of Experimental Modal Analysis (EMA) and the Finite Element Method (FEM) are used in the analysis of a mine cage. The natural frequencies and mode shapes of the cage are detrmined by conducting a modal test using the impact excitation technique. A large hammer and transducer are designed and built for this purpose. Finite element models of the cage are developed and tuned to accurately reproduce results of the modal test. The use of the experimental and analytical methods is termed the *dual* approach in this thesis. The term "dual" has no mathematical connotations.

1.3 OBJECTIVES

The objectives of this project are presented in point form below. It was realized at the beginning of the project that some of these objectives would be difficult to achieve. The project does not set out to fully investigate the dynamic behaviour of mine cages and shaft steelwork. It sets out to improve the present understanding of mine cages and in so doing provide the author with a vehicle to improve his own knowledge in the fields of experimental and analytical dynamic analysis.

1. To apply experimental modal testing techniques in the evaluation of the dynamic characteristics of mine cages.
2. To evaluate the use and application of the Finite Element Method for determining the dynamic characteristics of mine cages.
3. To use the dual FEM-EMA approach to develop a FEM model of a mine cage.
4. To improve the understanding of the dynamic behaviour of mine cages.

1.4 DISSERTATION STRUCTURE

The remainder of the dissertation is set out as follows:
The experimental procedure and some important points on signal processing as well as the theory relevant to the techniques of dynamic analysis are discussed in Chapter 2. This includes methods for curve fitting to EMA data and some numerical techniques used in solving eigen problems in the FEM. Important characteristics of conveyance and shaft steelwork systems are discussed in Chapter 3. A simple structure in the form of a flat steel plate is analyzed using EMA and FEM in Chapter 4. This analysis was conducted to gain experience in the use of EMA and FEM. A mine cage is analyzed using the dual FEM-EMA approach in Chapter 5. A discussion of the project is presented in Chapter 6 and conclusions and recommendations are presented in Chapters 7 and 8 respectively. A brief description of the equipment used in the study and other information and results which would otherwise detract from the continuity of the dissertation are presented in the Appendices.

Chapter 2

DYNAMIC ANALYSIS

Experimental Modal Analysis (EMA) or modal testing is described by Ewins [6] as

> *the processes involved in testing components or structures with the objective of obtaining a mathematical description of their dynamic or vibration behaviour.*

Mitchell [24] claims that EMA "grew to prominence because the engineering community was incapable of properly analyzing the dynamics of commercially significant structures". However, techniques such as the Finite Element Method (FEM), with significant dynamic capabilities, have been developed. Rieger [21] describes Finite Element Analysis (FEA) as a "computerized procedure for the analysis of structures and other continua'. Despite advances in analytical modelling, EMA continues to thrive. In fact, Ewins goes on to say that perhaps the most common application of modal testing is the measurement of data for comparison and validation of finite element or other theoretical models. Stevens [23] states that recent developments in the merging of experimental and analytical techniques have made it possible to construct accurate analytical models of complex systems, which in turn is having a major impact on design procedures. Rieger [21], shows by means of case studies that experimental modal analysis and finite element analysis can be co-ordinated into an effective diagnostic procedure for vibration analysis.

From the above it is apparent that there are two techniques available for the dynamic modelling of structures. One is an experimental technique and the other is an analytical technique. The two techniques can be used independently of one another, but used together they form a powerful design and diagnostic tool.

The dynamic characteristics of a structure can be defined by means of its mass, stiffness and damping properties — the time domain or spatial model. Although real structures are continuous systems and their mass, stiffness and damping are thus distributed, they can often be represented as an assemblage of rigid masses connected by spring and damper elements. The equations of motion for such a *lumped parameter system* are easily obtained by applying Newton's Second Law of Motion :

$$\sum F = ma \tag{2.1}$$

to each mass. The resulting equations of motion are :

$$[M]\{\ddot{x}\} + [C]\{\dot{x}\} + [K]\{x\} = \{F\} \tag{2.2}$$

A similar set of equations are obtained by means of the Finite Element Method. In this method, the structure is divided into small *finite elements,* interconnected by *nodes.* A simple distribution of displacement is assumed within each element and the unknown nodal displacements are solved for, using numerical methods. The method is an approximate one, but skillful selection of the element type and mesh results in a realistic and accurate model.

An alternative to the time domain model is the modal model, the dynamic characteristics being defined by means of the natural frequencies, mode shapes and modal damping. Here the system's responses are a function of frequency, rather than time. The two models are equivalent and in principle it is possible to derive one from the other by mathematically transforming from the time domain to the frequency domain or vice versa.

Analytical modal analysis is the process whereby the modal model is extracted from the time domain model. This may be achieved by finding the eigenvalues and eigenvectors of equation 2.2, the external forces $\{F\}$ being set to zero (the *free vibration* condition). The eigenvalues determine the natural frequencies and damping for each mode, while the eigenvectors represent the corresponding characteristic deflected shape or mode shape of the structure.

Experimental modal analysis is the process of extracting the modal model from experimental data. The structure is subjected to an excitation $f(t)$ and the responses $x(t)$ are measured. The responses are determined by the structure's properties $h(t)$. Using the Laplace Transform, it is possible to transform to the frequency domain. This is represented schematically in Figure 2.1.

The relation between steady state input and output is represented by

$$F(s)H(s) = X(s) \tag{2.3}$$

or

$$H(s) = \frac{X(s)}{F(s)} \tag{2.4}$$

where $H(s)$ is called the *trans, , inction*, expressing the dynamic characteristics of the structure in terms of the complex variable $s = a + jw$. A special case of this transform occurs when $a = 0$ and is called the Fourier Transform. This is easily calculated using the Fast Fourier Transform (FFT) algorithm with a digital computer. The transfer function then becomes

$$H(jw) = \frac{X(jw)}{F(jw)} \tag{2.5}$$

and is called the *Frequency Response Function* (FRF). FRF's are calculated from measurements of system response by means of multichannel spectrum analyzers. In practice the excitation (usually a force) is applied to a small number of points on the structure and the response (usually an acceleration) is measured at a large number of points. A large number of FRF's are thus required to describe a structure. By curve fitting analytical expressions to the measured FRF's, the natural frequencies, damping and modes shapes of the structure are obtained.

The analysis is based on the fact that for a linear system, the response to any excitation may be expressed as a linear combination of the natural modes of vibration of the system. The most important assumption is that the structure is assumed to be linear.

2.1 BASIC THEORY

Consider the simple system consisting of a mass m, a spring of stiffness k, and a damper of viscous damping coefficient c, depicted in Figure 2.2. If the system is set in motion by one or another means, the displacement or response of the mass is time dependent and is given by $x(t)$. If an excitation in the form of a force $f(t)$ is applied to the system, the response is termed *forced vibration*. If the system is set in motion and no further excitation force is applied, the response is termed *free vibration*. Free vibrations describe the natural behaviour or the natural modes of vibration of the system. In a system with damping, the free vibrations will diminish with time as the damper dissipates the energy initially input to the system. If there is no damping present, the vibrations will not diminish with time as the energy is not dissipated — the system is said to be conservative. The number of degrees of freedom of a vibratory system is the number of *independent spatial coordinates* necessary to define its geometric configuration [10]. A rigid body in space requires six degrees of freedom to describe its configuration — three translational and three rotational degrees of freedom. The system shown in Figure 2.2 requires only one degree of freedom to describe its configuration, hence it is termed a single degree of freedom (SDOF) system. A system requiring n degrees of freedom to describe its configuration would be capable of vibrating in n different natural modes of vibration, each characterized by a natural frequency, corresponding mode shape and description of the rate of energy dissipation — the modal damping.

The spatial model consists of the mass, stiffness and damping properties of the system. A frequency response analysis of the spatial model leads to a description of the structure's properties as a function of frequency. A free vibration analysis produces a description of the manner in which the system behaves naturally by means of the natural frequencies, mode shapes and modal damping - the modal model. In a forced response analysis, a sinusoidal excitation is applied to the system and the steady state response is examined. The response and excitation are sinusoidal and of the same frequency for a linear system. The *frequency response characteristics* of the structure are described by means of *frequency response functions*, defined as the ratio of response to excitation — the response model. Hence there three models describing a system. Analysis of the *spatial model* leads to development of the *modal model* and the *response model*.

2.1.1 SDOF Systems

Applying Newton's Second Law of Motion to the above single degree of freedom system results in the following equation of motion describing the system:

$$m\ddot{x} + c\dot{x} + kx = f$$

Undamped systems

Consider this system with no excitation force or damping, that is the undamped free vibration situation. The solution to the resulting equation is obtained by substituting a trial solution [6,7] of the form $x(t) = xe^{i\omega t}$, resulting in the requirement that $k - \omega^2 m = 0$. This produces a single natural frequency

$$\omega_0 = \sqrt{\frac{k}{m}} \tag{2.6}$$

Now considering the response of the system to an excitation of the form $f(t) = fe^{i\omega t}$, we once again assume a solution of the form $x(t) = xe^{i\omega t}$. Substituting into the equation of motion and re-arranging to obtain an expression for the ratio of the response to excitation results in a *frequency response function:*

$$\frac{x}{f} = \alpha(\omega) = \frac{1}{k - \omega^2 m}$$

Damped systems

Viscous damping

If we include the presence of a viscous damper, the free vibration situation requires a more general trial solution, of the form $x(t) = xe^{st}$, resulting in the condition $ms^2 + cs + k = 0$. This equation has two roots:

$$s_{1,2} = \frac{-c \pm \sqrt{c^2 - 4km}}{2m}$$

Defining $\omega_0 = \sqrt{\frac{k}{m}}$ and $\zeta = \frac{c}{2\sqrt{km}}$, the solution becomes:

$$s_{1,2} = -\omega_0\zeta \pm i\omega_0\sqrt{1 - \zeta^2}$$

Since there are two roots, the response will take the form

$$x(t) = X_1 e^{s_1 t} + X_2 e^{s_2 t}$$

where $X_{1,2}$ are constants determined by the initial conditions. Defining $\omega_0' = \omega_0\sqrt{1 - \zeta^2}$ and substituting and simplifying gives the following expression for the response:

$$x(t) = e^{-\omega_0\zeta t}[(X_1 + X_2)\cos\omega_0' t + i(X_1 - X_2)\sin\omega_0' t]$$

Since the response is a real physical quantity, $(X_1 + X_2)$ and $i(X_1 - X_2)$ must each be real too. In order for this to be the case, X_1 and X_2 must be complex conjugates, hence the response becomes

$$x(t) = e^{\omega_0' t}(B_1 \cos\omega_0' t + A_2 \sin\omega_0' t)$$

Clearly, the response has two components: an imaginary, oscillatory part with a frequency of ω_0' — the damped natural frequency, and a real, decay part resulting from the damping. For the forced response analysis, the same form of excitation and response as for the undamped system are used. This results in a frequency response function:

$$\alpha(\omega) = \frac{1}{k - m\omega^2 + i\omega c}$$

In contrast to the undamped FRF, this is a complex quantity, containing magnitude and phase information.

Hysteretic damping
It is found that for real structures, having many degrees of freedom, the viscous damping model is not adequate. A damper whose rate varies inversely with frequency is required [6,15,13] — the structural or hysteretic damper. The equation of motion for the forced response of the structurally damped system becomes:

$$(\omega^2 m + k + ih)xe^{i\omega t} = fe^{i\omega t}$$

and the frequency response function becomes:

$$\alpha(\omega) = \frac{1}{k - \omega^2 m + ih}$$

Analysis of the free vibration case presents some difficulty and is not dealt with here.

2.1.2 MDOF Systems

Real systems are generally multi degree of freedom (MDOF) systems and the equations of motion are conveniently written in matrix form, as follows:

$$[M]\{\ddot{x}(t)\} + [C]\{\dot{x}(t)\} + [K]\{x(t)\} = \{f(t)\}$$

For an N degree of freedom system, $[M]$, $[K]$, $[C]$ are NxN matrices and $\{x(t)\}$, its time derivatives and $\{f(t)\}$ are Nx1 vectors. There is an equation of motion for each degree of freedom. The stiffness matrix $[K]$ is symmetric due to the Maxwell-Betti reciprocity relationship for elastic structures [7]. The mass matrix $[M]$ is also symmetric due to the Beltrami-Mitchell compatibility requirements.

Undamped system

Consider again the undamped free vibration condition for the multi degree of freedom system. Assume a solution of the form $\{x(t)\} = xe^{i\omega t}$ [6,7]. This implies that the entire system can vibrate at a single frequency ω. Substituting into the matrix equation of motion leads to the requirement that:

$$|[K] - \omega^2[M]| = 0$$

which gives N possible values of ω^2, the undamped natural frequencies ω_r of the system. Substituting these values of ω^2 into the equations of motion leads to a corresponding set of values for the vector {x}. These are the mode shapes $\{\psi\}_r$ corresponding to the natural frequencies ω_r. The modal model may thus be presented in the form of two NxN *eigen* matrices: a diagonal matrix of the natural frequencies (eigenvalues) ω_r^2 and a matrix whose columns are the modes shape vectors (eigenvectors) $\{\psi\}_r$, represented as $[\psi]$. The eigenvalue matrix is unique, but the eigenvectors are not. Each eigenvector represents the relativ^ displacements of the degrees of freedom. The scaling of the vector is determined by the procedures followed to obtain the solution and does not affect its shape. The modal model has certain orthogonality properties such that:

$$[\psi]^T[M][\psi] = [m_r]_{diag} \tag{2.7}$$

and

$$[\psi]^T[K][\psi] = [k_r]_{diag} \tag{2.8}$$

The values m_r and k_r are called the modal mass and stiffness of mode r. Because $[\psi]$ is not unique, neither are m_r and k_r, however the ratio $\frac{k_r}{m_r}$ is unique and $\frac{k_r}{m_r} = \omega_r^2$. One important means of scaling the eigenvectors is known as mass-normalizing [6] and the mass normalized eigenvectors are denoted:

$$\{\phi\}_r = \frac{\{\psi\}_r}{\sqrt{m_r}} \tag{2.9}$$

hence

$$[\phi]^T[M][\phi] = [I]_{diag} \tag{2.10}$$

and

$$[\phi]^T[K][\phi] = [\omega_r^2]_{diag}$$

The usefulness of this transformation will become apparent later.

For the forced response analysis we assume a solution of the same form as for the free vibration case, but the structure is now excited by a set of sinusoidal forces, all of the same frequency, ie: $\{f(t)\} = \{f\}e^{i\omega t}$. Substituting into the matrix equation of motion and rearranging:

$$\{x\} = \frac{\{f\}}{[K] - \omega^2[M]} = [\alpha(\omega)]\{f\}$$

$[\alpha(\omega)]$ is now an NxN matrix of frequency response functions. An element of this matrix is defined as:

$$\alpha_{jk} = \frac{x_j}{f_k}$$

with the condition that $f_m = 0$ for $m = 1, N; \neq k$. Essentially this means that α_{jk} is the FRF resulting from a response at j induced by an excitation at k, all other excitations being zero. Again the Maxwell-Betti reciprocal relation applies [7] and $\alpha_{jk} = \alpha_{kj}$, hence $[\alpha(\omega)]$ is a symmetric matrix. Using the orthogonality relationships, it is possible to derive a more useful expression for elements of the FRF matrix:

$$([K] - \omega^2[M]) = [\alpha(\omega)]^{-1}$$

Premultiplying by $[\phi]^T$ and post multiplying by $[\phi]$ we get:

$$[\phi]^T[K][\phi] - \omega^2[\phi]^T[M][\phi] = [\phi]^T[\alpha(\omega)]^{-1}[\phi]$$

or

$$[\omega_r^2]_{diag} - [\omega^2]_{diag} = [\phi]^T[\alpha(\omega)]^{-1}[\phi]$$

therefore

$$[\alpha(\omega)] = [\phi][\omega_r^2 - \omega^2]_{diag}^{-1}[\phi]^T$$

The fact that $[\alpha(\omega)]$ is a symmetric matrix is confirmed by the form of this equation. An element of the matrix is given by :

$$\alpha_{jk}(\omega) = \sum_{r=1}^{N} \frac{{}_r\phi_j \, {}_r\phi_k}{\omega_r^2 - \omega^2}$$

or

$$\alpha_{jk}(\omega) = \sum_{r=1}^{N} \frac{{}_rA_{jk}}{\omega_r^2 - \omega^2}$$

where ${}_rA_{jk} = {}_r\phi_j \, {}_r\phi_k$ is defined as the modal constant for mode r, for the FRF linking coordinates j and k.

Systems with proportional damping

Proportional damping occurs when the damping matrix is also orthogonal to the eigenvectors of the undamped system [6,7]:

$$[\psi]^T[C][\psi] = [c_r]_{diag}$$

The system can be represented by a set of decoupled second order differential equations.

Viscous damping

We now consider the special case where the viscous damping matrix is assumed to be proportional to a linear combination of the mass and stiffness matrices:

$$[C] = \alpha[M] + \beta[K]$$

and by pre- and post multiplying by the undamped system $[\psi]$:

$$[\psi]^T[C][\psi] = \alpha[\psi]^T[M][\psi] + \beta[\psi]^T[K][\psi]$$

or

$$[\psi]^T[C][\psi] = \alpha[k_r]_{diag} + \beta[m_r]_{diag} = [c_r]_{diag}$$

The significance of this is that the mode shapes of the damped and undamped system are identical, while the resonant frequencies differ slightly:

$$\omega_r' = \omega_r\sqrt{1-\zeta_r^2}$$

where $\zeta_r = \frac{\beta\omega_r}{2} + \frac{\alpha}{2\omega_r}$. The forced response analysis leads to the following equation for an element of the FRF matrix:

$$\alpha_{jk}(\omega) = \sum_{r=1}^{N} \frac{{}_rA_{jk}}{\omega_r^2 - \omega^2 + i\omega\frac{c_r}{m_r}}$$

Hysteretic damping
A similar result can be obtained for the proportionally hysteretically damped system. In this case, the equation of motion is:

$$[M]\{\ddot{x}(t)\} + [K + iH]\{x(t)\} = \{f(t)\}$$

and

$$[H] = \alpha[K] + \beta[M]$$

The FRF is given by:

$$\alpha_{jk}(\omega) = \sum_{r=1}^{N} \frac{{}_rA_{jk}}{\omega_r^2 - \omega^2 + i\eta_r\omega_r^2}$$

The mode shapes are again the same as for the undamped system, and the eigenvalues (denoted by λ_r) are complex:

$$\lambda_r = \omega_r \sqrt{1 + i\eta_r}$$

where

$$\eta_r = \alpha + \frac{\beta}{\omega_r^2}$$

For the undamped and proportionally damped systems, the mode shapes are all identical. The natural frequencies of the proportionally damped systems are complex, with an oscillatory part and a decay part which arises from the dissipation of energy by the damping elements.

Systems with general damping

Hysteretic damping

The general hysteretically damped system is discussed first because it is simpler than its viscous counterpart.

The equation of motion of the free vibration system is:

$$[M]\{\ddot{x}(t)\} + [K]\{x(t)\} + i[H]\{x(t)\} = 0$$

Assuming a solution of the form $\{x(t)\} = \{x\}e^{i\lambda t}$ leads to the requirement that:

$$|[K] + i[H] - \lambda^2[M]| = 0$$

As with the undamped system, the solution is in the form of the two matrices containing the eigenvectors and eigenvalues respectively. However, in this case, both of these matrices are complex. We can write the rth eigenvalue as:

$$\lambda_r = \omega_r'' \sqrt{1 + i\eta_r}$$

where ω_r'' is the natural frequency and η_r is the structural damping loss factor. This is similar to the eigenvalues for the proportionally damped system, but the resonant frequency ω_r'' is not necessarily the same as for the undamped case, ω_r. The most important difference results from the eigenvectors being complex. The displacement of each coordinate has a phase angle as well as a magnitude. This means that when the system is vibrating at a natural frequency, all coordinates of the mode shape do not reach their maximum displacement at the same time, as they do for the undamped and proportionally damped systems. For the latter systems, the displacements could be considered complex, but with a zero complex part: the phase is thus either 0 or 180 degrees. The orthogonality properties of the system are as follows:

$$[\psi]^T[M][\psi] = [m_r]_{diag}$$

and

$$[\psi]^T[K + iH][\psi] = [k_r]_{diag}$$

and

$$\lambda_r^2 = \frac{k_r}{m_r}$$

The mass normalized eigenvectors are again given by:

$$\{\phi\}_r = \frac{\{\psi\}_r}{\sqrt{m_r}}$$

The forced response analysis leads to the following expression for an element of the FRF matrix:

$$\alpha_{jk}(\omega) = \sum_{r=1}^{N} \frac{{}_rA_{jk}}{\omega_r^2 - \omega^2 + i\eta_r\omega_r^2}$$

Because the mode shapes are complex, the numerator of this expression is also complex.

Viscous damping

The equation of motion for the general viscous damped system is:

$$[M]\{\ddot{x}(t)\} + [C]\{\dot{x}(t)\} + [K]\{x(t)\} = \{f(t)\}$$

If we define a vector {y(t)} made up of displacements and velocities, such that:

$$\left\{ y(t) \right\} = \left\{ \begin{array}{c} \dot{x}(t) \\ x(t) \end{array} \right\}$$

then the equation of motion can then be re-written as:

$$\left[[M] \quad [C] \right] \left\{ \dot{y}(t) \right\} + \left[[0] \quad [K] \right] \left\{ y(t) \right\} = \left\{ f(t) \right\}$$

resulting in a set of N equations, but with $2N$ unknowns. By introducing the identity equation:

$$[M]\{\dot{x}(t)\} - [M]\{\dot{x}(t)\} = 0$$

written in the form

$$\left[[0] \quad [M] \right] \left\{ \dot{y}(t) \right\} + \left[-[M] \quad [0] \right] \left\{ y(t) \right\} = \left\{ 0 \right\}$$

we can obtain an equation of the form:

$$\left[\begin{array}{cc} [0] & [M] \\ [M] & [C] \end{array} \right] \left\{ \dot{y}(t) \right\} + \left[\begin{array}{cc} -[M] & [0] \\ [0] & [K] \end{array} \right] \left\{ y(t) \right\} = \left\{ \begin{array}{c} \{0\} \\ \{f(t)\} \end{array} \right\}$$

or

$$[A]\{\dot{y}(t)\} + [B]\{y(t)\} = \{z(t)\} \tag{2.11}$$

which is $2N$ equations in $2N$ unknowns. This is now in the form of the well known and simple to solve eigenvalue problem. It can be seen that for the free vibration situation, where we assume a solution of the form $\{y(t)\} = \{y\}e^{st}$ and set $\{z(t)\} = 0$, equation 2.11 only has a solution when

$$|s[A] + [B]| = 0$$

The rth eigenpair consisting of $2N$ eigenvalues, s_r, and $2N$ eigenvectors $\{\theta\}_r$ satisfy the equation:

$$(s_r[A] + [B])\{\theta\}_r = 0 \tag{2.12}$$

$\{\theta\}_r$ now consists of a displacement vector and a velocity vector. By manipulating equation 2.12 we can again arrive at the orthogonality properties, this time stated in terms of the matrices $[A]$ and $[B]$:

$$\{\theta\}_r^T[A]\{\theta\}_q = 0$$

and

$$\{\theta\}_r^T[B]\{\theta\}_q = 0$$

for the cases where $r \neq q$, which implies that

$$[\theta]^T[A][\theta] = [a_r]_{diag}$$

and

$$[\theta]^T[B][\theta] = [b_r]_{diag}$$

It can be shown ([6,7]) that

$$2\omega_r\zeta_r = \frac{c_r}{m_r}$$

and

$$\omega_r^2 = \frac{k_r}{m_r}$$

where m_r, k_r and c_r are the modal mass, stiffness and damping terms.

For the forced response analysis, we assume a trial solution of the form $\{y(t)\} = \{y\}e^{i\omega t}$ and an excitation of the form $z(t) = \{z\}e^{i\omega t}$ and substituting into equation 2.11 and dividing by $e^{i\omega t}$, we get:

$$i\omega[A]\{y\} + [B]\{y\} = \{z\} \tag{2.13}$$

Because the $2N$ eigenvectors are linearly independent of one another it is possible, using the principle of superposition, to write:

$$\{y\} = \sum_{r=1}^{2N} \gamma_r\{\theta\}_r \tag{2.14}$$

where γ_r are a set of coefficients determining the participation of each eigenvector in the response $\{y\}$. Substituting equation 2.14 into equation 2.13 and multiplying by $\{\theta\}_q^T$ we get:

$$i\omega\{\theta\}_q^T\,[A]\sum_{r=1}^{2N}\gamma_r\{\theta\}_r+\{\theta\}_q^T\,[B]\sum_{r=1}^{2N}\{\theta\}_r=\{\theta\}_q^T\{z\}$$

Simplifying using the orthogonality properties we get:

$$i\omega a_q\gamma_q+b_q\gamma_q=\{\theta\}_q^T\{z\}$$

and solving for γ_q we get:

$$\gamma_q=\frac{\{\theta\}_q^T\{z\}}{(i\omega a_q+b_q)}$$

where a_q, b_q are the qth elements on the diagonals of $[a_r]_{diag}$ and $[b_r]_{diag}$ respectively. Back substituting into equation 2.14 we get:

$$\{y\}=\sum_{r=1}^{2N}\frac{\{\theta\}_r^T\,\{z\}\,\{\theta\}_r}{i\omega a_r+b_r}$$

By further manipulation of equation 2.12 we can show that

$$s_r=\frac{-b_r}{a_r}$$

hence

$$\{y\}=\sum_{r=1}^{2N}\frac{\{\theta\}_r^T\,\{z\}\,\{\theta\}_r}{a_r(i\omega-s_r)} \tag{2.15}$$

Now the complex eigenvalues obtained by the free vibration analysis s_r may be written as:

$$s_r=\omega_r(-\zeta_r\pm i\sqrt{1-\zeta_r^2})$$

Substituting for s_r in equation 2.15 and returning to the original coordinate system (recalling that $\{\dot{x}\}=i\omega\{x\}$) we get:

$$\left\{\begin{array}{c}i\omega\{x\}\\\{x\}\end{array}\right\}=\sum_{r=1}^{2N}\frac{\{\theta\}_r^T\left\{\begin{array}{c}\{0\}\\\{f\}\end{array}\right\}\{\theta\}_r}{a_r(i\omega+\zeta_r\omega_r\pm i\omega\sqrt{1-\zeta_r^2})}$$

If we now isolate a specific case for the excitation applied at location k and the response measured at location j, we get that

$$\frac{x_j}{f_k} = \alpha_{jk}(\omega) = \sum_{r=1}^{2N} \frac{{}_r\theta_k \, {}_r\theta_j}{a_r(i\omega + \zeta_r\omega_r \pm i\omega_r\sqrt{1-\zeta_r^2})}$$

or defining

$${}_rA'_{jk} = \frac{{}_r\theta_j \, {}_r\theta_k}{a_r}$$

we get:

$$\alpha_{jk}(\omega) = \sum_{r=1}^{2N} \frac{{}_rA'_{jk}}{i\omega + \zeta_r\omega_r \pm i\omega_r\sqrt{1-\zeta_r^2}} \tag{2.16}$$

In the above discussion, the concept of a frequency response function $\alpha(\omega)$ was introduced. It was defined as the ratio of the response to the excitation and in all the cases dealt with, the response was a displacement $x(t)$, and the excitation a force $f(t)$. Practically, it may not be convenient to measure the displacement response of the system. Hence we may define other forms of the FRF using the velocity response $v(t)$ or the acceleration response $a(t)$ as follows: $Y(\omega) = \frac{v}{f}$ and $A(\omega) = \frac{a}{f}$. The terms $\alpha(\omega)$, $Y(\omega)$ and $A(\omega)$ are known as the system *receptance*, *mobility* and *inertance* respectively. It can be seen that if we let $x(t) = xe^{i\omega t}$, then $Y(\omega) = i\omega\alpha(\omega)$ and that $A(\omega) = -\omega^2\alpha(\omega)$.

At this stage it is important to point out that by applying an excitation at one point on a structure and measuring the responses at all points of interest, we are able to determine a single row (or column) of the FRF matrix. If we excite the structure at more than one point, we are able to measure more rows of the FRF matrix.

2.2 MODAL TEST PROCEDURE

In this section, some of the more important considerations in carrying out an experimental modal analysis are discussed. Points relevant to the impact test procedure are dealt with. More detailed information regarding the impact and other test procedures is available in [6,7]. The technical specifications of the equipment used in the modal tests may be found in Appendix A.

Experimental modal analysis requires that a structure's response to an excitation, as well as the excitation itself, be measured in order to determine the structure's properties. The test system comprises the following:

- Structure
- Transduction system
- Excitation system
- Analyzer

2.2.1 Structure Set Up

In selecting the type of support for the structure, the conditions under which the test piece will normally operate must be taken into consideration. The structure to be tested must be set up in such a way that the data to be measured will suit the objective of the test. It must be decided what boundary conditions suit this purpose — there are essentially only two choices: either the structure will be *grounded* or it will be *free*. In the grounded condition, some points of the structure will be restrained or fixed to ground. In the free condition, no point of the structure is restrained. In reality, neither of these conditions can be perfectly created, though approximation to the free condition is easier to achieve than the grounded condition. In analyzing a cantilevered beam, testing the beam in the free condition would serve little purpose, as the operating conditions require that one end of the beam be restrained in several degrees of freedom. Clearly, more meaningful results will be obtained by testing the beam with one end properly restrained.

Because the structure must be held in some way, it is not possible to achieve a truly free condition. However, it is possible to mount the structure in such a way as to minimize the interference of the mountings on the motion in certain degrees of freedom of interest. For example, a plate could be suspended along its edge by means of rigid wires. These wires, being perpendicular to the primary vibrations of the plate, would have an insignificant effect on such vibrations. Alternatively, the structure could be mounted on very flexible supports. For example, the plate could be laid on a piece of soft sponge. In this case, the mounting would interfere with the degrees of freedom of interest, however provided that the sponge is soft enough, the effect will not be great enough to have any influence on the flexural modes. Ewins [6], indicates that the highest rigid body mode frequency of the structure and its mountings should be less than 20 % of that of the lowest flexural mode. Should it not be possible to avoid interference with degrees of freedom of interest, then the mountings should be placed as near to nodes of the first flexural mode as possible. Obviously for very large structures, providing mountings to simulate the free condition becomes more difficult and such structures must then be tested in the grounded condition. It may seem that to fix or ground a given point on a structure is a simple matter when compared to attempting to simulate a free condition. However, any support structure designed to ground the test piece is not perfectly rigid and it is found in practice that providing a rigid base is not a simple task. Care must be taken to ensure that the support does not influence the stiffness of the structure and that the flexibility of the support at all of the ground points is much higher than that of the structure at such points.

Having decided on the boundary conditions for the test, the measurement grid must be established. The basic criteria in selecting response measurement points is that they should be capable of defining adequately the geometry of the structure when in resonance at the highest mode of interest. When the dual EMA and FEM approach is used, responses must be measured at points matching those on the FEM grid, to allow comparison of the FEM and experimental mode shapes. Where possible, responses should not be measured at points which are known to be nodes as the low responses will make accurate measurements difficult to obtain. If results of a preliminary FEM analysis are available, they can be useful in avoiding such problems. A preliminary FEM analysis can also indicate whether there are any local effects present which should be investigated in the modal test.

If the structure is correctly set up and the measurement grid thoughtfully designed, numerous tests will not be necessary. This is particularly important when investigating a practical problem where the test object cannot easily be taken out of production for test purposes.

2.2.2 Transduction System

The transduction system comprises accelerometers for measuring responses, force transducers for measuring the excitation and the signal conditioning amplifiers needed to boost the transducer signals to levels suitable for input to the analyzer. A FM tape recorder is also useful to store the signals for later processing, should it not be practical to use the analyzer at the site of the test. Transducers are generally of the piezoelectric type.

The means of fixing the accelerometers to the structure is of paramount importance. Wax, magnets and studs are some of the possible methods.

Each method has a frequency limit, beyond which it should not be used. Studs provide reliability over the greatest frequency range. It is not always possible to attach studs directly to a structure, however, a technique used successfully by the author entailed gluing small steel discs to the structure. The discs had been drilled and tapped using a lathe and one surface ground to a smooth finish. This ensured that the axis of the stud would be perpendicular to the disc and there would be good contact between the accelerometer and disc. On small structures, the method of attachment and the mass of the accelerometer can affect the stiffness and mass characteristics of the structure, resulting in erroneous results. For larger structures these effects are less significant.

When testing a large structure, very long cables are required. Care must be taken to ensure that the number of joints is kept to a minimum and that connections are good. It is good practice to check all cables in the laboratory prior to attempting a test on site. Cables should be prevented from hanging loosely and moving in wind as this can produce spurious signals. The gain of the amplifiers should be checked and adjusted for each point on the measurement grid to ensure that signals of suitable strength are available for the analyzer.

2.2.3 Excitation

Exciters can be broadly divided into contacting and non-contacting classes. Impact excitation falls into the non-contacting class of excitation as the exciter (hammer) is only in contact with the structure for a very short period of time. Exciters in the contacting class remain in contact with the structure throughout the test. Special precautions must be taken to ensure that such exciters do not interfere with the motion of the structure. Consequently they require a greater set up time. Impact excitation has the advantage of being a very quick method, but more accurate results can be obtained using contacting type excitation techniques. As a result, impact testing is often used for a "first look" to identify areas of interest which are then investigated thoroughly using a contacting type technique. Further discussion will be limited to impact excitation.

The impact hammer comprises a massive body, the mass of which can be varied by means of extender masses, a force transducer and a set of tips of varying stiffness. The magnitude of the impact force is controlled by means of the mass of the hammer and its velocity. The frequency range over which the hammer imparts energy to the structure is controlled via the stiffness of the tip and the mass of the hammer. The hammer-tip system has a resonant frequency determined by the mass of the hammer and the stiffness of the tip. Above this frequency very little energy will be imparted to the structure. The force pulse delivered by a hammer blow is similar in shape to a half sine wave, which has a frequency content that is flat, but which drops off sharply after the hammer-tip resonant frequency. To ensure that the maximum energy is imparted to the test structure within the frequency range of interest, the mass and stiffness of the tip should be selected to coincide the hammer-tip resonant frequency with the maximum frequency of interest.

Hammer blows should be applied at the same point on the structure and at the same orientation. A number of impacts should be averaged to obtain data at a particular point on the measurement grid (averaging reduces random errors). Double impacts should be avoided and the magnitude of the blows should also be kept reasonably constant in order to make use of the full dynamic range of the analyzer. The above considerations are easier to fulfill if the hammer is suspended by some mechanism, rather than hand held. The structure's responses must have decayed to zero, ie. it must have stopped ringing, before the next hammer blow is delivered. All attachments — extender masses and tips — must be firmly mounted to eliminate spurious signals caused by vibration of loose components. When selecting the point of impact of the hammer, care should be taken that the impacts do not load the structure beyond its linear (elastic) range. The excitation point should also be chosen in such a way that all foreseeable modes are excited.

2.2.4 Analyzer Set Up

Setting up the analyzer (GR 2515) to capture data was a task simplified by means of the DATM data acquisition software available. There are essentially three potential signal processing problems, associated with the calculation of the discreet fourier transform, which the user must be aware of. They are aliasing, leakage and noise.

Aliasing

Aliasing results from the digitizing of the original analogue time histories. It affects mainly the response signals. If the digitizing sampling rate is too slow, then some high frequency data will be indistinguishable from certain low frequency data, causing distortion of the spectrum calculated from the discreet fourier transform. To correct this problem, anti-aliasing filters are used. These are low-pass, sharp cut-off filters. Because the cut-off occurs over a finite frequency, the spectrum in the cut-off area will not be alias-free.

For example, if the analyzer is set up with a baseband frequency of 64 Hz, then only the spectrum up to say 50 Hz will be alias-free. Thus the analysis can be confidently conducted in the range 0–50 Hz, and not 0–64 Hz.

Leakage and Noise

Leakage results from the combined effects of the need to measure signals of only finite length and the assumption (required by the discrete Fourier transform) that the signal is periodic in time. It affects mainly the response signals. If the signal is periodic in the finite time sample, then there is no discontinuity between the value at the beginning and end of the sample. However, if it is not, then there is a discontinuity and this causes energy to be "leaked" into the spectrum in frequencies near to those of the true spectrum frequencies. Noise is a problem that affects both the excitation and response signals, but which is particularly important for the excitation (force) signal. Leakage and noise can be reduced using windows especially designed for that purpose [26].

An exponential window is applied to the response signal in order to force the signal to zero at its ends, eliminating the discontinuity and hence the leakage. Such a window is necessary when the responses do not decay naturally to zero within the required sampling interval. This usually arises when a lightly damped structure is analyzed with a large frequency baseband because the structure rings for a long time after the impact and the high frequency baseband demands a short time interval. The window may be applied several times, if necessary, and it introduces artificial damping, which may be evaluated and subtracted from damping estimates to determine the real damping present.

A force window is used to improve the signal-to-noise ratio on the force signal. The force signal comprises a half sine wave pulse, the duration of which is small in comparison with the length of the time span. Consequently, the energy contained in the noise can be significant compared to that contained in the force pulse. The force window artificially eliminates any signal existing immediately before and after the force pulse. The force pulse resembles a half sine wave, but when such a pulse is viewed on the analyzer, some ringing is apparent. This is merely a consequence of the anti-aliasing filters, and not ringing of the hammer-tip arrangement.

2.2.5 Coherence

The coherence function gives the tester some indication of how well the measurements of transfer function have been made. A very brief description of coherence will be presented here. Further detail may be obtained from texts such as [6,12]. In essence, analyzers are able to estimate various quantities involved in calculating an estimate of the transfer function. These quantities are estimates because because only finite data samples are used. There are at least two "formulae" for arriving at an estimate of the transfer function. These two formulae will not necessarily produce exactly the same result, hence by comparison of the two results, we have an indication of how well the measurements have been made. Coherence is defined as the ratio of the transfer functions derived from the two formulae. Ideally, the coherence should be equal to unity, but this will not be the case as the two estimates of the transfer function will rarely be identical. In fact, the coherence is always less than or equal to unity [6].

Sources of less than unity coherence include the following:

1. Noise on either the response or excitation signal. Near resonance, the excitation signal is more vulnerable because the measured force is very small, resulting in poor a signal-to-noise ratio. Conversely, near anti-resonances, the response signal is more susceptible to low signal-to-noise ratios.

2. Where the frequency resolution of the analyzer is not small enough to describe adequately the rapid variations encountered near a resonance.

3. Where the structure is not linear and the response is not entirely attributed to the effect of the excitation.

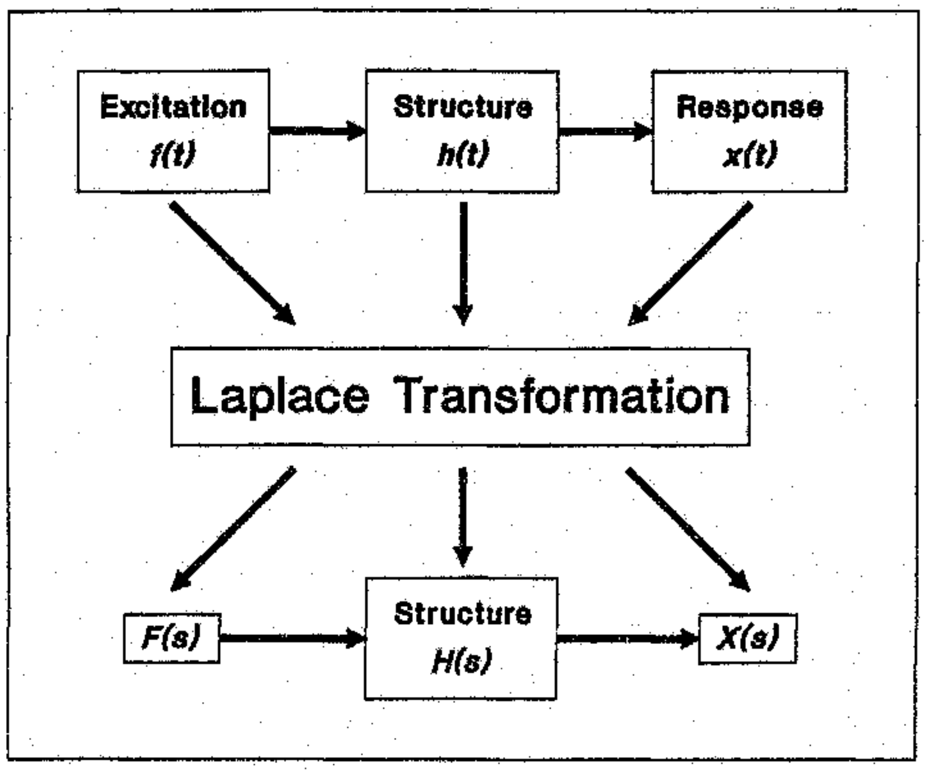

Figure 2.1: Time and frequency domain representations of a structure

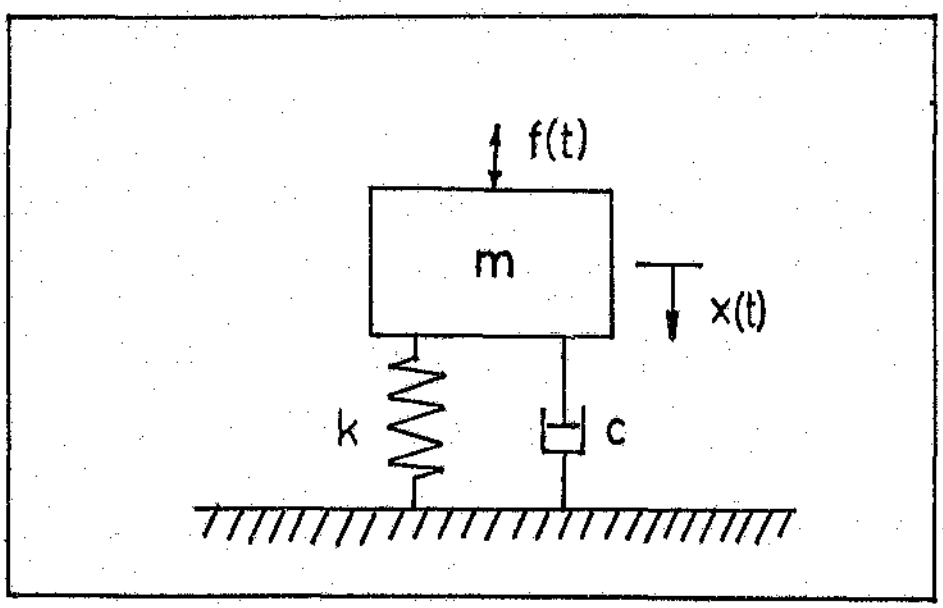

Figure 2.2: Simple mass, spring and viscous damper system

2.3 MODAL PARAMETER EXTRACTION

The display of the FRF data forms a very important part of the analysis procedure and there are many methods which may be used. Because the FRF is generally a complex quantity it has magnitude and phase, each varying with frequency. The most common type of plot is the Bode plot, consisting of plots of magnitude and phase versus frequency, all quantities being plotted on log scales because of the large range of data encountered. Another type of plot is the Nyquist plot, consisting of the locus traced by plotting the imaginary part against the real part as the frequency varies. On the Bode plot, resonances appear as peaks, separated by troughs or by "negative" peaks, known as anti-resonances. Under certain conditions, the Nyquist plot traces a circle in the region around a resonance. A more detailed discussion of the form of these plots may be found in [6].

Once the FRF's have been measured, the next step in the analysis is the extraction of modal parameters from the FRF data. This is done by curve fitting a theoretical expression to the FRF data either in the time domain or in the frequency domain. There are numerous curve fitting techniques available, each having its own peculiarities, strengths and weaknesses. Modern modal analysis systems offer the user the choice of several methods. In order for the user to decide which method is best suited to his situation and to obtain the best performance from the chosen method, a knowledge of how these techniques operate is essential. Single degree of freedom (SDOF) curve fitting procedures make the assumption that around a resonance, the system response is dominated by that resonance. Such methods fit a curve to a single resonance or mode on an FRF. However, for systems of high modal density, the modes may be so close together or so heavily damped that the response at resonance is not dominated by one mode. In such cases it is necessary to fit a curve to the entire FRF, including all resonances of interest. These methods are called multi degree of freedom (MDOF) curve fitting procedures. SDOF techniques should be used if possible as they are faster and simpler than MDOF techniques, though with the availability of increasingly sophisticated computers, computing time is becoming less of a deciding factor in the choice of the type of curve fitting technique. As a practical guide to deciding when MDOF methods should be used, Smiley et al [18] suggest that when the peaks on FRF's are more than 3 dB above the surrounding data, SDOF techniques are sufficiently accurate.

2.3.1 Interpretation Functions

Two functions that are commonly used in the interpretation of experimentally measured transfer functions are the *mode indicator function* (MIF) and the *conjugate summation function* (CSF) [8]. These functions are useful for identifying the number and approximate position of resonances since they operate on the whole database. They are usually used to provide some visual indication of the number and position of modes before the curve fitting process is started.

The MIF is defined as:

$$MIF = \frac{\sum |Re(\alpha_{jk})|\ |\alpha_{jk}|}{\sum |\alpha_{jk}|^2}$$

The MIF has a maximum value of unity and local minimums occur where modes of the structure occur. Even modes with low amplitudes will be apparent.

The CSF is defined simply as:

$$CSF = \sum \alpha_{jk}\alpha_{jk}^*$$

The CSF has local peaks where modes of the structure occur. Modes with low amplitude may not be apparent because of the large dynamic range of the data.

2.3.2 SDOF Curve Fitting Techniques

The methods described here are frequency domain methods.

Circle-fit method

Using the hysteretically damped system as an example, the receptance FRF is given by:

$$\alpha_{jk} = \sum_{s=1}^{N} \frac{{}_sA_{jk}}{\omega_s^2(1 - (\frac{\omega}{\omega_s})^2 + i\eta_s)}$$

which can be shown to be the equation of a circle in the real-imaginary plane [6]. Splitting this equation into two terms describing the specific mode in question and all the other modes, we can write:

$$\alpha_{jk} = \frac{{}_rA_{jk}}{\omega_r^2(1-(\frac{\omega}{\omega_r})^2+i\eta_r)} + \sum_{s=1,\neq r}^{N} \frac{{}_sA_{jk}}{\omega_s^2(1-(\frac{\omega}{\omega_s})^2+i\eta_s)} \tag{2.17}$$

For a small range of frequency around the frequency of mode r, the second term is assumed independent of frequency. This means that the circle traced out by the first term alone is the same as that traced out by the sum of the two terms, but is displaced from the origin by the amount of the second term. It is thus possible to examine a particular modal circle for the purpose of extracting the modal parameters. For a particular mode and a particular FRF we drop the subscripts and look at the first term only:

$$\alpha = \frac{A}{\omega_r^2(1-(\frac{\omega}{\omega_r})^2+i\eta_r)}$$

To simplify, we can set $A = 1$ since the effect of the modal constant A is to scale the diameter by $|A|$ and rotate it by $B = \arctan\frac{Re(A)}{Im(A))}$. It can be shown that the rate at which the the circle is traced out as the frequency ω increases from 0 through to infinity, reaches a maximum when $\omega = \omega_r$. The damping of the mode may be evaluated by considering two points a and b on the circle shown in Figure 2.3.

$$\tan\left(\frac{\theta_b}{2}\right) = \frac{1-\left(\frac{\omega_b}{\omega_r}\right)^2}{\eta_r}$$

and similarly

$$\tan\left(\frac{\theta_a}{2}\right) = \frac{\left(\frac{\omega_a}{\omega_r}\right)^2-1}{\eta_r}$$

By adding these two equations and solving for η_r we get

$$\eta_r = \frac{\omega_a^2-\omega_b^2}{\omega_r^2\left(\tan\left(\frac{\theta_a}{2}\right)+\tan\left(\frac{\theta_b}{2}\right)\right)} \tag{2.18}$$

and if the damping is light this may be simplified to:

$$\eta_r = \frac{2(\omega_a - \omega_b)}{\omega_r \left(\tan\left(\frac{\theta_a}{2}\right) + \tan\left(\frac{\theta_b}{2}\right)\right)}$$

For the case where $\theta_a = \theta_b = 90$ degrees (the half power points), this simplifies further to:

$$\eta_r = \frac{\omega_a - \omega_b}{\omega_r} \tag{2.19}$$

At resonance, $\omega = \omega_r$ and the diameter of the circle is given by:

$$D = \frac{|A|}{\omega_r^2 \eta_r} \tag{2.20}$$

The same steps may be applied to the system with viscous damping, but using the system mobility rather than receptance as it is the former that produces a circle in the real-imaginary plane for this case.

The above circle fit procedure thus entails the following:

- Fit a circle to the points in the region where a resonance is suspected.
- Establish the natural frequency by finding the maximum sweep rate.
- Use equation 2.18 to determine the damping.
- Evaluate the modal constant A using the diameter of the circle to find $|A|$ (equation 2.20) and the circle centre position to evaluate the phase angle.

This procedure can be done for every FRF obtained and at every resonance identified, hence damping estimates and mode shapes for each resonance are calculated.

Peak pick method

This method is simpler, but less accurate than the above method. It is not a curve fitting procedure as such. A peak on an FRF plot (Figure 2.4) is chosen and the frequency of maximum response (R_{max}) is taken as the natural frequency ω_r. The half power points are then identified — the points at which the response level is equal to $\frac{R_{max}}{\sqrt{2}}$. Equation 2.19 can then be used to estimate the damping. The modal constant A may then be estimated by assuming that the total response at resonance is attributed to only the resonance in question:

$$A = R_{max}\, \omega_r^2 \eta_r$$

This assumption ignores the effects of the other modes all together, unlike in the above procedure where the effect is considered. In addition, only real modal constants may be estimated because the value of R_{max} used is a real number, being the magnitude of the FRF at a specific frequency.

2.3.3 MDOF Curve Fitting Techniques

Extension of SDOF method

In the SDOF circle fit method, we assumed that the second term in equation 2.17 was constant for a small range of frequency around the resonance of interest. If we first carry out a SDOF analysis we will have an estimate of the required coefficients that make up the second term and thus we no longer need assume that the second term remain constant. We can calculate the value of that term, subtract it from a measured value for the term on the left hand side of equation 2.17 and then perform a curve fit for the first term, obtaining a new, better estimate for the parameters for mode r. This procedure can then be repeated iteratively until suitable convergence has been achieved.

Complex exponential method

This method is a time domain curve fitting procedure [6,8]. A single FRF is used to extract the modal parameters. It makes use of the time domain version of the FRF — the Impulse Response Function (IRF), which is obtained by inverse Fourier transforming the FRF. The IRF represents the decaying time history response of the system subjected to a unit impulse [12]. Considering the system with viscous damping, we have an expression for $\alpha_{jk}(\omega)$ in equation 2.16. By inverse Fourier transforming this expression we can arrive at an expression for the IRF, $h_{jk}(t)$:

$$h_{jk}(t) = \sum_{r=1}^{2N} {}_rA_{jk}\, e^{s_r t}$$

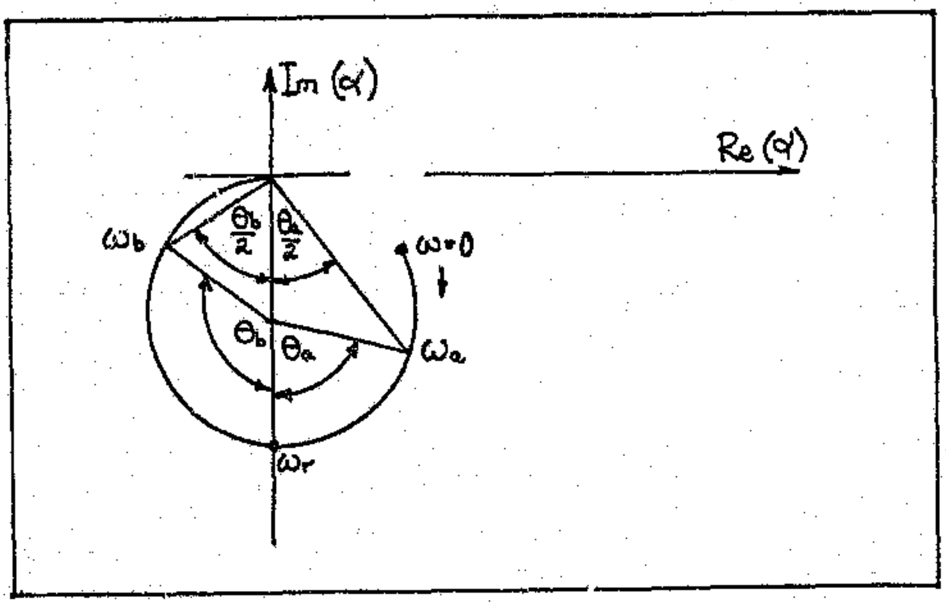

Figure 2.3: Modal circle

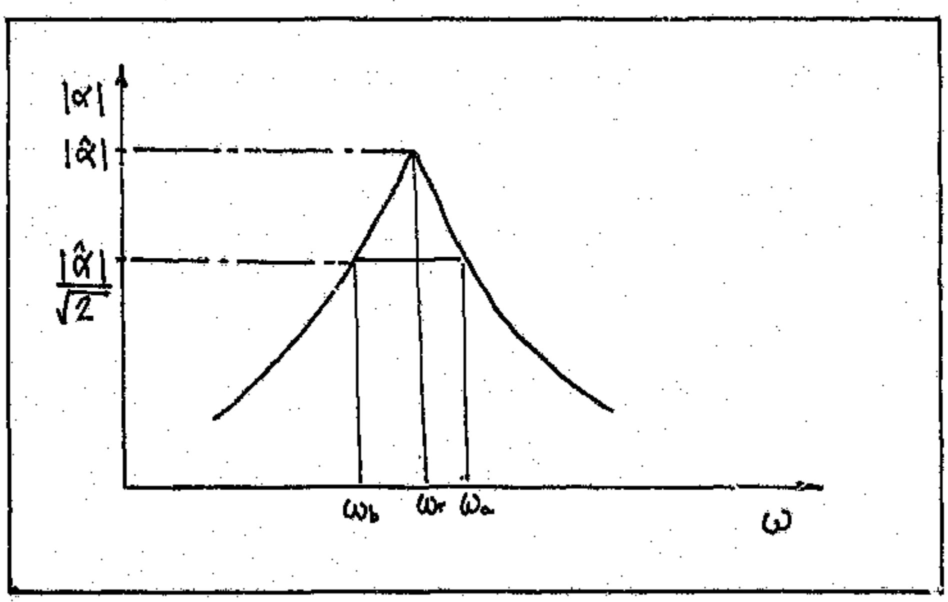

Figure 2.4: Peak on FRF plot

If the time interval over which the IRF is defined is divided into $2N$ equal intervals of length T, then the value of the IRF for the Kth interval is given by (dropping subscripts):

$$h(t_K) = \sum_{r=1}^{2N} {}_rA\,{}_rV^K$$

where ${}_rV = e^{s_r T}$. Expanding this equation at each time interval gives the following set of equations:

$$\begin{aligned}
h(t_0) &= {}_1A + \quad {}_2A + \quad \cdots + {}_{2N}A \\
h(t_1) &= {}_1A\,{}_1V + \quad {}_2A\,{}_2V + \quad \cdots + {}_{2N}A\,{}_{2N}V \\
h(t_2) &= {}_1A\,{}_1V^2 + \quad {}_2A\,{}_2V^2 + \quad \cdots + {}_{2N}A\,{}_{2N}V^2 \\
&\vdots \\
h(t_{2n}) &= {}_1A\,{}_1V^{2n} + \quad {}_2A\,{}_2V^{2n} + \quad \cdots + {}_{2N}A\,{}_{2N}V^{2n}
\end{aligned} \tag{2.21}$$

There is a polynomial of order $2n$ that will satisfy the expression:

$$V^{2n} + \rho_1\, V^{2n-1} + \rho_2\, V^{2n-2} + \cdots + \rho_{2n-1}\, V + \rho_{2n} = 0 \tag{2.22}$$

and which has roots ${}_1V$, ${}_2V$, $\cdots {}_{2n}V$, in which case the polynomial may be re-written as:

$$(V - {}_1V)(V - {}_2V)\cdots(V - {}_{2n}V) = 0$$

In order to determine the coefficients ρ in the polynomial, multiply row 1 of equation 2.21 by ρ_{2n}, row 2 by ρ_{2n-1} etc., noting that from equation 2.22, $\rho_0 = 1$:

$$\begin{aligned}
\rho_{2n}h(t_0) &= \rho_{2n}({}_1A + \quad {}_2A + \quad \cdots + {}_{2N}A) \\
\rho_{2n-1}h(t_1) &= \rho_{2n-1}({}_1A\,{}_1V + \quad {}_2A\,{}_2V + \quad \cdots + {}_{2N}A\,{}_{2N}V) \\
\rho_{2n-2}h(t_2) &= \rho_{2n-2}({}_1A\,{}_1V^2 + \quad {}_2A\,{}_2V^2 + \quad \cdots + {}_{2N}A\,{}_{2N}V^2) \\
&\vdots \\
h(t_{2n}) &= {}_1A\,{}_1V^{2n} + \quad {}_2A\,{}_2V^{2n} + \quad \cdots + {}_{2N}A\,{}_{2N}V^{2n}
\end{aligned}$$

Summing:

$$\sum_{K=0}^{2n} \rho_{2n-K}\, h(t_K) = \sum_{K=0}^{2n} \rho_{2n-K} \left(\sum_{r=1}^{n} {}_rA\,{}_rV^K \right) = \sum_{r=1}^{n} {}_rA \left(\sum_{K=0}^{2n} \rho_{2n-K}\, {}_rV^K \right)$$

Clearly, since ${}_rV$ is a root of equation 2.22,

$$\sum_{K=0}^{2n} \rho_{2n-K}\ {}_rV^K = 0$$

Therefore

$$\sum_{K=0}^{2n} \rho_{2n-K}\ h(t_K) = 0 \tag{2.23}$$

This entire procedure is then repeated, but this time starting with row 2 of equation 2.21. An extra row is added to equation 2.21 for $h(t_{2n+1})$ so that there are always a set of $2n+1$ equations. This results in the equation

$$\sum_{K=0}^{2n} \rho_{2n-K}\ h(t_{K+1}) = 0$$

An entire set of such equations can be developed and written in the form of a matrix equation:

$$\begin{bmatrix} h(t_{2n-1}) & h(t_{2n-2}) & \cdots h(t_0) \\ h(t_{2n}) & h(t_{2n-1}) & \cdots h(t_1) \\ \vdots & & \vdots \\ h(t_{4n-2}) & h(t_{4n-3}) & \cdots h(t_{2n-1}) \end{bmatrix} \begin{bmatrix} \rho_1 \\ \rho_2 \\ \vdots \\ \rho_{2n} \end{bmatrix} = - \begin{bmatrix} h(t_{2n}) \\ h(t_{2n+1}) \\ \vdots \\ h(t_{4n-1}) \end{bmatrix} \tag{2.24}$$

Equation 2.24 is solved for the unknown coefficients ρ which are then substituted into equation 2.22 and the roots ${}_rV$ are solved for. Since ${}_rV = e^{s_r T}$, and $s_r = \omega_r(-\zeta_r + i\sqrt{1-\zeta_r^2})$, it can be shown that

$$|{}_rV| = e^{-\zeta_r \omega_r T}$$

and

$$\angle\, {}_rV = \omega_r \sqrt{1-\zeta-r^2}\, T$$

from which values of ω_r and ζ_r may be obtained. All that remains to solve for is the modal constant ${}_rA$ by substituting for the roots in ${}_rV$ in equation 2.21.

In order to use the method, an estimate of the of the number of degrees of freedom ($2n$) is required. To do this, the method calculates an estimate of the FRF using a number of different values of $2n$ and compares the difference or error between them. This is presented in the form of an error plot which gives the error versus the number of degrees of freedom. When the correct number degrees of freedom is reached, the error levels off, indicating that the use of a larger number of degrees of freedom will not improve the accuracy. This optimum number of degrees of freedom will result in the determination of the true structural modes as well as some computational modes which attempt to account for effects of modes outside the frame of analysis as well as discrepancies resulting from the measurement process (noise, leakage errors, effects of using time windows).

Polyreference technique

This technique is also a time domain technique operating on the IRF. However it is a global curve fitting technique which operates on multiple FRF's for multiple reference locations. A complete discussion of the technique may be found in references [16,17,8]. The FRF database may be built up using FRF's obtained from several separate single exciter tests or from a single multiple exciter test. The method requires as input FRF's as defined in the above sections — that is the FRF between two points, one of which is the point of excitation, all other excitations being zero. In other words a test procedure whereby the structure is excited by simultaneous multiple inputs, and the FRF calculated simply as the ratio of response to one of the inputs, will not be correctly analyzed by the polyreference method.

The analysis procedure involves summing the FRF's from various reference locations into a correlation matrix. This matrix is used to extract the natural frequencies, damping coefficients and mode shapes of the system. The selection of response locations that are incorporated in the matrix has a significant effect on the final results. By choosing responses from a certain part of the structure, local modes will be emphasized. On the other hand, by using all responses, the overall structural modes will be dominant. In the case where only one reference location is used, the polyreference technique produces the same result as the complex exponential technique and the latter is considered a special case of the former. The advantage of the polyreference method is that it produces a global estimate of the required parameters as opposed to a set obtained by examining a single FRF (as in the complex exponential method). This is especially significant when we consider that a single exciter test may not excite all of the modes of a system. By including data from a test with exciters in different locations a more complete and accurate description of the system is possible.

Many other modal parameter estimation techniques exist and new ones are constantly being developed, particularly methods that provide global estimates of modal parameters. Ibrahim [19] concludes that generally, time domain curve fitting methods are more accurate, better able to handle systems with high modal density and require less operator judgment and interaction than frequency domain methods.

It is important to realize that the quality of results obtained are only as good as the quality of the measured data. The use of sophisticated curve fitting algorithms on poor data cannot account for inadequacies in the measured data.

2.3.4 Residuals

In the above discussion of curve fitting techniques, methods for determining modal parameters were discussed. When these parameters are used to generate a theoretical FRF it is often found that the resulting curve does not appear to fit the measured data very well. This is a result of the effects of modes outside the frequency range of the analysis. When the theoretical FRF is generated, the equation used will typically be of the type:

$$\alpha_{jk}(\omega) = \sum_{r=m1}^{m2} \frac{{}_rA_{jk}}{\omega_r - \omega^2 + i\eta_r\omega_r^2}$$

The limits $m1$ and $m2$ represent the limits over which the curve fit took place. The equation which would represent the actual data would include the effect of terms below $m1$ and terms above $m2$:

$$\alpha_{jk}(\omega) = \sum_{r=1}^{N} \frac{{}_rA_{jk}}{\omega_r - \omega^2 + i\eta_r\omega_r^2}$$

which may be re-stated as:

$$\alpha_{jk}(\omega) = \sum_{r=1}^{m1-1} + \sum_{r=m1}^{m2} + \sum_{r=m2+1}^{N} \left(\frac{{}_rA_{jk}}{\omega_r - \omega^2 + i\eta_r\omega_r^2} \right)$$

A structure's low frequency response is dominated by its mass characteristics, while its high frequency response is dominated by its stiffness characteristics. In the above equation, the first term, representing the low frequency behaviour of the structure is called the *residual mass* and the third term, representing the high frequency behaviour is called the *residual stiffness* of the FRF. The residual terms are evaluated by comparing the measured value of the FRF to the theoretically generated value at the respective ends of the analysis. The difference between the two values at the low frequency end is used to evaluate a residual term of the form $\frac{1}{\omega^2 {}_rM_{jk}}$. At the upper end of the frequency range the residual of the form $\frac{1}{{}_rK_{jk}}$ is evaluated. The addition of these residual terms do not affect the estimates of the original parameters, but merely allows the theoretical curve to fit more closely to the measured curve by taking into account effects outside the frequency range of the analysis.

2.3.5 Quality of Modal Database

Once a set of natural frequencies, mode shapes and damping factors have been determined, the question arises as to how good these estimates are. If we consider the results in isolation from results obtained by any other method of analysis, there are essentially two checks which can be used to evaluate the quality of the database. Firstly, the database should be able to synthesize FRF's that correspond well with the measured data. This check amounts to visually comparing measured and synthesized curves. The second check is based on the fact that each mode shape should be linearly independent of the others. The Modal Assurance Criteria (MAC) provides a measure of the least squares deviation from the straight line correlation of two mode shapes. For two mode shapes, a and b, the MAC is defined as [6]:

$$MAC_{ab} = \frac{|\sum_{j=1}^{n}(\phi_a)_j(\phi_b)_j^*|^2}{\sum_{j=1}^{n}(\phi_a)_j(\phi_a)_j^* \sum_{j=1}^{n}(\phi_b)_j(\phi_b)_j^*}$$

The * represents the complex conjugate, hence complex mode shapes can be compared. When the two mode shapes are identical or if they differ only by a scaling factor, $MAC_{ab} = 1$, indicating 100 % correlation and that the mode shapes are fully linearly dependent. If the two mode shapes are linearly independent, then $MAC_{ab} = 0$, indicating 0 % correlation. The values of MAC_{ab} are usually presented in matrix form. If a set of mode shapes from an EMA are compared to one another, the values of MAC will be in the form of a symmetrical square matrix with unity on the diagonal. The off-diagonal terms should be very low — of the order of 0.05 if the modes are linearly independent. If the off diagonal terms are high, one of the following may be the cause: non-linearities in the test structure, split modes (the same mode identified at two different but very close frequencies), noise on the measured data or poor analysis of the data.

While the MAC was originally used to check the linear independence of mode shapes obtained from EMA, it can be used to compare mode shapes from two different analyses, for example an EMA and FEM analysis. When a set of mode shapes are compared to themselves the matrix is known as the Auto-MAC, while if shapes from different analyses are compared, the matrix is called the Cross-MAC. The Auto-MAC is always a square, symmetric matrix with unity on the diagonal [6,7]. The Cross-MAC need not exhibit any of these characteristics.

2.4 THE FINITE ELEMENT METHOD (FEM)

The finite element method is a numerical procedure for obtaining an approximate solution to partial differential equations. Such equations occur in fields such as stress analysis, fluid flow, heat transfer etc.. A structure or flow field is divided into a number of small or finite *elements*. Elements are assumed to be connected to one another at a discrete number of positions or *nodes* along their boundaries. The variable of interest is defined by simple functions which are chosen to uniquely define the state of the field within the element in terms of the value of the variable at the nodes. This enables the solution to be found for each element and subsequently for the entire problem. As the size of the elements used decreases and simultaneously the number of elements increase, we can expect the solution to converge towards the true solution.

One formulation of the method is that applied to stress analysis, known as the displacement based method. It can be viewed as an extension of the displacement method of analysis used in the analysis of beam and truss structures. In this case, the variation of the displacement $\{s\}$ through the element is defined in terms of the displacements at the nodes $\{u\}$. Generally, each node requires 3 translations and 3 rotations to fully define its displacement in space. The functions chosen to approximate the variation of displacement are called *shape functions* or *interpolation functions*, $[N]$. The displacement at a point within an element is given by $\{s\} = [N]\{u\}$ and the velocity is given by $\{\dot{s}\} = [N]\{\dot{u}\}$. To a large extent the choice of the functions $[N]$ determines the degree of accuracy that can be achieved by the method. The shape functions usually take the form of polynomials. More advanced developments include the time dimension in the formulation of the shape functions. This can be useful for dynamic analyses but obviously the addition of another dimension increases the complexity of the problem. Usually the standard displacement type formulation is used in conjunction with standard integration algorithms to determine the response properties as a function of time.

The Lagrange method expresses the energies of the system in terms of the *generalized* coordinates $\{U\}$ and obtains the equations of motion of the system directly. The Lagrange equations [10] for a conservative system are:

$$\frac{d}{dt}\left(\frac{\partial T}{\partial \dot{U}}\right)+\left(\frac{\partial P}{\partial U}\right)=0 \tag{2.25}$$

where T is the system kinetic energy and P is the system potential energy.

The kinetic energy of an element of density ρ can be expressed as

$$T_{el}=\int_{vol}\frac{1}{2}\rho\{\dot{s}\}^T\{\dot{s}\}dV=\frac{1}{2}\{\dot{u}\}^T\int_{vol}\rho[N]^T[N]dV\{\dot{u}\} \tag{2.26}$$

The integral $\int_{vol}\rho[N]^T[N]dV=[m]$ is called the mass matrix of the element.

The work done by internal stresses resulting from deformation of the structure is stored as internal strain energy, S. The strains $\{\epsilon\}$ experienced by an element are related to the nodal displacements by the *strain-displacement matrix* $[B]$:

$$\{\epsilon\}=[B]\{u\}$$

Generally, $\{\epsilon\}$ has 3 direct strains and 3 shear strains. For an element with material whose elastic properties may be described by the matrix $[E]$, the internal strain energy is

$$S_{el}=\int_{vol}\frac{1}{2}\{\epsilon\}^T[E]\{\epsilon\}dV=\frac{1}{2}\{u\}^T\int_{vol}[B]^T[E][B]dV\{u\} \tag{2.27}$$

The integral $\int_{vol}[B]^T[E][B]dV=[k]$ is called the stiffness matrix of the element.

The total kinetic energy, T and the total internal strain energy of the structure, S are found simply by summing equation 2.26 and 2.27 over all elements:

$$T=\sum T_{el}=\sum\frac{1}{2}\{\dot{u}\}^T[m]\{\dot{u}\}=\frac{1}{2}\{\dot{U}\}^T[M]\{\dot{U}\} \tag{2.28}$$

and

$$S = \sum S_{el} = \sum \frac{1}{2}\{u\}^T[k]\{u\} = \frac{1}{2}\{U\}^T[K]\{U\} \qquad (2.29)$$

where $[M]$, $[K]$, $\{\dot{U}\}$ and $\{U\}$ are the structure mass matrix, structure stiffness matrix and structure nodal velocity and deflection vectors respectively. The structure stiffness matrix $[K]$ is made up by summing the contributions made by element stiffness matrices $[k]$ into the structure stiffness matrix. Each $[k]$ is associated with an area within $[K]$. Since many elements will share common nodes, there will be some overlapping of $[k]$ terms in $[K]$. These overlapping terms are simply added and account for the fact that many elements can contribute to the stiffness at a particular node. The mass matrix $[M]$ is known as the *consistent* mass matrix [15] since the same shape functions are used to generate it as are used to generate the stiffness matrix. Thus the formulation of the mass matrix is mathematically consistent with the process of minimizing the total system energy. An alternative means of generating the mass matrix is to merely lump point masses at the nodes. This results in a diagonal matrix called the *lumped* mass matrix. It is difficult to decide which formulation is the best. The consistent formulation is more difficult to generate and is generally computationally inefficient. If the lumped mass approximation is crude then many elements are required to obtain sufficient accuracy.

If there are no external forces acting on the structure, then the total potential energy of the structure is equal to the internal strain energy ie. $P = S$. Substituting equations 2.28 and 2.29 into equation 2.25 we get

$$[M]\{\ddot{U}\} + [K]\{U\} = 0$$

While the mass and stiffness matrices of the structure can be determined in a straight forward manner, the same is not true of the damping matrix. We can develop a term describing the dissipation of energy within the element, by assuming that the dissipative forces are proportional to the nodal velocities. The problem arises in determining the element damping matrix $[c]$. For a Newtonian fluid, $[c]$ can be evaluated. However, in structural mechanics hysteretic rather than viscous damping is encountered and the magnitude of the damping force is proportional to the stress rather than velocity. We can attempt to model damping by constructing the damping matrix as a linear combination of the mass and stiffness matrices. This represents a continuous damping model applied to the entire structure. In reality bolted and welded joints introduce damping effects that are not accounted for in a continuous damping FEM model. Any damping matrix that we may construct from element damping matrices will thus not be a true reflection of the actual structure damping properties. In fact it is accepted [13,14,15] that it is impractical to determine meaningful damping factors for finite element systems by assembling the element damping matrices. This is not to say that the Finite Element Method cannot analyze situations that include damping, but rather some other means of determining the damping matrix is needed. Experimental techniques such as experimental modal analysis should be used to this end.

Having established a method for evaluating the mass and stiffness matrices of a structure, we now turn to methods of solving particular problems. Since the element and structure properties are evaluated numerically, solution strategies will also be numerical. Due to the difficulties in defining the damping matrix, the following discussion will be restricted to methods of determining the solution to the undamped system. Since we are initially interested in obtaining the natural frequencies and mode shapes of the structure, we will consider the free vibration case, the equation of motion being:

$$[M]\{\ddot{x}\} + [K]\{x\} = \{0\} \tag{2.30}$$

and we recall that this reduces to the eigenvalue problem

$$([K] - \omega^2[M])\{\psi\} = 0 \tag{2.31}$$

The system maintains the orthogonality properties as stated in equations 2.7–2.10. This equation represents the basic mathematical description of a structure, thus considerable research has been devoted to its efficient solution.

2.4.1 Numerical Solution of the Eigenvalue Problem

All numerical solution procedures for the eigen problem must be iterative in nature. This is because solving the eigen problem is basically equivalent to finding the roots of the polynomial

$$|[K] - \omega^2[M]| = 0$$

which has the same order as that of $[K]$ and $[M]$. There are no explicit means of solving any polynomial of order greater than four, so iterative procedures must be used.

Many methods for solving eigen problems exist. Of particular interest are the vector iteration methods and one of these, the inverse vector iteration method will be discussed next. Inverse vector iteration is particularly suited to computer applications because it requires less reading and writing storage operations than many other methods [13].

Inverse vector iteration

Equation 2.31 can be represented as

$$[K]\{\psi\}_r = \omega_r^2[M]\{\psi\}_r \tag{2.32}$$

Multiplying by the inverse of $[K]$, setting $[K]^{-1}[M] = [G]$ and dividing by $\lambda_r = \omega_r^2$ puts this equation into the standard form

$$\frac{1}{\lambda_r}\{\psi\}_r = [G]\{\psi\}_r \tag{2.33}$$

The left hand side of equation 2.33 is a vector multiplied by a scalar while the right hand side is a vector multiplied by a matrix. The former operation merely scales the vector, leaving its direction unchanged. The latter operation scales the vector and rotates it. Equation 2.33 is only satisfied by a unique vector — the eigenvector — that is not rotated by multiplication by the matrix, but merely scaled. When the amount of scaling introduced by the matrix is equal to the scaling by the scalar on the left hand side, that scalar represents the eigenvalue. To solve equation 2.33 iteratively we substitute a trial vector for the vector on the right hand side and obtain a new, scaled and rotated vector. This direction of this vector is compared to that of the original vector and if it is not the same the process is repeated using the new vector as the next guess. The procedure eventually converges on the lowest mode of the system and when it does so, the eigenvalue is merely the ratio of the last two computed vectors. The method takes its name from the fact that the a matrix must be inverted and vectors are solved for iteratively.

The procedure may be explained mathematically as follows: We assume any arbitrary vector $\{v\}_0$ as a first guess. Since the eigenvectors of the system are known to be independent of one another, this vector can be written as a linear combination of the eigenvectors:

$$\{v\}_0 = \sum_{r=1}^{n} c_r\{\psi\}_r \tag{2.34}$$

Letting

$$\{v\}_n = [G]\{v\}_{n-1} \tag{2.35}$$

it can be seen that

$$\{v\}_1 = [G]\{v_0\} = \sum_{r=1}^{n} c_r [G]\{\psi\}_r = \sum_{r=1}^{n} c_r \frac{1}{\lambda_r}\{\psi\}_r$$

and

$$\{v\}_2 = [G]\sum_{r=1}^{n} c_r \frac{1}{\lambda_r}\{\psi\}_r = \sum_{r=1}^{n} c_r \left(\frac{1}{\lambda_r}\right)^2 \{\psi\}_r$$

By analogy it can be seen that

$$\{v\}_n = \sum_{r=1}^{n} c_r \left(\frac{1}{\lambda_r}\right)^n \{\psi\}_r \tag{2.36}$$

Separating the first term from the remaining terms in equation 2.36

$$\{v\}_n = \left(\frac{1}{\lambda_1}\right)^n c_1\{\psi\}_1 + \left(\frac{1}{\lambda_1}\right)^n \sum_{r=2}^{n} c_r \left(\frac{\lambda_1}{\lambda_n}\right)^n \{\psi\}_r \tag{2.37}$$

Assuming that the eigenvalues are ordered:

$$\lambda_1 < \lambda_2 < \lambda_3 < \ldots < \lambda_n$$

then $\frac{\lambda_1}{\lambda_r} < 1$ and as $n \to \infty$, $\left(\frac{\lambda_1}{\lambda_r}\right)^n \to 0$ and

$$\{v\}_n = \left(\frac{1}{\lambda_1}\right)^n c_1\{\psi\}_1$$

and

$$\{v\}_{n+1} = \left(\frac{1}{\lambda_1}\right)^{n+1} c_1\{\psi\}_1 = \frac{1}{\lambda_1}\{v\}_n \tag{2.38}$$

Clearly $\lambda_1 = \frac{\{v\}_n}{\{v\}_{n+1}}$

In this form, the method seems capable of obtaining only the first eigenpair, however it can be modified to obtain the second and successive eigenpairs. This may be achieved in two ways [13] — *matrix deflation* and *iteration vector deflation*. Matrix deflation modifies the matrices to filter out the eigenpair that has been calculated, allowing convergence on the next eigenpair. Iteration vector deflation achieves the same result by operating on the iteration vectors.

Matrix deflation will be used here. In order to suppress the first eigenpair and allow the solution to converge on the second eigenpair, we make use of the orthogonality requirements of the system and the linear independence of the eigenvectors to develop a transformation which will constrain or filter out the first eigenpair, leaving the other modes unchanged. Firstly, since the eigenvectors are linearly independent of one another, any response $\{x\}$ of the structure may be written as a linear combination of the eigenvectors:

$$\{x\} = [\psi]\{P\} \tag{2.39}$$

where $\{P\}$ is a vector of constants determined by the initial conditions. It can be seen that P_1 determines the contribution made to all the elements of $\{x\}$ by the first eigenvector $\{\psi\}_1$. By setting $P_1 = 0$ we can effectively eliminate that component of the response at the frequency of the first mode. Premultiplying equation 2.39 by $[\psi]^{-1}$ we get

$$\{P\} = [\psi]^{-1}\{x\} = [Q]\{x\}$$

and setting $P_1 = 0$ results in the following equation

$$P_1 = q_{11}x_1 + q_{12}x_2 + \cdots + q_{1n}x_n = 0 \tag{2.40}$$

If we choose our trial vector $\{v\}_0$ we can transform it to a new vector $\{\bar{v}\}_0$, ensuring that equation 2.40 is satisfied. The transformation shown below ensures that this will be the case:

$$\begin{bmatrix} q_{11} & q_{12} & q_{13} & \cdots & q_n \\ 0 & 1 & 0 & \cdots & 0 \\ 0 & 0 & 1 & \cdots & 0 \\ \vdots & \vdots & \vdots & \cdots & \vdots \\ 0 & 0 & 0 & \cdots & 1 \end{bmatrix} \{\bar{v}\}_0 = \begin{bmatrix} 0 & 0 & 0 & \cdots & 0 \\ 0 & 1 & 0 & \cdots & 0 \\ 0 & 0 & 1 & \cdots & 0 \\ \vdots & \vdots & \vdots & \cdots & \vdots \\ 0 & 0 & 0 & \cdots & 1 \end{bmatrix} \{v_0\}$$

Solving for $\{\bar{v}\}_0$:

$$\{\bar{v}\}_0 = \begin{bmatrix} q_{11} & q_{12} & q_{13} & \cdots & q_n \\ 0 & 1 & 0 & \cdots & 0 \\ 0 & 0 & 1 & \cdots & 0 \\ \vdots & \vdots & \vdots & \cdots & \vdots \\ 0 & 0 & 0 & \cdots & 1 \end{bmatrix}^{-1} \begin{bmatrix} 0 & 0 & 0 & \cdots & 0 \\ 0 & 1 & 0 & \cdots & 0 \\ 0 & 0 & 1 & \cdots & 0 \\ \vdots & \vdots & \vdots & \cdots & \vdots \\ 0 & 0 & 0 & \cdots & 1 \end{bmatrix} \{v_0\} \ = [S]\{v_0\}$$

All that we require to perform this transformation is the first row of $[Q]$ since all other terms that make up $[S]$ are either unity or zero. To find $[Q]$ we make use of the orthogonality properties stated in equation 2.7. Premultiplying this equation by $[m_r]_{diag}$ and post multiplying by $[\psi]^{-1}$ we get

$$[m_r]_{diag}[\psi]^T[M] = [m_r^2]_{diag}[Q]$$

Now if we look at the first row of these matrices we see that

$$\left[\ q_{11} \quad q_{12} \quad \cdots \quad q_n\ \right] = \frac{1}{m_1}\left\{\ {}_1\psi_1 \quad {}_1\psi_2 \quad \cdots \quad {}_1\psi_n\ \right\}[M]$$

Hence we can determine the matrix $[S]$ that will transform our trial vector to a new vector and ensure that the iterative procedure will converge to the second eigenpair. Once the second eigenpair has been obtained, a new matrix $[S]$ is constructed by finding the second row of $[Q]$. A further application of the iterative process will produce the third eigenpair, the first two pairs having been "swept" out of the solution by the *sweeping* matrix $[S]$. Equation 2.33 may then be represented as

$$\frac{1}{\lambda_r}\{\psi\}_r = [G][S]\{\psi\}_r \tag{2.41}$$

The above procedure experiences numerical difficulties when there is a zero natural frequency. A zero natural frequency occurs when a structure is not fully constrained and rigid body motion is possible. To avoid this problem, the concept of an eigenvalue shift is used. We make a substitution such that

$$\mu_r = \lambda_r - \nu_r \tag{2.42}$$

We are then able to solve for μ_r using the inverse vector iteration method without encountering numerical difficulties and λ_r is obtained by back substitution into equation 2.42.

Subspace iteration method

Equation 2.33 may be restated, using a matrix of p eigenvectors rather than a single vector, as follows

$$[\psi] = [G][\psi][\lambda_r]_{diag} \tag{2.43}$$

$[\psi]$ has p columns, each defining an eigenvector. $[\lambda_r]_{diag}$ contains the eigenvalue associated with each eigenvector. The usual orthogonality properties apply, but it should be noted that equation 2.43 is a necessary and sufficient condition that the vectors of $[\psi]$ are eigenvectors while the orthogonality conditions are necessary but not sufficient. Now the p eigenvectors defined in equation 2.43 form a p-dimensional subspace of the full space. If we iterate using the inverse vector iteration method with p linearly independent vectors $[v]_0$ as our first guesses, then we are iterating with a subspace, denoted E. Each successive iteration produces a new subspace. The iteration procedure can be written as

$$[v]_n = [G][v]_{n-1}\ ,\ n = 1, 2, \ldots \tag{2.44}$$

Using a vector deflation procedure, such as the Gram-Schmidt procedure, the starting vectors are converted into an orthogonal basis. The Gram-Schmidt method [13] uses the fact that if a guess vector is orthogonal to an eigenvector, then it will not converge to that eigenvector. At the first iteration, no eigenvectors have been established, but if the guess vectors form an orthonormal basis, then we can expect convergence to occur in fewer iterations. We first find the projection of the matrix $[G]$ onto the subspace

$$[G]_n = [v]_n^T [G][v]_n$$

This results in the much smaller eigenvalue problem

$$[Q]_n = [\gamma_r]_{diag}[G]_n[Q]_n \tag{2.45}$$

As the solution progresses and the vectors become closer and closer to eigenvectors, $[G]$ tends toward diagonal form. A method such as the generalized Jacobi transformation method [13] may be used for an efficient solution to this problem. We now have the eigenvectors $[Q]$ and eigenvalues γ_r of the projected problem. An improved estimate of the eigenvectors of the original system are found from the reverse projection

$$[\bar{v}]_n = [v]_n[Q]_n$$

These vectors are then subjected to the Gram-Schmidt orthogonalisation procedure and then used as the new guess vectors.

In practice it is found that a higher convergence rate is achieved by using more than p vectors in the iteration. A value of the minimum of $2p$ or $p+8$ is found to be effective. The rate at which convergence occurs is also dependent on the choice of starting vectors. If the vectors are chosen in such a way that they excite those parts of the structure with small stiffness and large mass, then fewer iterations will be required to obtain convergence. This is due to the fact that, as we have seen from the discussion of the inverse iteration method, convergence occurs on the lower modes. From equation 2.6 it can be seen that large mass and small stiffness implies a low natural frequency. Intuitively, a vector that displaces the degrees of freedom with highest mass and lowest stiffness would represent the lowest mode of vibration. In essence, fewer iterations are required if the starting vectors are close to the eigenvectors. An example of a scheme for selecting the starting vectors is the one used in the MODEL SOLUTION code of I-Deas [8]. The first vector is chosen as the diagonal of the mass matrix. This ensures that every degree of freedom associated with mass is excited. The remaining vectors are each given a value of unity at the degrees of freedom with the highest ratio of mass-to-stiffness as determined by comparing the terms on the diagonals of the mass and stiffness matrices. On either side of the values of unity, three degrees of freedom are given a "perturbation" value of 0.01, but only if a value of unity or another perturbation has not been assigned to this degree of freedom in any of the remaining vectors. This constraint ensures that all the vectors, other than the first, are orthogonal. This scheme is presented below for four start vectors

$\frac{m}{k}$	*vector* 1	*vector* 2	*vector* 3	*vector* 4
3	18	1	0	0
.3	2	.01	0	0
2	8	0	1	0
1	5	0	0	1
.5	3	0	.01	0
.05	.2	0	.01	0
.03	.2	0	0	.01

The method is well suited to solving for a reasonably small number of eigenpairs (less than 20) [13] in a system of equations that has many hundreds or thousands of degrees of freedom. This is usually the case in practical FEM problems, where the model may consist of a few thousand degrees of freedom and only the first ten modes of vibration are of interest. If a large number of eigenpairs is sought, the method becomes more costly and can encounter problems with computer storage requirements. Usually the lower modes of a structure are the ones of most interest and this drawback is not considered to be a major one.

2.4.2 Reduction of Mass and Stiffness Matrices

Often a problem may be of such a size that even methods such as subspace iteration cannot produce an economical solution. In such cases it is desirable to reduce the size of the problem. One such procedure is that proposed by Guyan [20].

The nodal displacement vector $\{U\}$ of the FEM model may be partitioned into two parts as follows

$$\{U\} = \left\{ \begin{array}{c} \{U_1\} \\ \{U_2\} \end{array} \right\}$$

In order to reduce the size of the problem, we assume that the *slave* displacements $\{U_2\}$ are uniquely related to the *master* displacements $\{U_1\}$:

$$\{U_2\} = [L]\{U_1\}$$

therefore

$$\{U\} = \left[\begin{array}{c} [I] \\ [L] \end{array} \right] \{U_1\} = [Z]\{U_1\} \tag{2.46}$$

Substituting equation 2.46 into equations 2.28 and 2.29, the kinetic and potential energies of the system may be written as

$$T = \frac{1}{2}\{\dot{U}_1\}^T[Z]^T[M][Z]\{\dot{U}_1\} \tag{2.47}$$

and

$$S = \frac{1}{2}\{U_1\}^T[Z]^T[K][Z]\{U_1\} \tag{2.48}$$

Substituting equations 2.46 and 2.48 into the Lagrange equation 2.25 we get

$$[Z]^T[M][Z]\{\ddot{U}_1\} + [Z]^T[K][Z]\{U_1\} = 0$$

The problem has been reduced to one with only the degrees of freedom of the master degrees of freedom. It can be seen that the reduced mass and stiffness matrices are

$$[M]^* = [Z]^T[M][Z] \tag{2.49}$$

and

$$[K]^* = [Z]^T[K][Z] \tag{2.50}$$

The relation between the aster and slave degrees of freedom is found using engineering judgment and intuition. We assume that any displacement pattern which may occur is the same as that obtained by giving the master degrees of freedom the same displacements they had in such a pattern. In other words, if we displace the master degrees of freedom, the slaves will follow in a manner determined only by the stiffness and geometry of the structure. Mathematically, the stiffness matrix is partitioned in the same way as the displacement vector, forces $\{F_1\}$ are applied to the masters and no forces are applied to the slaves:

$$\left\{ \begin{array}{c} \{F_1\} \\ 0 \end{array} \right\} = \left[\begin{array}{cc} [K]_{11} & [K]_{12} \\ [K]_{21} & [K]_{22} \end{array} \right] \left\{ \begin{array}{c} \{U_1\} \\ \{U_2\} \end{array} \right\}$$

from which it can be seen that

$$[L] = -[K]_{22}^{-1}[K]_{21} \tag{2.51}$$

The mass matrix is partitioned such that

$$[M] = \left[\begin{array}{cc} [M]_{11} & [M]_{12} \\ [M]_{21} & [M]_{22} \end{array} \right]$$

Substituting equation 2.51 into equations 2.50 and 2.49

$$[K]^* = [K]_{11} - [K]_{12}[K]_{22}^{-1}[K]_{21}$$

$$[M]^* = [M]_{11} - [M]_{12}[K]_{22}^{T}[K]_{21} - [K]_{21}^{T}[K]_{22}^{-1T}([M]_{21} - [M]_{22}[K]_{22}^{-1}[K]_{21})$$

These expressions can be simplified further using the fact that $[K]_{21} = [K]_{12}^T$ and $[M]_{21} = [M]_{12}^T$.

The reduced stiffness matrix retains all the information contained in the original matrix, hence there is no approximation inherent in the reduced stiffness matrix. However, the reduced mass matrix has combinations of stiffness and mass terms, indicating that some approximation has resulted.

The much reduced problem may now be solved with a considerable saving in computing effort. The full mode shapes may be recovered by reversing the transformation of equation 2.46. The results obtained using the above reduction rely strongly on the selection of the master degrees of freedom. The master degrees of freedom must be able to represent the modes of the structure which are of interest and should include degrees of freedom that are expected to contribute significantly to the kinetic energy of the modes of interest. Rotational degrees of freedom and degrees of freedom not in the plane of interest are usually the first priority for slaves, followed by degrees of freedom with low mass-to-stiffness ratios. The effect of the reduction is to raise the lower frequencies due to the constraints imposed while the higher frequencies are not represented at all. The latter may be used to advantage in certain situations, for example in a structure composed of beams and plates. We may not be interested in the numerous local modes of the plates, but rather the main structural modes. The plates contribute to the mass and stiffness properties of the structure and must be modelled. By choosing the master degrees of freedom to model the main structural modes, the local modes will be "missed".

2.4.3 Dynamic Response

While the previous sections have dealt with methods of obtaining the eigenvectors and eigenvalues of the undamped free-vibration system, it now becomes necessary to examine the dynamic response of the structure to some excitation. For the moment we will not concern ourselves with how the damping matrix of the system is set up in the finite element method. The response to an excitation is obtained by integrating the equations of motion. An analytical solution is generally not possible and numerical integration techniques are used. There are two basic approaches to the problem — the *mode superposition* and *direct integration* methods [13,14,15]. The mode superposition method transforms the problem into a set of decoupled equations. This means that the there is an independent equation for each degree of freedom, each analogous to the equation for a single degree of freedom system. The decoupled equations are solved using numerical integration or by evaluating the Duhamel integral [13] and the response is obtained by superposition of the results for each decoupled degree of freedom. In the direct integration method, the coupled equations are integrated directly — there is no transformation before the integration.

The mode superposition method is suitable if only the low frequency modes are needed to describe adequately the response. This will be determined by the frequency content of the excitation. In essence, if the excitation has a frequency content in the range ω_1–ω_2, then all modes in that range must be used in the superposition. A few modes are easily extracted from a very large system using eigenvalue extraction techniques such as the subspace iteration method. If the frequency content of the excitation spans a very large frequency range, then a large number of modes will have to be extracted at great computational effort. In such a case, the direct integration method is preferred. There are many such methods available. Explicit methods solve the equations of motion at time t to predict the response at time $t + \Delta t$, while implicit methods solve the equations at time $t+\Delta t$ to predict response at time $t + \Delta t$. Explicit methods are unstable unless Δt is small enough — conditionally stable, while implicit methods are stable irrespective of Δt — unconditionally stable. Generally, the smaller the time step used, the greater is the accuracy obtained and the greater is the computational effort required for the entire solution. The time step chosen for explicit methods is based on stability requirements and it is found that accuracy requirements are usually exceeded by this choice. For implicit methods, the time step is chosen by considering the highest frequency of interest. The response will be modelled accurately below this frequency and no computing effort will be expended in modelling the response outside the frequency range of interest. Finally, the mode superposition method is based on the assumption that the system is linear, while direct integration methods are able to handle non-linear systems. The mode superposition method is of particular interest and is discussed next.

Mode superposition method

This method is particularly effective when the damping is proportional. The equations of motion for the proportionally viscous damped system are

$$[M]\{\ddot{x}\} + [C]\{\dot{x}\} + [K]\{x\} = \{f\}$$

and we recall that the undamped system eigenvectors are also [C]-orthogonal and that $c_r = 2\omega_r\zeta_r m_r$. Thus these equations may be decoupled by transforming to the generalized coordinate system $\{g\}$ via the following coordinate transformation:

$$\{x\} = [\phi]\{g\}$$

Using this transformation and premultiplying the equation of motion by $[\phi]^T$ (the mass normalized mode shapes) we get

$$[\phi]^T[M][\phi]\{\ddot{g}\} + [\phi]^T[C][\phi]\{\dot{g}\} + [\phi]^T[K][\phi]\{g\} = [\phi]^T\{f\}$$

Using the orthogonality conditions, this reduces to

$$[I]\{\ddot{g}\} + [2\omega_r\zeta_r]_{diag}\{\dot{g}\} + [\omega_r^2]_{diag}\{g\} = [\phi]^T\{f\}$$

Each equation corresponds to a mode of vibration. These decoupled equations may now be solved using the methods of direct integration. The solution in terms of the original coordinate system is found by applying the reverse transformation.

If we know that the excitation will only excite the lower modes, we need only include such modes in the above equations, with the accompanying reduction in size of the problem to be solved. Clearly an eigenvalue extraction must be performed first in order to determine the required mode shapes. While this is a large computational task itself, the cost involved will be offset if the response to a number of load cases is to be calculated. The eigenvalue extraction need only be done once and the mode superposition analysis done for each load case, whereas if direct integration methods were used, they would have to be done in entirety for each load case. It should be pointed out that although only a few of the generalized coordinates are used in the transformation, all of the original coordinates are included in the solution.

2.4.4 Beam and Shell Elements

A brief description of the elements used in this study is presented here. More information regarding these elements may be found in references [8,9]. The elements were low order elements, using low order polynomials for the shape functions. Generally, such low order elements are too stiff, and very fine meshes are required to achieve reasonable accuracy. However, their performance can be improved by neglecting the strain energy due to shear in the formulation and by using the dicrete Kirchoff assumption that the shear deformation is zero at certain discrete points of the element [13]. This formulation has the advantage that low order elements can provide satisfactory accuracy at a cost lower than that incurred by using higher order elements. A comparison of results from the literature [27] and ABAQUS and MODEL SOLUTION FEM models indicated that good accuracy could be expected from the low order elements of both codes. Ten two-noded beam elements were used to model a cantilevered steel beam 1.5 m long and of solid rectangular section 120 mm x 50 mm. The results are summarized in Table 2.1. The FEM models included the effects of shear while the theoretical model did not. As a result, the natural frequencies of the FEM models should be lower than the former and the results bear this out.

ABAQUS elements

Two-noded (B31) and three-noded (B32) beam elements and four-noded (S4R) and eight-noded (S8R) shell elements were used. Each node has three translational and three rotational degrees of freedom associated with it. These elements follow Timoshenko beam theory [9] — they allow transverse shear deformation. It is assumed that the beam cross-section does not deform and warping of the cross-section does not occur. Plane sections remain plane. The B31 elements are based on linear interpolation polynomials (shape functions) while the B32 elements are based on quadratic interpolation polynomials.

The shell elements used were S4R four-noded and S8R eight-noded elements, implementing the discrete Kirchoff assumption. Each node has three translational and three rotational degrees of freedom associated with it.

MODEL SOLUTION elements

Two-noded "linear" beam elements and four-noded "linear" shell elements were used. The beam elements approximate Timoshenko beam theory, but Euler-Bernoulli beams may be modelled by setting the shear area ratios to zero [8]. The shell elements approximate Kirchoff shell theory — deformation due to transverse shear is not included. In both beam and shell elements, each node has three translational and three rotational degrees of freedom.

2.5 DUAL EMA-FE. _ APPROACH

The impression may have been created that the finite element method provides the analyst with a foolproof modelling tool. All he has to do is break the structure down into a number of elements, the system matrices will be calculated accurately and all further calculations will produce accurate results. Unfortunately, this is not the case. While the system matrices for a given assemblage of elements are readily and accurately calculated, the crux of the matter lies in whether or not the assemblage of elements accurately represents the structure. The answer to this question is determined by the skill and experience of the FEM modeller. The modeller will determine the types of element used and how the structure is built up from those elements. The experience of the modeller will enable him to decide which features must be modelled carefully and which features are less important. There will always be a trade off between the accuracy required and the computational and modelling effort required.

Similarly, EMA does not provide a foolproof tool for experimentally determining a structure's dynamic properties. The type of excitation, measurement methods and curve fitting procedures are all quantities in which the knowledge and skill of the experimenter play a very large role. The techniques used have a strong influence on the results obtained and must be selected to ensure that the results satisfy the final purpose of the test.

The fact that there is a certain amount of uncertainty present in results predicted by FEM and measured by EMA was highlighted by two surveys [25] designed to assess state-of-the-art measurement and prediction methods. In one survey, test pieces were circulated to various organizations who were then asked to measure a particular FRF. The survey showed that there was some scatter in the measurements. In the other survey, detail design data for a simple structure was provided to a number of organizations who were asked to analytically predict certain dynamic structure properties, including an FRF. There was a large amount of scatter in the predictions. While some predictions were close to experimentally measured results, others were rather poor. The surveys showed the need for good quality measured data in the use of EMA and that there is a very clear need for experimental validation of analytical models.

Before the advent of FEM, the engineering community was incapable of properly analyzing the dynamics of large structures. As a result the technique of EMA grew to prominence as a method for identifying deficiencies in existing structures. EMA was used largely as a cure for dynamics problems that could not be prevented in the design stage. Today, through the use of FEM, the engineering community is far more capable of analyzing structural dynamics. However, EMA continues to thrive both as a trouble shooting tool and as a means of validating FEM models. Recent trends have been to use EMA and FEM together as an effective design and diagnostic tool. In this study the term *dual* refers to the combined use of the techniques of FEM and EMA. It has no mathematical connotations.

The dual approach can also be used in the design phase of a product. Obviously in the initial stages there would not be a product to conduct an experimental analysis on, but once a prototype has been built, EMA can be used to validate the analytical models and shortcomings in the design can be overcome without the expense of constructing numerous prototypes. It has been shown that the FEM cannot construct a meaningful damping matrix for a real structure. Since damping plays a very important part in the response characteristics of a structure, this leads to the question as to how we can use the FEM to analyze the forced response of a structure. The answer to this question is found in using (for example) the mode superposition analysis described above in conjunction with damping estimates from EMA — the dual approach. If an experimental modal analysis was conducted, some of the natural frequencies, modal damping factors and mode shapes of the system will be known. The natural frequencies and mode shapes of an undamped FEM model of the structure could then be tuned to reproduce the natural frequencies and mode shapes of the test. Once this has been achieved, the experimental modal damping factors from the modal test can be used as good estimates of the damping factors in the FEM modal superposition analysis.

Table 2.1: Theoretical and FEM frequencies for a cantilever beam

Mode No.	Theory	ABAQUS	MODEL SOLUTION
1	18.425	18.309	18.444
2	44.219	43.804	44.093
3	115.465	112.365	115.031
4	277.116	264.080	288.897
5	323.305	306.904	319.748

Chapter 3

DYNAMIC BEHAVIOUR OF SHAFTS AND CONVEYANCES

Structural problems caused by vibration of mine conveyances are common in the mining industry. A survey [3] conducted on gold mines in South Africa showed that minor structural problems such as the loosening of bolts, fatigue cracking of components and unacceptable vibration levels were encountered. Solutions to these problems were found by using bolts with locking devices, strengthening certain components and by reducing hoisting speeds. Greenway [1] states that more serious structural problems such as the fatigue and overload failure of buntons have been less common. However, with increasing production requirements necessitating larger conveyances and higher hoisting speeds, a long term solution to the problem was desirable. To this end, the Chamber of Mines Research Organization (COMRO), with the assistance of the American based Structural Dynamics Research Corporation (SDRC[1]) embarked upon an extensive investigation into the dynamics of shaft steelwork and conveyances. This research embraced a test and analysis phase and culminated in the production of a set of design guidelines which could be used to avoid the recurrence of dynamics related problems in future shafts.

The research program investigated only skips and much of the test work was carried out at the President Steyn No. 4 shaft, where dynamics related problems had been experienced. The conclusions of the test phase were that the predominant behaviour of the skip was that of a rigid body moving in rotation and translation, elastically restrained by the guide rollers and/or the slipper plates bearing on the guides. The shaft guides are not perfectly

[1]SDRC is a service mark of Structural Dynamics Research Corporation

aligned and it is this misalignment that provides the basic excitation of the lateral motion of the skip. During slow speed operation the guide rollers are able to guide the skip over the imperfectly aligned guides. However at high speed, the guide rollers had insufficient travel and metal to metal contact between the slipper plates and guides occurred. This resulted in higher loading of the shaft steelwork. In cases where the guide rollers are completely inoperative (for example when a roller failure had occurred), severe impacting of the slipper plates on the guides occurred. This phenomenon has been called *slamming* and results in very high loading of the steelwork. Slamming is illustrated in Figure 3.1.

The skip strikes the guide near mid span. As the skip approaches the bunton, the stiffness of the guide progressively increases until the lateral motion of the skip is arrested by the bunton. The skip is catapulted into the opposite guide, the forces involved in the impact being very high. A numerical model [5] was developed to investigate this behaviour. The skip was modelled as a lumped mass representing the effective mass of the skip at the contact point. The guides were modelled as prismatic beams simply supported on springs representing the buntons. The model is shown in Figure 3.2. The skip was given an initial lateral velocity and allowed to impact the guide at a number of points along its length. A numerical time stepping algorithm was used to solve the equations of motion of the mass, taking into account the variation of stiffness of the guide along its length. The computer study indicated that for the President Steyn number 4 shaft skip and steelwork, in the worst case the skip may be catapulted into the opposite guide at 2.7 times the velocity that it struck the first guide. If this gain in lateral kinetic energy was to occur for every impact, the result would be catastrophic. In practice this does not occur because for some impacts kinetic energy is lost rather than gained, hence a limit state response is reached. The conclusions of the computer study were as follows:

- slamming is aggravated by increasing skip mass and higher skip velocity.
- slamming is alleviated if guide stiffness is increased and bunton stiffness is reduced.

Mounting the slipper plates on flexible rather than rigid mountings has the same effect as reducing bunton stiffness and is a more economical manner to reduce slamming than replacing or modifying buntons. This leads to the intuitive conclusion that if the skip was in fact a flexible rather than rigid structure, slamming would be reduced. A study involving a different, more flexible type of skip confirmed this. It may also be seen that by increasing the spacing of buntons and maintaining the stiffness of the guide at mid

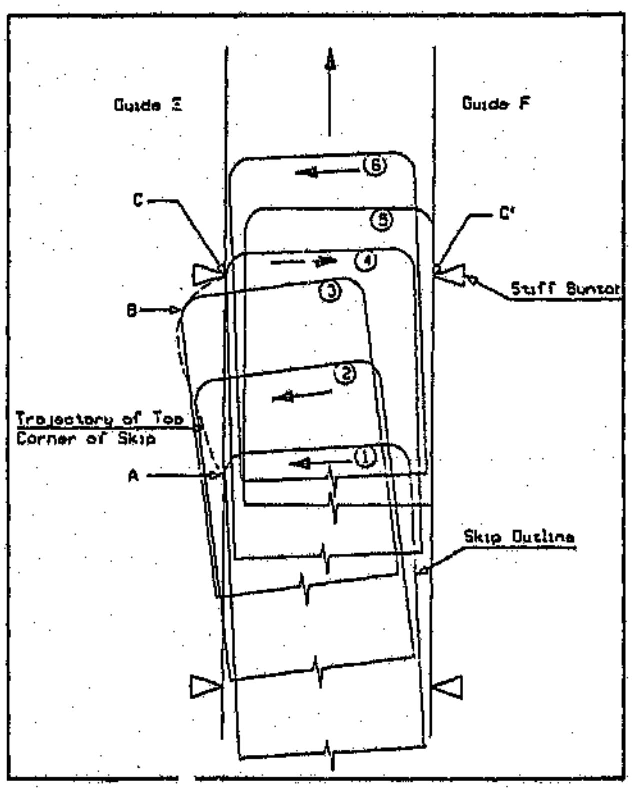

Figure 3.1: Slamming of mine skip

span (by using a stiffer guide), slamming is alleviated. Fewer buntons may be used resulting in a saving in the cost of steelwork.

The design of shaft steelwork was thus governed by the loads imposed by slamming and these loads were strongly dependent on stiffness parameters of the steelwork. The design procedure is thus an iterative one. Using the computer study described above, several dimensionless plots of the important parameters were developed and used as the basis for a set of design guidelines for shaft steelwork [4]. These guidelines have been applied to the design of a new shaft [1] and have resulted in improved slamming behaviour and a substantial saving in the cost of steelwork.

While the above work was based largely on a numerical study of the slamming behaviour of a conveyance, Schmidt and Tondl [11] investigated the vibration of a cage from a completely theoretical angle. The aim of their work was to identify the cause of failure of every second guide bar on alternate sides of the guide system. In their work, the excitation of the conveyance is caused by the variation of stiffness of guide system as the conveyance moves along it. The excitation is termed parametric since one of the parameters governing the system provides the excitation. The model analyzed by Schmidt and Tondl is shown in Figure 3.3. The conveyance is assumed to behave as a rigid body. For a constant travel speed, v, the stiffness of the guide varies with a frequency of $\omega = 2\pi v/l_0$. Assuming that this variation is a harmonic one, the stiffness of the guide at points 1 and 2 is given by

$$k_1 = k_0(1 + \mu\cos\omega t)$$

$$k_2 = k_0(1 + \mu\cos(\omega t - \psi))$$

where k_0 is the average stiffness of the guide, $\psi = 2\pi\frac{l-l_0}{l_0}$ is the phase difference between points 1 and 2 and μ is the half amplitude of the stiffness variation. Assuming that the conveyance moves in the guides with no clearance and that the centroid lies at the centre of the conveyance, the following two equations of motion are obtained by applying Lagranges equation to the system:

$$\ddot{\theta} + \Omega_1^2\{[1 + \frac{1}{2}\mu[\cos\omega t + \cos(\omega t - \psi)]]\theta + \frac{1}{2}\mu[\cos\omega t - \cos(\omega t - \psi)]u\} = 0$$

$$\ddot{u} + \Omega_2^2\{[1 + \frac{1}{2}\mu[\cos\omega t + \cos(\omega t - \psi)]]u + \frac{1}{2}\mu[\cos\omega t - \cos(\omega t - \psi)]\theta\} = 0$$

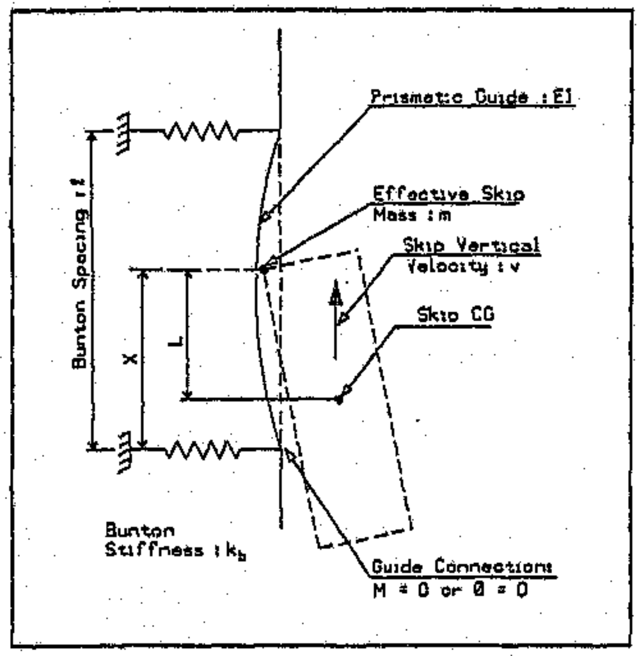

Figure 3.2: Slamming model of mine skip

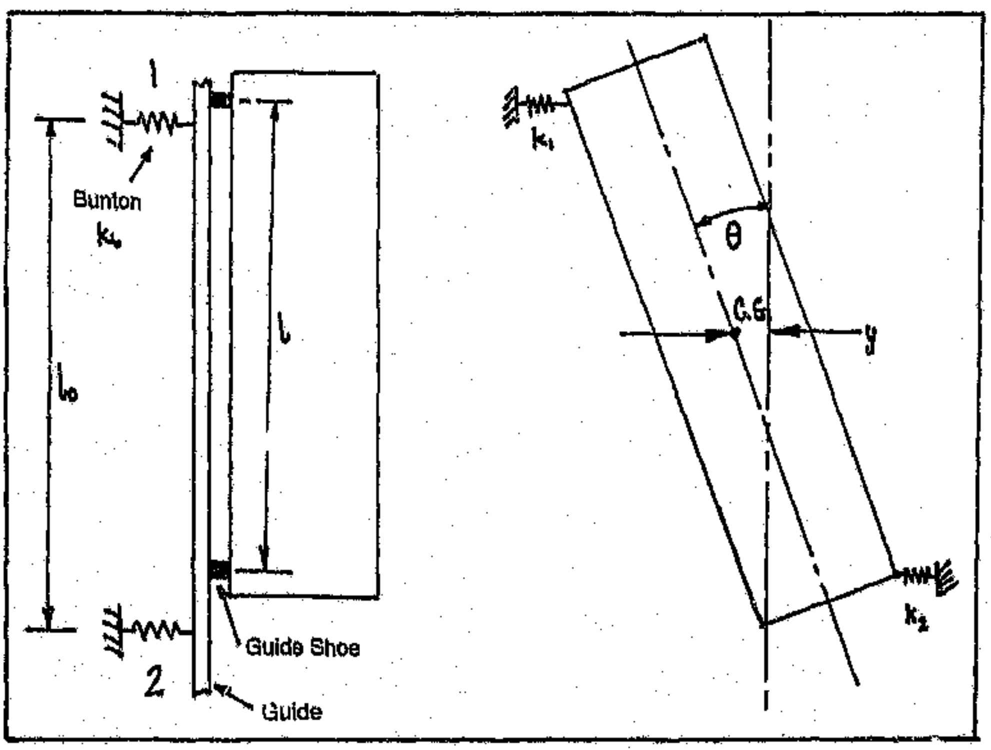

Figure 3.3: Parametric model of mine conveyance

where Ω_1 and Ω_2 are the mean natural frequencies of rotational and translational vibrations respectively and $u = \frac{2v}{l}$. *Instability intervals* — frequency intervals where the system will exhibit a parametric resonance — are defined as follows:
Intervals of the first kind, first order:

$$2\Omega_s - \frac{1}{2}\mu a_{ss} < \omega < 2\Omega_s + \frac{1}{2}\mu a_{ss}$$

Intervals of the second kind, first order:

$$|\Omega_1 + \Omega_2| - \frac{1}{2}\mu\sqrt{a_{12}a_{21}} < \omega < |\Omega_1 + \Omega_2| + \frac{1}{2}\mu\sqrt{a_{12}a_{21}}$$

where $a_{11} = a_{22} = \frac{1}{2}\sqrt{2(1+\cos\psi)}$ and $a_{12} = a_{21} = \frac{1}{2}\sqrt{2(1-\cos\psi)}$.
Using the President Steyn 4 shaft skip and steelwork parameters, $\omega = 16.0$ *rads*$^{-1}$ and the stability intervals are (see Appendix D):
of the first kind, first order:

$$62.3 < \omega < 62.5$$

$$107.1 < \omega < 107.3$$

of the second kind, first order:

$$84.3 < \omega < 85.2$$

These intervals are very narrow, but nonetheless they do exist. While the system is not operating near a parametric resonance, some important conclusions may be drawn from these stability intervals. It may be seen that for $l/l_0 = \frac{1}{2}, 1\frac{1}{2}, \ldots$ the first interval does not exist and for $l/l_0 = 1, 2, \ldots$ the second interval does not exist. Evidently only one of these intervals may be eliminated by choosing the appropriate bunton spacing. However, the width of both intervals can be reduced by reducing the value of μ, that is by reducing the variability of the guide stiffness. This may be achieved by reducing bunton stiffness and increasing guide stiffness, or simply by mounting the slipper plates on flexible mountings. These conclusions are exactly those arrived at by the the numerical study of COMRO and SDRC.

The above results were obtained by assuming that the conveyance moved in the guides with no clearance. Schmidt and Tondl go on to investigate the effect of clearance. For the case where the conveyance length is an integer multiple of the bunton spacing (this is very nearly the case for the President Steyn number 4 shaft skip), the equations of motion decouple and may be written in the dimensionless form shown below by making the substitution $\eta = \omega/\Omega_s$, $W = \theta/\theta_0 = u/u_0$ and $\tau = \Omega_s t$. The constants θ_0 and u_0 are the values of rotation and translation respectively, required to take up the clearance.

$$\ddot{W} + f(W-1)(1+\mu\cos\eta\tau) = 0$$

Including linear and progressive damping coefficients b and δ respectively, the equation can be written as:

$$\ddot{W} + (b+\delta W^2)\dot{W} + f(W-1)(1+\mu\cos\eta\tau) = 0$$

A solution of the form

$$W = A\cos(\frac{1}{2}\eta\tau + \varphi)$$

is assumed. A represents the amplitude of the vibrations of the conveyance. A value of unity or less indicates that the conveyance is moving within the clearance space between the guides. Values greater than unity indicate that the conveyance is causing deflection of the guides. Schmidt and Tondl show that the solution is obtained from the equations

$$\frac{1}{2}\eta(b + \frac{1}{4}\delta A^2) = \frac{1}{2}\mu Q\sin 2\varphi \tag{3.1}$$

$$(\frac{1}{4}\eta)^2 - Q = \frac{1}{2}\mu Q\cos 2\varphi \tag{3.2}$$

where

$$Q = \frac{2}{\pi}\left(\arctan\sqrt{A^2-1} - \frac{\sqrt{A^2-1}}{A^2}\right), A > 1$$

and

$$Q = 0, A \leq 1$$

The resonance curve, showing the variation of A with η may be obtained from equations 3.1 and 3.2. The "backbone" curve is given by

$$\eta \doteq s\sqrt{Q}$$

and the "limit envelope" is given by

$$\eta = \frac{\mu Q}{b + \frac{1}{4}\delta A^2}$$

Using values of $\mu = 0.942$ (for the President Steyn steelwork), $b = 0.0$ and $\delta = 0.01$, the resonance curve shown in Figure 3.4 is obtained.

The operating points for the translational and rotational resonances are $\eta = 0.50$ and $\eta = 0.29$ respectively. Similar operating points for the President Steyn No 4 shaft cage can be calculated — $\eta = 0.37$ and $\eta = 0.22$ for the translational and rotational resonances. The cage is a lighter conveyance, resulting in higher resonant frequencies. These points are away from the region of parametric resonance, indicating that an increase in the speed of the conveyances can be accommodated without parametric resonance being encountered.

The parameters in one of the dimensionless plots developed by COMRO and SDRC, namely "dimensionless bunton stiffness", "bunton:guide stiffness ratio" and "dimensionless skip displacement", can be manipulated to be analogous to the parameters η, μ and W respectively, of Schmidt and Tondl. When this is done, the COMRO/SDRC results do not show the same resonance peak characteristic (see Appendix D) found by Schmidt and Tondl. This would seem to indicate that the former data is in the region defined by $\eta < 0.75$ on the latter's resonance curve. An increase in hoisting speed would cause the operating points to move up the resonance curve, approaching the parametric resonance. The position of this resonance is approximately stationary, but the amplification as represented by A increases in inverse proportion to the variability of the guide stiffness. This means that the hoisting speed can be increased substantially (perhaps even doubled) before a parametric resonance is encountered, provided that the shaft steelwork can survive the increased slamming loads. To achieve higher hoisting speeds, the slamming forces must be controlled by correct steelwork design and parametric resonances must be avoided.

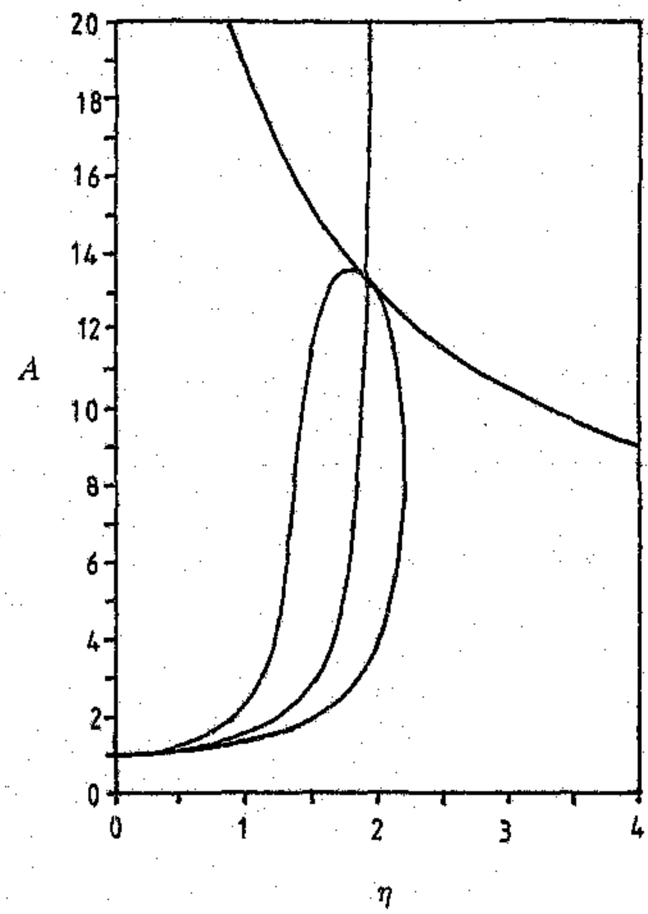

Figure 3.4: Resonance curve for President Steyn steelwork

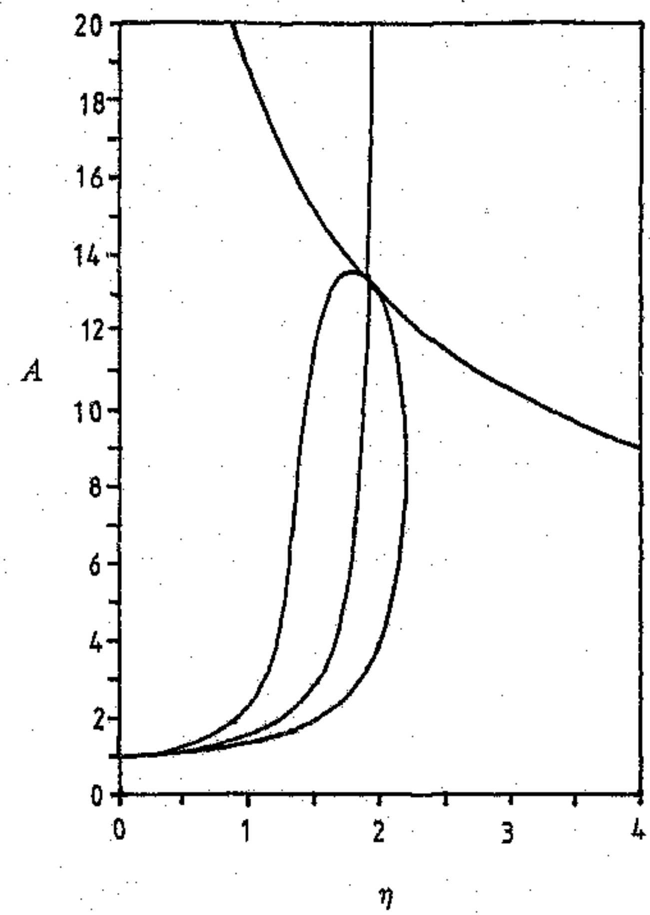

Figure 3.4: Resonance curve for President Steyn steelwork

Chapter 4

DYNAMIC ANALYSIS OF A FLAT PLATE

In order to gain familiarity with the techniques of EMA and FEM, an exercise was carried out on a flat plate. The results of this exercise are presented and discussed in this chapter. Further information on this analysis is presented in Appendix C.

4.1 FEM MODELS

Finite element modelling of this plate was carried out using the ABAQUS code available on the mainframe computer. Several models of the plate were developed using different types of element and varying mesh refinement. The nodes of the models were chosen so that they would coincide with those used in the modal test, in order to compare the mode shapes using the modal assurance criterion. As a result the FEM models are physically smaller because a 10 mm boundary of material is omitted. This means that the structure modelled in FEM actually has higher natural frequencies than the real structure. This was not considered to be a serious limitation because in reality it is very difficult to model exactly every physical detail of a complex structure. It was realized from the start that perfect correlation between the natural frequencies of experimental and finite element models would not be attained. In all of the models the material properties are the same. A summary of the different models is shown in Table 4.1.

The basic approach to modelling the plate was to start with a coarse mesh and increase the mesh density, observing the effect on natural frequency. When satisfactory convergence had been obtained, higher order elements were used to observe if there was any advantage in their use. The first three models employed linear elements and the number of elements and nodes used was progressively increased. The second two models employed fewer elements (of higher order), maintaining a large number of nodes. Many of the models (especially those with the linear elements) produced some spurious numerical modes which were immediately identified by their strange, unrealistic mode shapes. Comparison of results with EMA and theory is presented in section 4.3. Mode shapes for some of the models may be found in Appendix C.

4.2 EXPERIMENTAL MODAL ANALYSIS

4.2.1 Impact Tests

Impact tests on the plate were carried out using a small PCB hammer equipped with a piezoelectric force transducer. The plate was divided into a grid of 50 points and suspended by two strings as shown in Figure 4.1. Three accelerometers were fixed to the plate at points 6, 28 and 50, to measure the response in the direction perpendicular to the plane of the plate. The impact point was moved around as this was simpler and quicker than removing and replacing the accelerometers. This approach also allowed a set of FRF's for three reference locations to be measured simultaneously. In addition, the shifting of natural frequencies which may have occurred as a result of changing the structure's mass distribution by moving the accelerometers could also be avoided. The FRF's were re-numbered according to the reciprocity theorem after the test so that in effect there were 3 reference locations and 50 response locations. This resulted in a set of 150 FRF's.

The menu driven mode of MODAL-PLUS was used to capture the data and perform the curve fits. The menu driven mode was selected because it guides the user through the necessary steps in the acquisition and processing of data. In this way the user would learn the necessary steps in performing a modal test and eventually the faster command mode could be used. The GR 2515 was set up using a baseband of 400 Hz. Approximately 14 resonances were identified in this region. The tip for the impact hammer was selected to give a frequency content of over 400 Hz. The data was averaged over 10 impacts at each point. Frequency response functions were stored. The baseband chosen did not allow the acceleration signals to decay to zero in the time window, hence it was necessary to apply an exponential window to the response signals. The exponential window caused the response signal to decay (artificially) to zero within the window to avoid leakage errors.

Table 4.1: Summary of ABAQUS Plate Models

Model	Element Type (ABAQUS Designation)	Elements	Nodes
1	4-noded quadrilateral (S4R)	6	12
2	4-noded quadrilateral (S4R)	18	30
3	4-noded quadrilateral (S4R)	36	50
4	8-noded quadrilateral (S8R)	10	45
5	9-noded quadrilateral (S9R5)	10	55

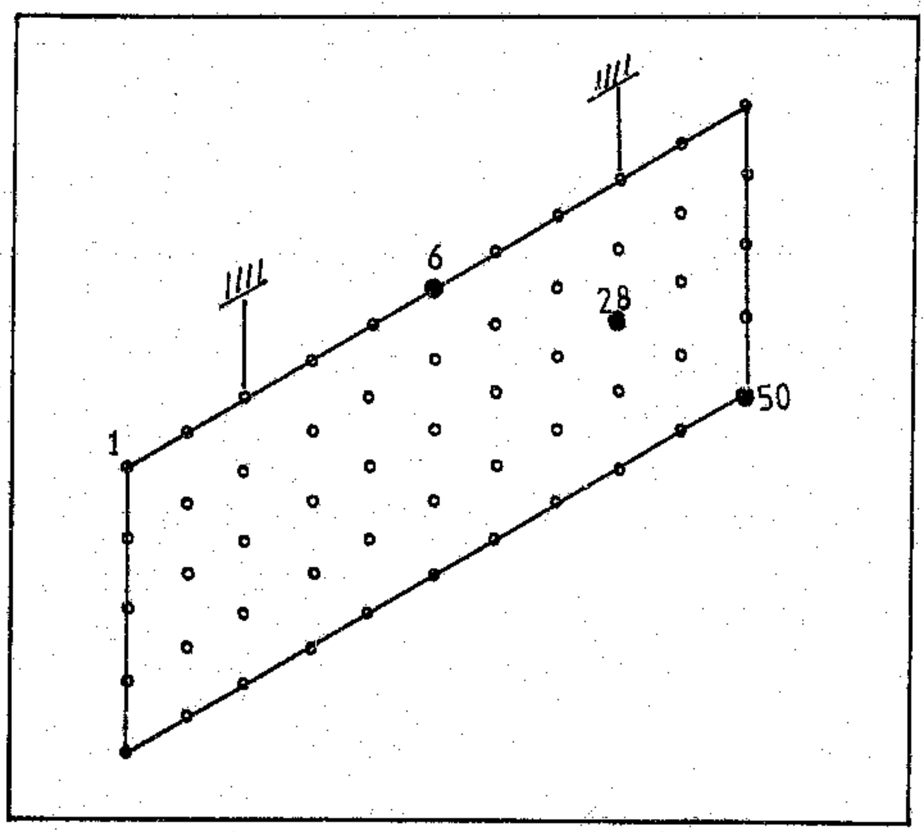

Figure 4.1: Set up for tests on plate

The amplifiers were set up to give an accelerometer signal in the range of minus 1 volt to plus 1 volt (approximately). This meant that the gain of the amplifiers was changed from point to point because response levels vary, depending on the proximity to nodes. The necessary calibration constants in the GR 2515 set-up were accordingly changed. This effected a high signal-noise-ratio for all measurement points. The hammer signal amplification was not changed because the strength of the impact was kept as constant as possible.

Care was taken to allow all ringing of the plate to stop before the next impact was applied. In some instances "double hits" occurred — that is there were two impacts from the hammer in one window. In this case the impact was rejected and not included in the averaged FRF. The coherence was checked after each set of 10 impacts. If it was poor, the test was repeated. Coherence was not stored.

4.2.2 Extraction of Modal Parameters

Before any curve fits were undertaken, two function interpretation tools available in MODAL-PLUS were used to determine the expected number and frequencies of the mode shapes. These functions — the *conjugate summation function* and the *mode indicator function* — are shown in Figures 4.2 and 4.3. Maxima in the conjugate summation function and minima in the mode indicator function indicate the presence of a resonance. Figures 4.4 and 4.5 show two driving point FRF's. Clearly, more resonances are evident in the FRF measured at point 50 than a that measured at point 28. For this reason, this FRF was used in the curve fitting procedures. The polyreference technique requires that a correlation matrix be set up when estimating the modal parameters. To ensure that all resonances were extracted and to allow for the effect of resonances outside of the analysis frequency range, the curve fits were carried out over two ranges: 0–255 Hz and 200–455 Hz. The error plots for these two ranges are shown in Figures 4.6 and 4.7. The number of roots estimated were chosen on the basis of these plots (14 and 16 for the first and second ranges respectively).

Roots which were obviously incorrect were discarded. Analytic functions were generated on the basis of the remaining, "good" roots. These are shown overlaid on the measured function in Figures 4.8 and 4.9. The modal parameters obtained from curve fitting over the two frequency ranges were consolidated into a single set of parameters which could then be used to synthesize functions over the entire frequency range. Because of the overlap in frequency range, one of the modes was identified twice — once in each range — one of them was merely deleted.

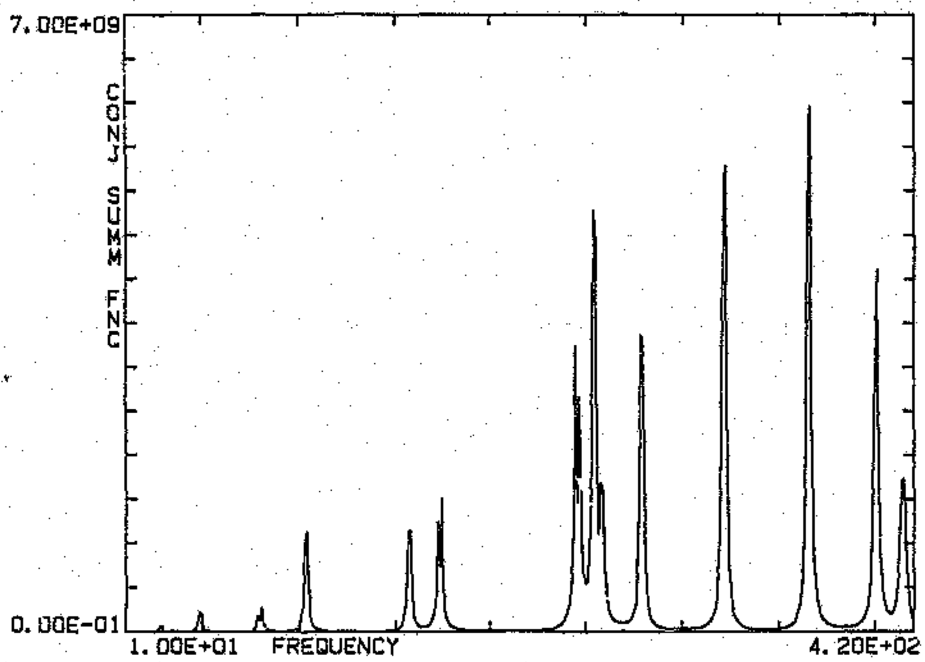

Figure 4.2: Conjugate summation function

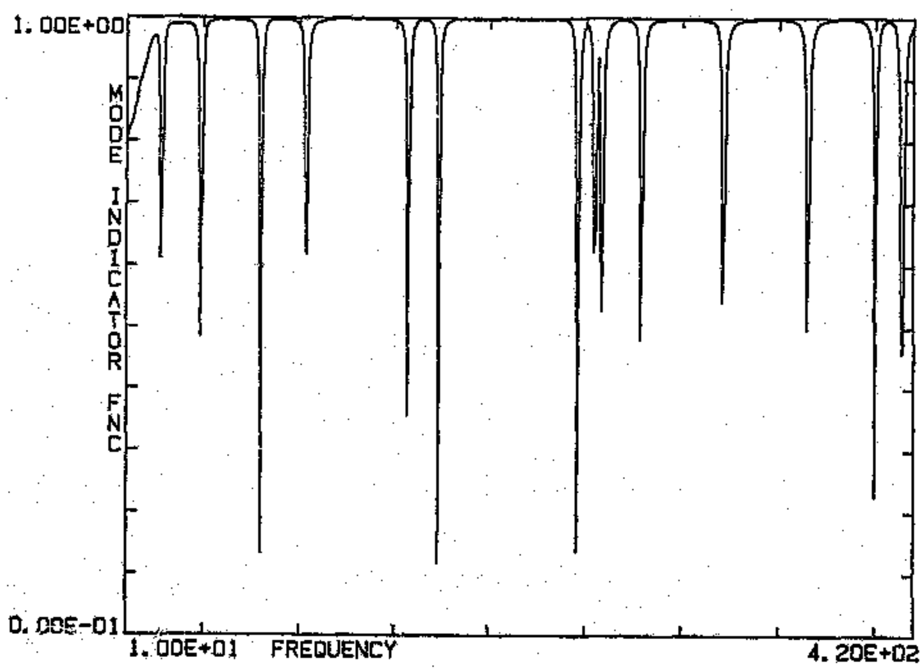

Figure 4.3: Mode indicator function

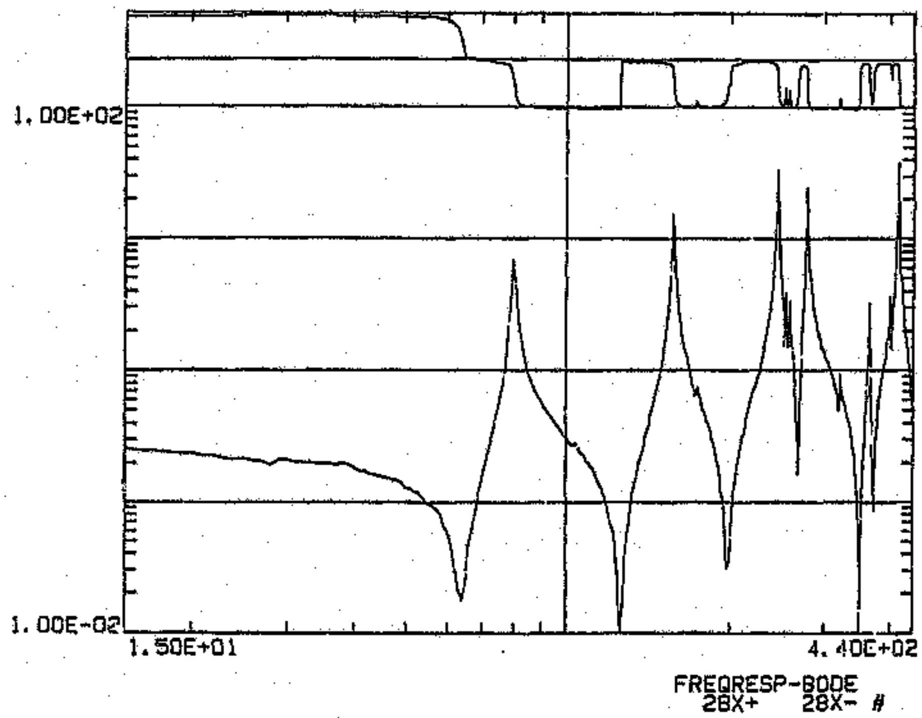

Figure 4.4: Driving point FRF at point 28

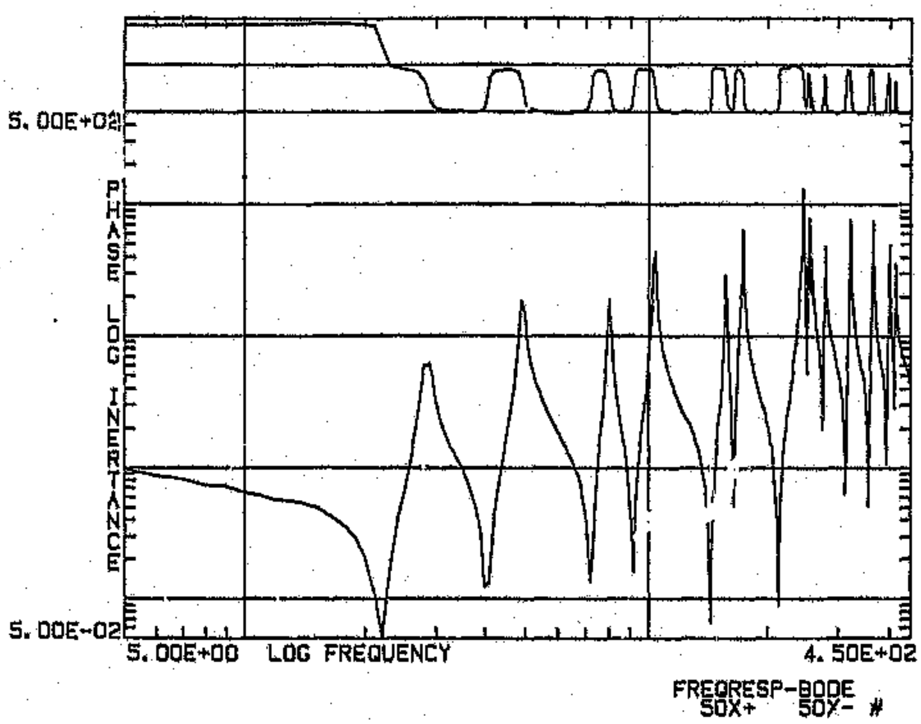

Figure 4.5: Driving point FRF at point 50

Once a set of satisfactory modal parameters had been found, the mode shapes could be estimated. The 14 modes extracted are shown in Appendix C. The total response method was used to estimate the shapes. The modes were real.

4.2.3 Quality of Modal Data

The quality of the modal database was evaluated by visually checking the accuracy of FRF's synthesized by the modal parameters and by carrying out a check on the linear independence of the mode shapes was carried out by means of the Modal Assurance Criteria (MAC).

Figures 4.10 and 4.11 show synthesized FRF's overlaid on the corresponding measured FRF's. The synthesized functions are represented by circles. The database is clearly capable of accurately synthesizing FRF's.

Table 4.2 shows the results of the linear independence check on the mode shapes. Diagonal entries are all 100 % and the matrix is symmetric as expected for an Auto-MAC correlation. The off-diagonal entries are all very low, the largest being 5.0 %. This clearly shows that the modes are linearly independent, as they should be for a good analysis.

Table 4.2: Auto-MAC for EMA Plate Analysis

Modal Assurance Criteria (%)								
Mode no		1	2	3	4	5	6	7
Freq (Hz)		27.39	49.37	80.10	103.59	157.26	173.10	245.83
1	27.39	100.0	0.2	0.1	0.1	4.6	0.7	0.7
2	49.37	0.2	100.0	0.2	0.1	0.0	2.5	1.1
3	80.10	0.1	0.2	100.0	0.3	0.1	0.0	0.7
4	103.59	0.1	0.1	0.3	100.0	0.5	0.5	0.1
5	157.26	4.6	0.0	0.1	0.5	100.0	0.1	0.1
6	173.10	0.7	2.5	0.0	0.5	0.1	100.0	0.3
7	245.83	0.7	1.1	0.7	0.1	0.1	0.3	100.0
8	254.51	3.1	0.2	1.3	3.8	0.0	0.8	0.0
9	258.65	0.0	0.5	2.3	0.1	0.3	0.9	0.2
10	279.36	0.1	0.0	1.1	2.0	0.5	0.1	0.1
11	321.44	4.9	0.1	0.0	0.0	0.1	0.0	0.5
12	365.48	0.4	2.8	0.0	0.1	0.4	3.5	0.7
13	400.22	5.0	1.2	0.4	0.1	3.9	1.5	0.3
14	414.52	2.1	0.1	5.0	0.2	0.6	0.1	0.1

Mode no		8	9	10	11	12	13	14
Freq (Hz)		254.51	258.65	279.36	321.44	365.48	400.22	414.52
1	27.39	3.1	0.0	0.1	4.9	0.4	5.0	2.1
2	49.37	0.2	0.5	0.0	0.1	2.8	1.2	0.1
3	80.10	1.3	2.3	1.1	0.0	0.0	0.4	5.0
4	103.59	3.8	0.1	2.0	0.0	0.1	0.1	0.2
5	157.26	0.0	0.3	0.5	0.1	0.4	3.9	0.6
6	173.10	0.8	0.9	0.1	0.0	3.5	1.5	0.1
7	245.83	0.0	0.2	0.1	0.5	0.7	0.3	0.1
8	254.51	100.0	0.0	0.0	1.6	0.4	0.4	0.1
9	258.65	0.0	100.0	1.2	0.0	0.1	0.4	1.4
10	279.36	0.0	1.2	100.0	0.1	0.0	0.0	1.6
11	321.44	1.6	0.0	0.1	100.0	0.4	0.0	0.5
12	365.48	0.4	0.1	0.0	0.4	100.0	1.1	0.0
13	400.22	0.4	0.4	0.0	0.0	1.1	100.0	0.0
14	414.52	0.1	1.4	1.6	0.5	0.0	0.0	100.0

4.3 CORRELATION BETWEEN FEM AND EMA: MAC

The experimental and FEM results are compared here, using the modal assurance criteria. Tables 4.3 and 4.4 that follow show the Cross-MAC for the simplest and most complex FEM models, respectively. The tables for the remaining three FEM models may be found in Appendix C. In all cases the FEM modes are represented by the rows and the EMA results by the columns of the tables. Finally, Table 4.5 is a summary of the natural frequencies of the plate, obtained by means of theoretical methods, FEM and EMA. The "theoretical" natural frequencies of the plate were obtained by assuming that the plate behaved as a slender beam. Equations for natural frequency of transverse vibrations of slender beams may be found in [27]. The formulas given by Blevins [27] for torsional vibrations of slender beams are not accurate for beams of cross section other than circular, hence the torsional vibration natural frequencies were not calculated.

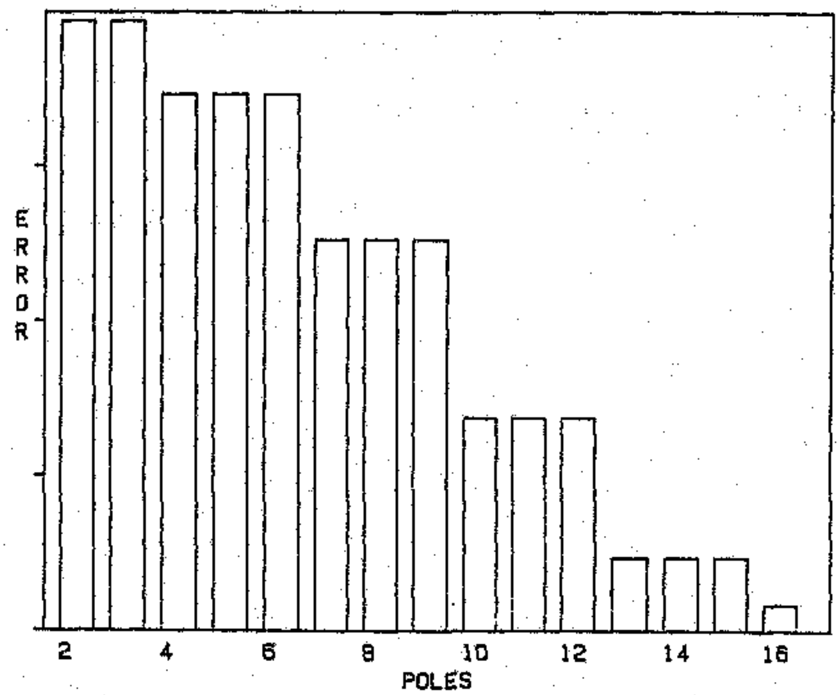

Figure 4.6: Error plot for 0–255 Hz range

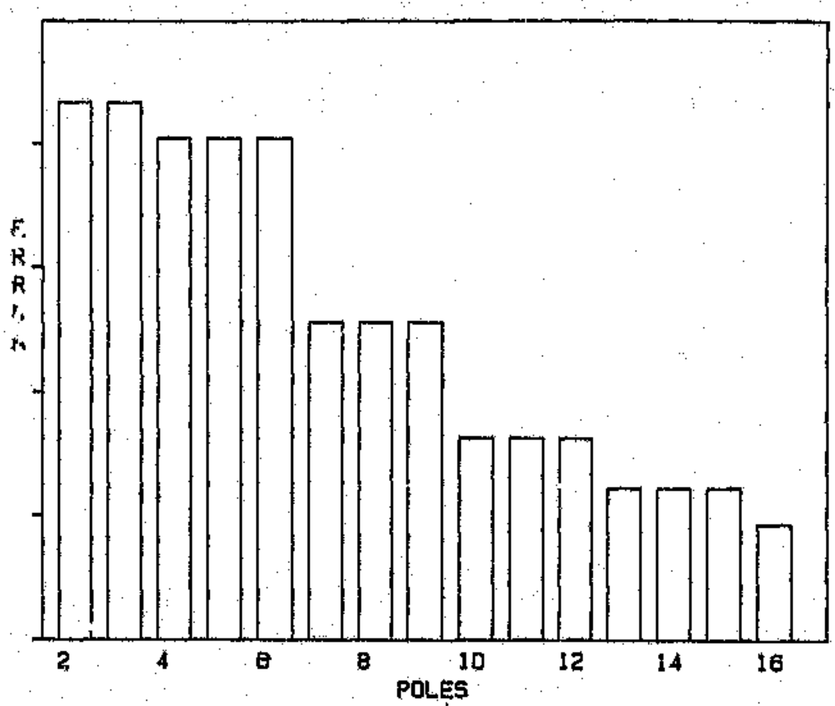

Figure 4.7: Error plot for 200–455 Hz range

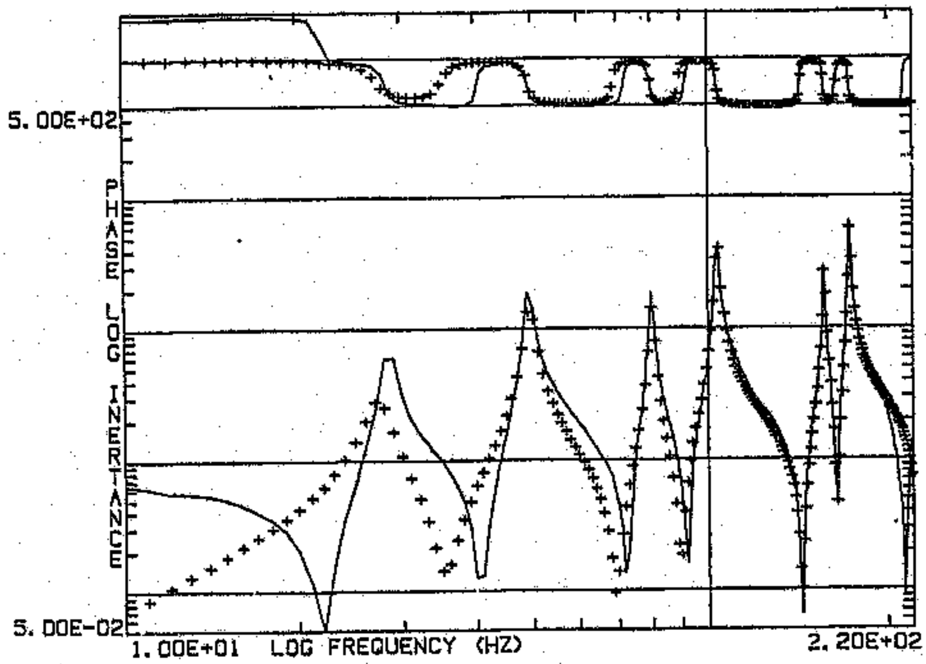

Figure 4.8: Analytic function for 0–255 Hz range

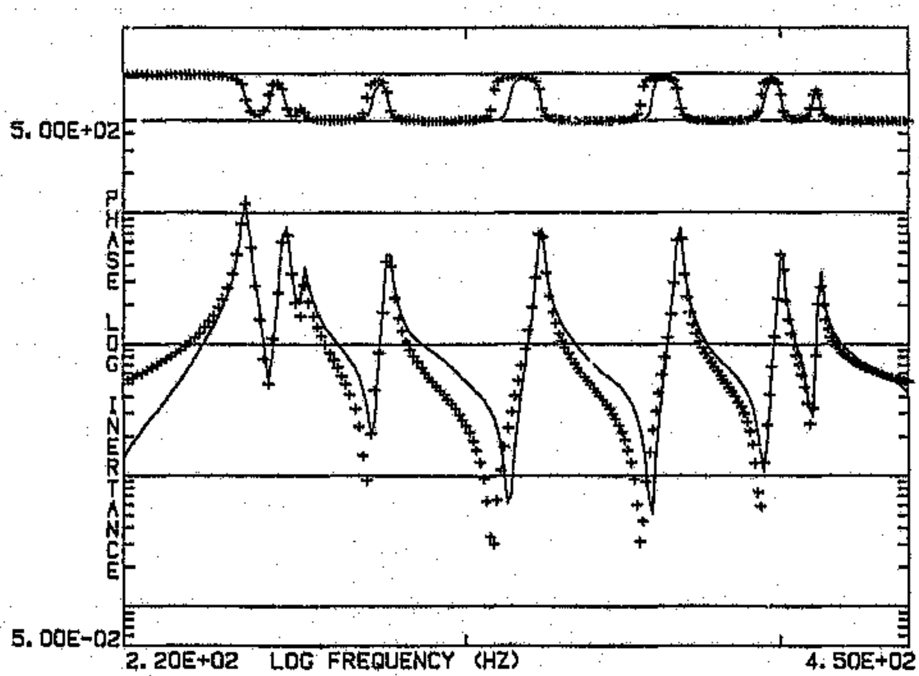

Figure 4.9: Analytic function for 200–455 Hz range

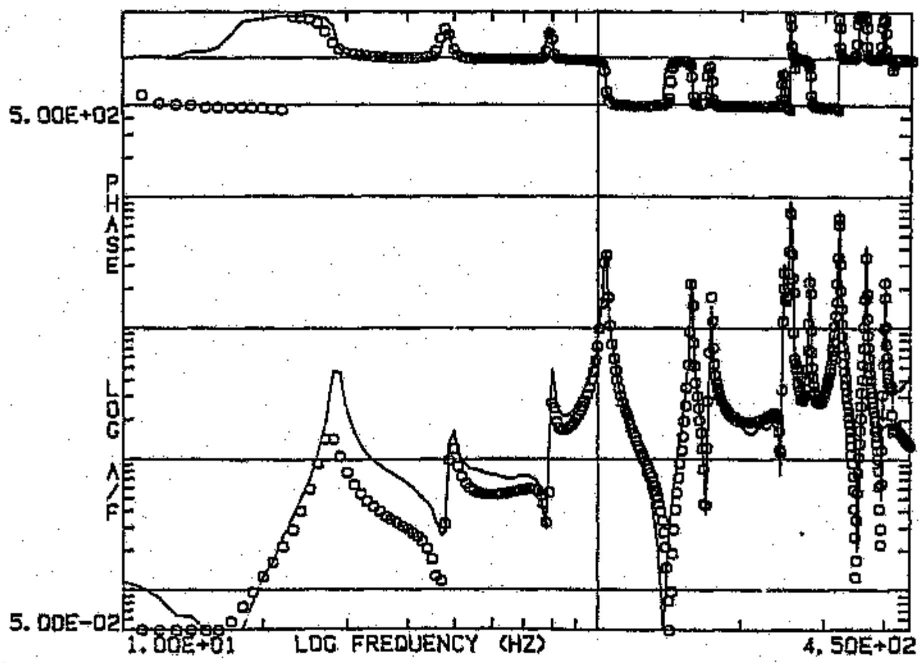

Figure 4.10: Synthesized function: reference 6x+,response 50x-

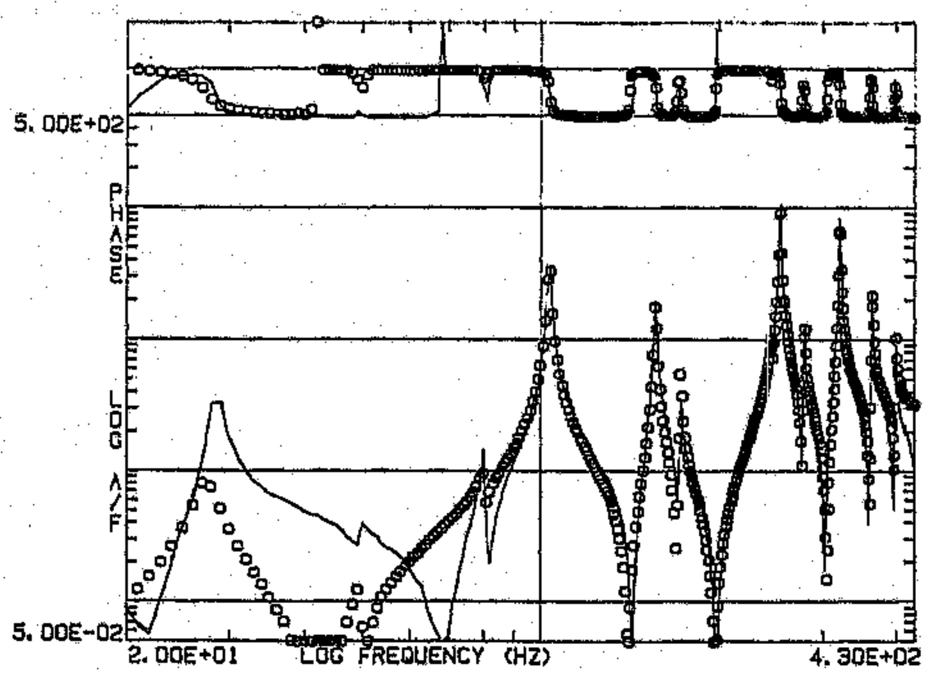

Figure 4.11: Synthesized function: reference 6x+,response 6x-

Table 4.3: Cross-MAC for plate: FEM 1 vs EMA

Modal Assurance Criteria (%)								
Mode no		1	2	3	4	5	6	7
Freq (Hz)		27.39	49.37	80.10	103.59	157.26	173.10	245.83
8	25.07	**96.5**	0.5	0.0	0.0	**83.7**	2.1	2.4
9	42.17	0.0	**92.8**	0.2	0.0	2.0	37.1	0.9
10	59.91	0.0	0.6	0.1	0.6	5.3	**74.3**	2.0
11	77.46	1.5	0.0	0.1	**98.2**	1.1	1.0	3.9
12	81.95	0.0	0.0	**84.8**	0.5	0.2	0.0	0.5
13	101.06	11.0	0.2	0.0	0.0	3.7	0.0	16.9
14	172.47	0.0	0.1	6.1	0.2	0.0	0.0	16.5
15	186.92	0.0	0.1	4.5	0.1	0.0	0.0	16.7
16	211.47	5.6	0.3	0.0	0.1	1.2	0.2	**71.5**
17	228.17	0.4	11.6	0.2	1.0	8.0	**81.4**	3.0
18	228.17	2.2	8.9	0.5	0.2	1.7	**69.9**	0.7
Mode no		8	9	10	11	12	13	14
Freq (Hz)		254.51	258.65	279.36	321.44	365.48	400.22	414.52
8	25.07	0.1	0.0	0.2	19.0	1.4	7.5	1.9
9	42.17	0.0	0.9	0.0	1.0	**74.5**	8.8	0.3
10	59.91	0.6	1.6	0.2	0.3	3.1	0.2	0.0
11	77.46	**73.2**	13.1	7.2	2.1	1.6	0.4	0.1
12	81.95	0.3	0.3	2.0	0.1	0.1	1.5	10.0
13	101.06	0.1	1.6	0.0	**91.8**	7.6	0.6	1.2
14	172.47	6.5	17.3	**64.2**	1.0	0.1	3.1	15.3
15	186.92	6.6	17.1	**65.0**	1.0	0.1	2.9	14.4
16	211.47	15.8	10.9	2.9	7.8	0.0	15.1	2.0
17	228.17	0.6	0.0	5.9	6.4	2.1	1.7	1.6
18	228.17	0.2	9.5	7.9	16.8	9.3	0.1	2.8

Table 4.4: Cross-MAC for plate: FEM 5 vs EMA

Modal Assurance Criteria (%)								
Mode no		1	2	3	4	5	6	7
Freq (Hz)		27.39	49.37	80.10	103.59	157.26	173.10	245.83
7	31.40	**96.5**	0.3	0.1	0.0	5.5	0.7	0.0
8	56.98	0.0	**99.0**	0.3	0.2	0.0	2.2	0.3
9	83.52	0.5	0.0	0.0	**79.8**	0.7	0.9	0.9
10	87.69	0.0	0.0	**98.3**	0.6	0.1	0.0	0.6
11	98.33	0.0	0.0	51.7	0.5	0.0	0.0	3.9
12	121.15	0.1	0.0	0.0	**98.2**	1.1	1.4	0.0
13	174.86	9.3	0.0	0.0	0.1	**94.8**	4.4	0.2
14	198.22	0.0	6.1	0.0	0.3	2.6	**92.8**	1.9
15	286.65	0.0	0.0	7.9	0.1	1.6	0.0	2.4
16	294.45	1.5	0.1	0.3	8.0	0.0	0.1	5.8
17	303.56	2.7	0.2	0.1	0.1	0.2	0.4	**82.5**
18	335.57	0.3	0.0	1.0	0.1	1.0	0.0	5.2
Mode no		8	9	10	11	12	13	14
Freq (Hz)		254.51	258.65	279.36	321.44	365.48	400.22	414.52
7	31.40	0.1	0.0	0.1	3.9	0.3	5.4	2.2
8	56.98	0.1	0.3	0.0	0.0	2.5	0.8	0.1
9	83.52	21.5	2.4	4.3	0.8	0.6	0.1	0.1
10	87.69	0.3	2.9	2.0	0.0	0.0	0.3	4.7
11	98.33	1.0	3.7	28.5	0.5	0.0	2.2	19.8
12	121.15	3.0	0.2	1.4	0.0	0.2	0.1	0.1
13	174.86	0.0	0.1	0.2	0.0	0.1	5.6	0.8
14	198.22	0.2	0.8	0.2	0.0	4.0	1.0	0.0
15	286.65	7.8	**86.3**	0.0	1.2	0.1	1.5	0.5
16	294.45	**72.8**	9.7	8.8	3.5	0.5	0.8	0.2
17	303.56	12.5	0.1	2.9	1.0	0.1	0.7	0.1
18	335.57	4.1	2.5	**83.6**	1.0	0.4	0.2	1.4

Table 4.5: Plate natural frequencies: theory, EMA and FEM

Natural Frequency (Hz)							
Mode	Theory	EMA	FEM 1	FEM 2	FEM 3	FEM 4	FEM 5
1	29.9	27.4	25.1	30.2	30.4	31.4	31.4
2	—	49.4	42.2	46.1	53.4	57.0	57.0
3	82.3	80.1	82.0	81.7	83.5	88.4	87.7
4	—	103.6	77.5	95.1	111.1	120.9	121.2
5	161.4	157.3	—	142.2	164.6	180.3	174.9
6	—	173.1	59.9	148.1	174.8	201.0	198.2
7	246.8	245.8	211.5	—	258.0	311.0	303.6
8	—	254.5	—	—	252.2	304.1	294.5
9	266.8	258.6	—	—	255.2	305.7	286.7
10	—	279.4	186.9	—	295.0	—	335.6
11	—	321.4	101.1	—	300.1	—	—
12	—	365.5	—	—	—	—	—
13	398.5	400.2	—	—	—	—	—
14	—	414.5	—	—	—	—	—

Chapter 5

DYNAMIC ANALYSIS OF A MINE CAGE

5.1 CAGE DESCRIPTION

The mine cage analyzed in this section was the four deck aluminium cage in operation at President Steyn Mine number 4 shaft, shown in Figure 1.3. This cage is constructed mainly from aluminium plates and sections, the only load bearing steel components being the top and bottom transoms and the slipper plates or guide shoes. All structural connections are bolted. The cage has four decks and a mass of about 7 000 kg, with a maximum payload mass of about 8 000 kg. The approximate dimensions of the cage are 10.6 m x 2.9 m x 1.6 m. The major components of the cage are described below:

Transoms: Two pairs of steel I-sections, a pair at the top of the cage, where the rope is attached, and a pair at the bottom of the cage. The top and bottom transoms are joined by the bridle legs.

Bridles: Two legs, each fabricated from aluminium plate and angle sections. These are the main structural members joining the top and bottom transoms.

Top Section: This part of the cage is made from heavy aluminium plates and provides the load path between top transoms and bridles and corner angles.

Corner Angles: Aluminium angles forming the corners of the cage.

Decks: Each deck comprises a network of aluminium beams, covered with an aluminium plate and provides the area on which the loads rest. There are four decks.

Guide Shoes: These are steel wear plates that locate the guides and protect the cage from damage should metal-to-metal contact occur between the cage and the shaft guides. There are five guide shoe locations along the length of the cage.

Guide Rollers: Solid rubber tyres with a spring loaded mechanism to guide the cage over irregularities in the guide profile.

Screens: Light aluminium plates covering the side and back of the cage to protect the occupants from falling debris and contact with the shaft steelwork.

Doors: Roller shutter doors cover the entrance to each deck.

This cage was designed to operate in either two or three guide compartments. In the two guide configuration, the guides run in the channels formed by the bridle legs. In the three guide configuration, the guides run in the channels formed by the guide shoes at the rear of the cage and at the front two corners of the cage — Figure 5.1.

5.2 EXPERIMENTAL MODAL ANALYSIS (EMA)

It is well known that an impact modal test does not produce modal data of exceptional quality when used on large and complex structures. However it is equally well known that it is by far the fastest, cheapest method of modal testing. The latter factor coupled with limited equipment resources resulted in the use of the impact technique for tests on the cage. A cage which had been in use in the shaft for several months, and which was removed for modifications to be made, was employed for the tests.

5.2.1 Impact Tests

A large hammer had been successfully used in other similar tests conducted by COMRO/SDRC[1] on a skip. A similar hammer was thus designed and

[1]SDRC is a service mark of Structural Dynamics Research Corporation

equipped with a specially designed proving ring type load cell. The mass of this hammer was approximately 70 kg and it could be fitted with various sizes of rubber tips. Design considerations and a description of this hammer may be found in Appendix B. The cage was suspended in the President Steyn number 4 shaft conveyance changing device, from the normal suspension point at the midpoint of the top transoms. This meant that the cage was free to move in all directions except vertically. Because the cage was suspended from a single point in a very confined space, some means of preventing it from swinging and snagging the support structure was necessary. Rubber hose was used to restrain the bottom of the cage. This resulted in a fairly flexible restraint which would prevent the cage from snagging the support steelwork and at the same time not affect the desired boundary conditions. A total of 25 points were selected for measurement purposes. A schematic representation of the cage test set up is shown in Figure 5.2.

Two accelerometers were fixed to a mounting block to allow rapid movement from one point to another. A small steel disc with a hole drilled and tapped at its mid point, was glued to each of the measurement points. The accelerometer block was then merely screwed to this disc. At each measurement location, the block was positioned to measure accelerations in the horizontal plane only (along the x- and y-directions). The measurement points and axis system are shown in Figure 5.3. The point of excitation was chosen as point 2, in the negative x-direction. This excitation point was not changed throughout the tests. The impact hammer was suspended from a point in the support structure. The impact point had to be restricted to a small area (about 400mm x 200mm) that was stiff enough to prevent the occurrence of local damage. Special care had to be taken to prevent missing this area because the cage swayed under the effects of wind as well as the impacts.

The initial impact tests carried out on the cage indicated that the hammer was not imparting sufficient energy to the cage in the frequency range of interest. This problem was overcome by trimming the rubber tip, effectively increasing its stiffness, until the cage was excited over a sufficient frequency range, ie. 0–40 Hz. Figure 5.4, a plot of the hammer input spectrum shows clearly how the energy transmitted to the cage drops off sharply above frequencies of about 40 Hz. Although the FRF's were captured in the 0–64 Hz range, the impact hammer was not capable of supplying energy to the system above a frequency of about 40 Hz, hence the analysis was conducted in the 0–35 Hz range.

The coherence function (based on the average of 8 impacts at each point) was calculated for each transfer function and used to check that measurements had been properly made. As with the test conducted on the flat plate, care was taken to avoid double impacts. The signal levels were adjusted to reasonable levels at each measurement point and the amplifier gains were very carefully noted so that the correct calibration factors could be used when the tape recorded data was replayed. Figure 5.5 shows Bode plots of FRF's measured at point 4 in the positive x- and y-directions. It is apparent that FRF's obtained using accelerometer responses not in the direction of the impact, ie. in the y-direction, were not as "clean" as those obtained using responses in the x-direction. This was attributed to the fact that there was little response in the y-direction and consequently the signal-to-noise ratio was low.

Figure 5.6 shows the coherence for measurements taken in the x- and y-directions, for the average of 8 impacts. The frequency range covered is 0–64Hz, the frequency baseband used in the measurement of the FRF's. For the function (upper figure) where the response was measured at point 12 in the negative x-direction, the coherence is close to unity, but appears to deteriorate above 40 Hz. This is probably caused by the fact that above 40 Hz, the hammer was not supplying much energy to the cage, hence responses and the signal-to-noise ratio would be low. For the function (lower figure) where the response was measured at point 8 in the positive y-direction, the coherence is low in many areas, not just above 40 Hz. This is probably a result of poor signal-to-noise ratio caused by the small responses obtained in the y-direction. On the whole, the coherence functions indicated that the measurements had been adequately taken.

The position of the impacts was not changed, but the two accelerometers were moved to each of the 25 measuring points after 10 impacts had been recorded at each. This resulted in sufficient data for a set of 50 FRF's to be constructed. This database was transferred from the GR 2515 to the MicroVax II, where SDRC's I-DEAS software was used for all further processing.

5.2.2 Extraction of Modal Parameters

The mode indicator function was used to establish the number and frequency of modes in the frequency range of interest. Figure 5.7 shows that seven modes are identified.

I-Deas modal analysis software offered several methods of extraction of modal parameters, among them the SDOF circle fit, the polyreference method and the complex exponential method. The complex exponential method was chosen as it was capable of a multi-degree-of-freedom (MDOF) curve fit. The complex exponential method proved to be a very fast and effective method of estimating the poles. Analytic frequency response functions were generated using these poles and the best correlation between the measured FRF and the analytic FRF was obtained with seven poles — seven resonances were identified in the 0–35 Hz frequency range. The FRF used for estimating the poles and the analytic function generated using these poles are shown overlaid in Figure 5.8, the analytic function is indicated with crosses. The upper part of the figure shows the analytic curve without the residuals added, while the lower includes the residuals. The curve with residuals is clearly a better fit than that without, especially in the low frequency area.

Having obtained a satisfactory curve fit, the mode shapes were extracted. The mode shapes were essentially real. The mode shapes are shown in Figures 5.9– 5.12. Mode 1 depicts the first bending mode of the cage, in the plane of the guides. Modes 2,3 and 4 are very similar and represent what is essentially the second bending mode, also in the plane of the guides. Modes 5 and 6 show flexure of the lower part of the cage (also in the guide plane). Finally, mode 7 is the third bending mode of the cage, also in the plane of the guides. Further discussion of the mode shapes and the reasons for some of them having similar appearance may be found in the section 5.2.3.

5.2.3 Quality of Modal Data

The quality of the modal database may be assessed by examining:

- the accuracy with which the model can synthesize FRF's other than the one used in extracting the modal parameters
- the linear independence of the mode shapes extracted, using the Modal Assurance Criteria

Figure 5.13 shows the synthesized function obtained for a measured function, namely for the transfer function measured between points $2x$- and $17x$-. The synthesized function is indicated by circles. The lower figure includes the residuals.

The fact that the synthesized function resembles the measured function closely is evidence that the modal model is a good one, at least in the frequency range of the analysis.

A check on the linear independence of the mode shapes was carried out using the modal assurance criteria and is shown in Table 5.1.

Table 5.1: Auto MAC for cage EMA

Modal Assurance Criteria (%)								
Mode no		1	2	3	4	5	6	7
Freq (Hz)		11.58	19.51	21.27	23.16	27.53	28.46	32.89
1	11.58	100.0	0.1	17.4	5.6	0.5	0.6	0.4
2	19.51	0.1	100.0	58.1	77.2	56.6	45.7	19.6
3	21.27	17.4	58.1	100.0	91.2	33.4	24.2	6.9
4	23.16	5.6	77.2	91.2	100.0	45.4	34.9	11.1
5	27.53	0.5	56.6	33.4	45.4	100.0	72.9	79.9
6	28.46	0.6	45.7	24.2	34.9	72.9	100.0	57.9
7	32.89	0.4	19.6	6.9	11.1	79.9	57.9	100.0

The high off-diagonal values indicate that some of the modes are not linearly independent. This is the effect of *spatial truncation* — there are clearly not enough degrees of freedom to differentiate between the motion of some of the modes. Modes 2,3 and 4 show high correlation with one another, as do modes 5,6 and 7. In order to distinguish the differences between these modes, it is necessary to measure transfer functions at more points. It is likely that the vibration of the screens covering the sides and back of the cage are responsible for some of the modes. If their resonant frequency was close to that of the main resonance, then the mode shape obtained using the limited degrees of freedom would appear similar to that of the main resonance. A simple means to determine if this was the case would be to measure a few transfer functions at a number of points on one of these screens and compare the resonant frequencies to those obtained for the main test.

5.3 FEM MODELS

Since a cage was not available for testing initially, work began with the development of the FEM model. As only an older version of ABAQUS with very limited pre- and post-processing capabilities was available, almost every node had to be input individually. The geometry of the cage allowed only minimal use of ABAQUS' limited node and element generation capabilities. This proved to be a very tedious task and with virtually non-existent pre- and post-processing capabilities, the numerous errors which occurred were difficult to find and correct. Indeed, many errors were only discovered when the I-DEAS software package became available on a MicroVax II computer. The MODEL SOLUTION FEM code available within I-DEAS was also used in the analysis. A practical approach was emphasized. No attempt was made to model the cage in minute detail — a simple, inexpensive model depicting the major characteristics of the real cage was desired. It soon became obvious that without any experimental data with which to compare results of the analysis, little confidence could be placed in their accuracy. Areas requiring attention could not be identified and the FEM modelling came to a halt. Once the results of the EMA were known, deficiencies in the models were corrected and a new model developed.

In all models, the beam joints were modelled as simple moment connections, with no special consideration given to detail modelling of joints. The material properties and beam and plate properties that were used in all the models are presented in Appendix E. The following sections describe the various models developed.

5.3.1 First ABAQUS Model

The initial model of the cage was developed using a mainframe version of ABAQUS. This model was transferred to the MiroVax II and the extensive pre- and post-processing capabilities of I-DEAS were used to correct errors and prepare the model for analysis by the MicroVax version of ABAQUS. This model of the cage consisted of two-noded (B31) beam elements and four-noded (S4R) shell elements. Only the major features of the cage were modelled. These included the top and bottom transoms, the bridles, transoms, floor decks, corner angles and the plates forming the top section of the cage. The floor plates, bracing and screens were not modelled. The minimum number of nodes and the lowest order elements needed to define these features were used. This model comprised 496 nodes and 2976 degrees of freedom. Twelve modes were extracted using the subspace iteration method for solving large eigen problems. Six of these were rigid body modes (since the cage was not restrained) and six were flexural modes. Using I-DEAS it was possible to animate the mode shapes — a valuable tool for visualizing the vibration of the cage at natural frequencies. The first shape was the first bending mode — a half sine wave shape in the plane of the guides. The second was the second bending mode — a full sine wave shape in the plane of the guides. The third mode was the first torsional mode — twisting along the axis of the cage. The fourth mode was the third bending mode, once again in the plane of the guides. The fifth and sixth modes showed localized effects — the motion of the massive steel top transoms and the heavy top section of the cage. The natural frequencies of these modes were in the range 7–20 Hz. No out of plane bending modes were apparent. The greater out-of-plane stiffness of the cage would account for this — these modes would occur in a higher frequency range than their in-plane counterparts. The mode shapes for this model are shown in Figures 5.14– 5.16

5.3.2 Second ABAQUS Model

The results of the first ABAQUS FEM model were compared to the EMA results on both a qualitative and quantitative level (more detail on the methods used may be found in section 5.4). It was evident that the FEM model was not stiff enough because its natural frequencies for the bending modes were significantly lower than those indicated by the EMA. Furthermore, the FEM analysis indicated that a torsional-type mode was present, whereas no torsional mode was identified by the EMA. There were two possible explanations for this. Firstly, it could be assumed that the EMA analysis was correct and there was no torsional mode in the frequency range investigated. As it was already established that the FEM model was not stiff enough, stiffening of the model could increase the frequency of this torsional mode, causing it to be shifted to outside the EMA frequency range. On the other hand, it was possible that the EMA analysis had not succeeded in identifying the torsional mode, possibly because the excitation had been applied in such a way that it would tend not to excite a torsional mode. At this point one of the advantages of the dual type approach became evident. Rather than design another test to establish experimentally the presence or absence of the mode, the question could be investigated easily using the analytical model.

To improve on the first ABAQUS model, refinements in three directions were made. Firstly, the model had to be stiffened. In an effort to develop the simplest possible model, the light screens covering the sides and back of the cage were omitted from the first model. They were included in the second model. Secondly, the mesh density was increased to improve definition of the main flexural modes. This entailed increasing the number of elements used to model the bridles and corner angles. Stiffening the model had in fact necessitated increasing the mesh density of these members anyway, because more nodes had to be created in order to attach the screens. Finally, the order of the elements used in the model was increased: three-noded (B32) beam elements and eight-noded (S8R) shell elements were used.

All of these changes were effected using the pre-processing capabilities of I-deas. Ironically, the ease with which the elements could be upgraded lead to the failure of the model. The number of degrees of freedom to be analyzed increased by 286 % (from 2976 to 8500), while the number of elements increased by 186 % (from 365 to 678). This model suffered from two main problems. Firstly, it required very long run times to extract the modes due to the number of degrees of freedom involved. Secondly, numerous modes resulting from local resonances of the screens were detected at frequencies around 8.5 Hz and 10 Hz — two of these mode shapes are shown in Figure 5.17. These numerous unwanted modes made it difficult to locate the main flexural modes and coupled with the long run times required, rendered the model impractical.

Nevertheless, valuable insight into the origin of one of the peaks observed in the FRF's was gained. This peak occurred at a frequency of approximately 8.5 Hz and is clearly visible in Figure 5.8. It is probable that this peak is caused by the resonance of the screens.

5.3.3 MODEL SOLUTION Model

From the results obtained by the above (second ABAQUS) model, it could not be concluded that the addition of the screens had had the desired effect. The third model was derived from the second by retaining the elements defined for the second, but converting them back to two-noded beams and four-noded shell elements. It was anticipated that this would reduce the number degrees of freedom back to a manageable level. This model consisted of 678 two-noded beam and four-noded shell elements using 520 nodes and 3120 degrees of freedom. In this model the screens were modelled because it was believed that the stiffness that they contributed was significant. To reduce the run times and eliminate the problem of extracting numerous modes showing only the flexure of the screens, as had happened in the previous model, a Guyan Reduction technique available in MODEL SOLUTION, was opted for. The maximum allowable number of master degrees of freedom (221) were used in the reduction. These were selected on the following basis:

- degrees of freedom corresponding to those at which the response was measured in the modal tests were retained

- only degrees of freedom in the x-and y-directions were retained as the response in the z-direction for the modes considered was known to be negligible

- degrees of freedom not in the direction of motion of the first few modes (ie. y-direction) were dropped in preference to those in the x-direction.

The first thirteen mode shapes were extracted, the first five being rigid body modes and the remaining six flexural modes. Only five modes were rigid body modes in this case because the elimination of some degrees of freedom, as discussed above, effectively restrained one of the rigid body modes. The mode shapes for this model are shown in Figures 5.18– 5.21. The first flexural mode was again the first bending mode, in the plane of the guides. The second mode shows the effect of the heavy top section of the cage coupled with the low stiffness associated with the door opening. The third mode is the second bending mode in the plane of the guides. The fourth mode shows local effects resulting from the out-of-phase motion of the massive top transoms. The fifth mode shows in-phase motion of the top transoms as well as flexure of the middle section of the cage. The sixth mode also shows localized effects — motion of the top transoms again and flexure of the screens on the first deck of the cage. The seventh mode is clearly the third bending mode of the cage, in the plane of the guides. Some local effects caused by the top transoms are again present. The last mode extracted shows only local effects of the flexure of plates and screens at the top of the cage. In this mode, the displacement of the screens (included as slave degrees of freedom) can be clearly seen to merely follow the displacement of the bridle and plates at the top of the cage (included as master degrees of freedom).

The results from this model showed that the screens had had the desired effect and the natural frequencies were increased to values more in line with those obtained from the EMA. The correlation of the FEM and EMA results will now be discussed.

5.4 CORRELATION BETWEEN FEM AND EMA: MAC

Ewins [6] states that generally, a value for the MAC in excess of 90 % should be attained for correlated modes and a value of less than 5 % for uncorrelated modes. However, other researchers [22] have set goals as low as 60 % for correlation between FEM and EMA studies.

Correlation between the first ABAQUS model and the modal model is presented in Table 5.2. Entries showing high correlation are indicated in **bold** face. The natural frequencies predicted by the FEM model are between 36 % and 57 % lower than their EMA counterparts. Despite the poor correlation in the natural frequencies, the mode shapes themselves show acceptable levels of correlation, varying between 67.6 % and 80.5 %. EMA modes 2,3 and 4 correlate well with the second bending mode identified by the FEM analysis. This is attributed to the effects of spatial truncation. In order to evaluate the differences between these three modes, more degrees of freedom in the EMA model are required. Exactly which of the three modes is the second bending mode is difficult to establish, though the correlation to the FEM second bending mode would indicate that it is EMA mode 4 at a frequency of 23.16 Hz.

Table 5.2: Cross-MAC: ABAQUS model (rows) vs EMA

Modal Assurance Criteria (%)								
Mode no		1	2	3	4	5	6	7
Freq (Hz)		11.58	19.51	21.27	23.16	27.53	28.46	32.89
7	7.36	**78.6**	0.6	10.6	2.2	0.2	2.5	0.1
8	10.69	0.1	**73.8**	**67.6**	**80.5**	40.4	34.8	10.1
9	11.05	7.9	1.3	7.1	6.0	7.6	6.0	3.5
10	14.04	0.0	3.4	1.3	0.1	41.2	25.8	**72.1**
11	19.21	6.4	0.1	0.1	0.0	0.3	0.2	0.1

Table 5.3 shows correlation between the MODEL SOLUTION model and EMA. Entries showing high correlation are indicated in **bold face**. The correlation between natural frequencies in this model are much better. The FEM frequencies vary between 3 % and 20 % lower than than their EMA counterparts. Once again, the correlation in mode shapes is good, ranging from 66.6 % to 83.0 %. As expected,the second bending mode identified in the FEM analysis still shows high correlation with three EMA modes, reinforcing the theory that this is caused by spatial truncation in the EMA model. An interesting observation is that the correlation between the FEM and EMA first bending mode shape has shown a *decrease*, from 78.6 % in

the ABAQUS model to 69.7 % in the MODEL SOLUTION model, while the natural frequencies are now within 3 % of one another. All of the other mode shapes have shown an increase in correlation. Intuitively, one would expect that as the complexity of a FEM model increases, not only do the number of modes accurately predicted increase, but also the accuracy of the lower modes. Although this trend is followed in simple models, in more complex models it is not always the case. Features of the model which might be insignificant for representation of one mode may be significant for the representation of another mode. A summary of the FEM and EMA results is presented in Table 5.4.

Table 5.3: Cross-MAC: MODEL SOLUTION model (rows) vs EMA

Modal Assurance Criteria (%)								
Mode no		1	2	3	4	5	6	7
Freq (Hz)		11.58	19.51	21.27	23.16	27.53	28.46	32.89
6	11.18	**69.7**	0.0	21.9	7.4	2.6	0.2	3.7
7	13.60	13.7	14.2	2.6	4.5	5.7	6.6	1.8
8	19.61	0.1	**66.6**	**72.7**	**83.0**	45.4	38.2	13.3
9	21.17	0.6	2.2	6.0	3.4	0.3	0.3	1.9
10	24.96	4.1	4.8	0.7	0.2	47.8	36.0	**73.7**

Table 5.4: Summary of experimental and analytical results

Description of Mode Shape	Frequency (Hz)			
	EMA	ABAQUS I	ABAQUS II	MODEL SOL
Bending of Screens	—	—	8.5	—
	—	—	10	—
First Bending	11.58	7.36	N/A	11.18
Second Bending	19.51	—		—
	21.27	—	N/A	—
	23.16	10.69	—	19.61
First Torsion	—	11.05	N/A	—
Twisting of Top	—	—	N/A	21.17
Bending of Bottom	27.53	—	N/A	—
	28.46	—		—
Third Bending	32.89	14.04	N/A	26.40

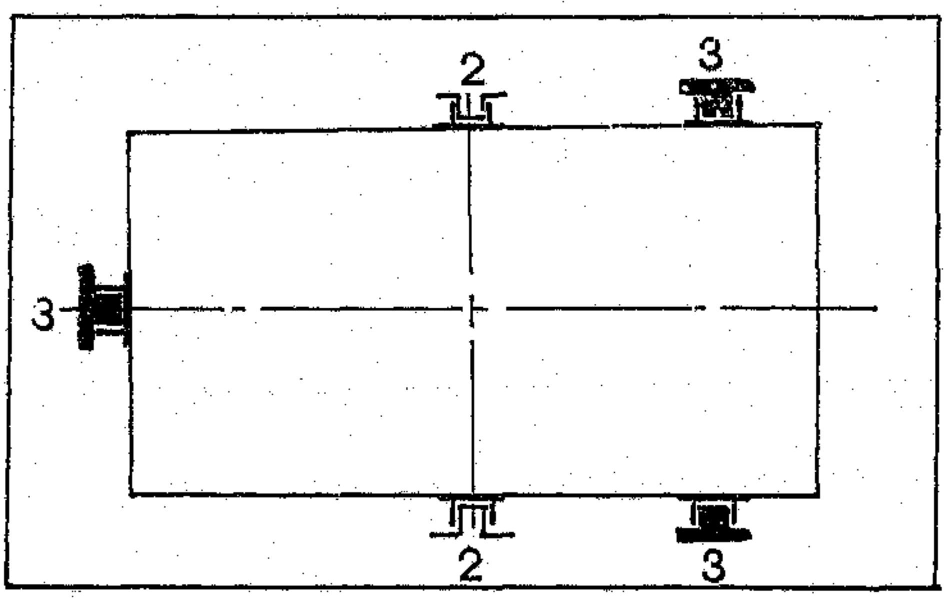

Figure 5.1: Cross-section through cage showing guide configurations

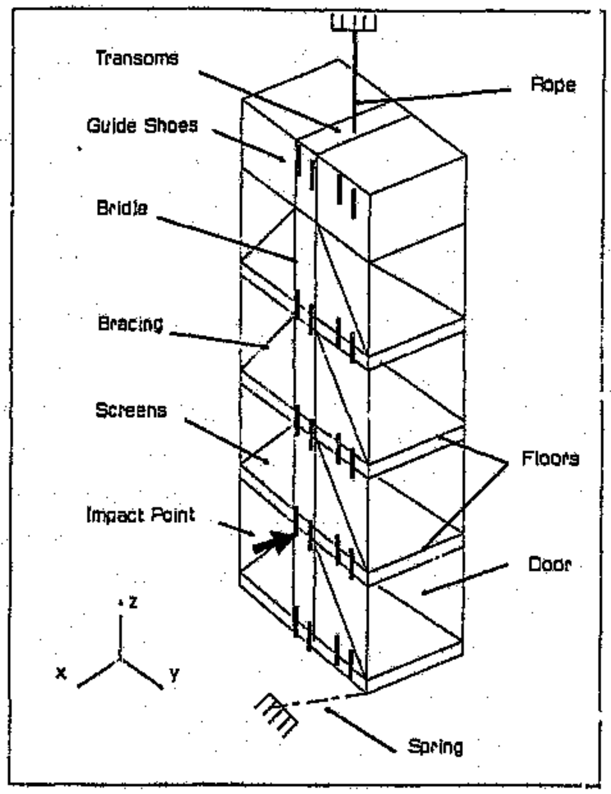

Figure 5.2: Set up of mine cage for impact tests

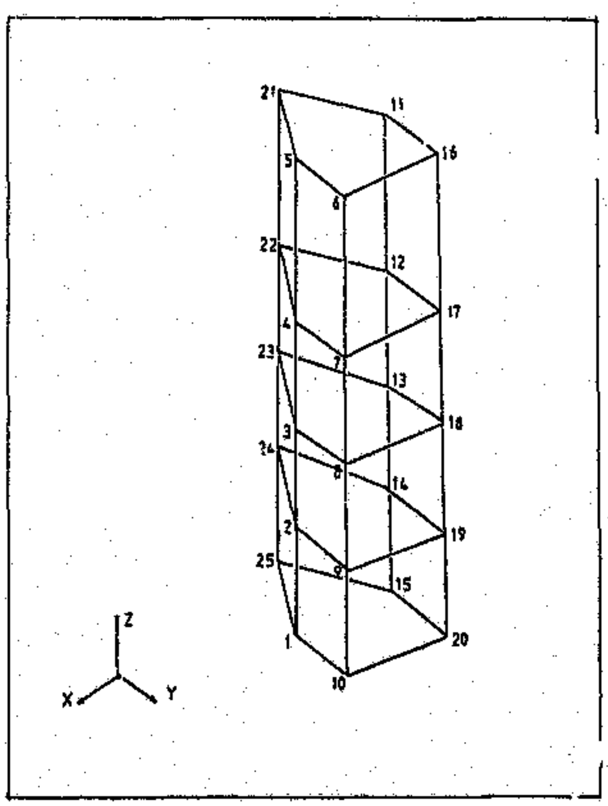

Figure 5.3: Measurement grid for cage modal test

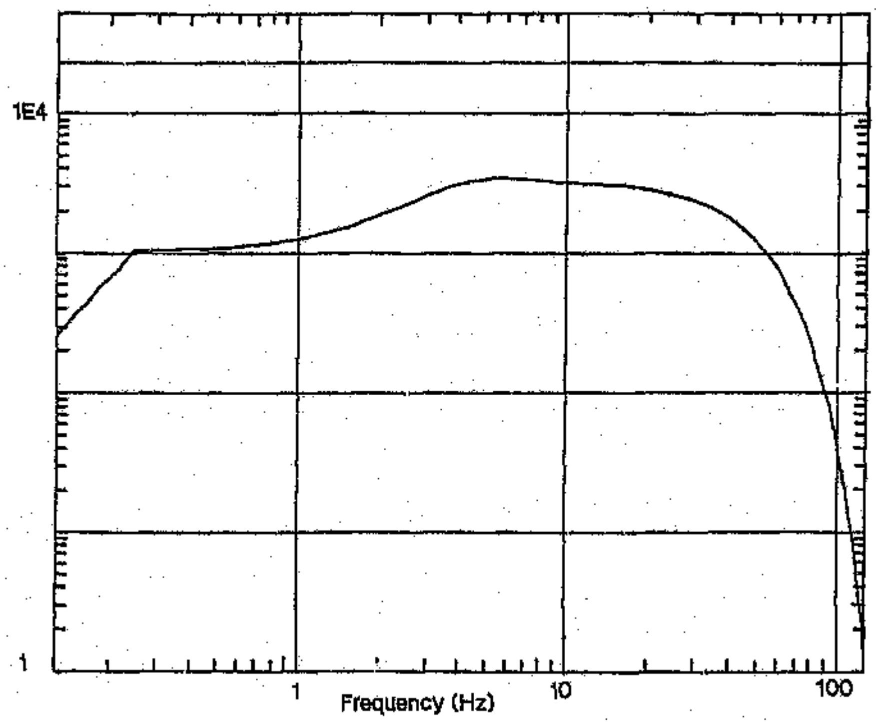

Figure 5.4: Hammer input spectrum

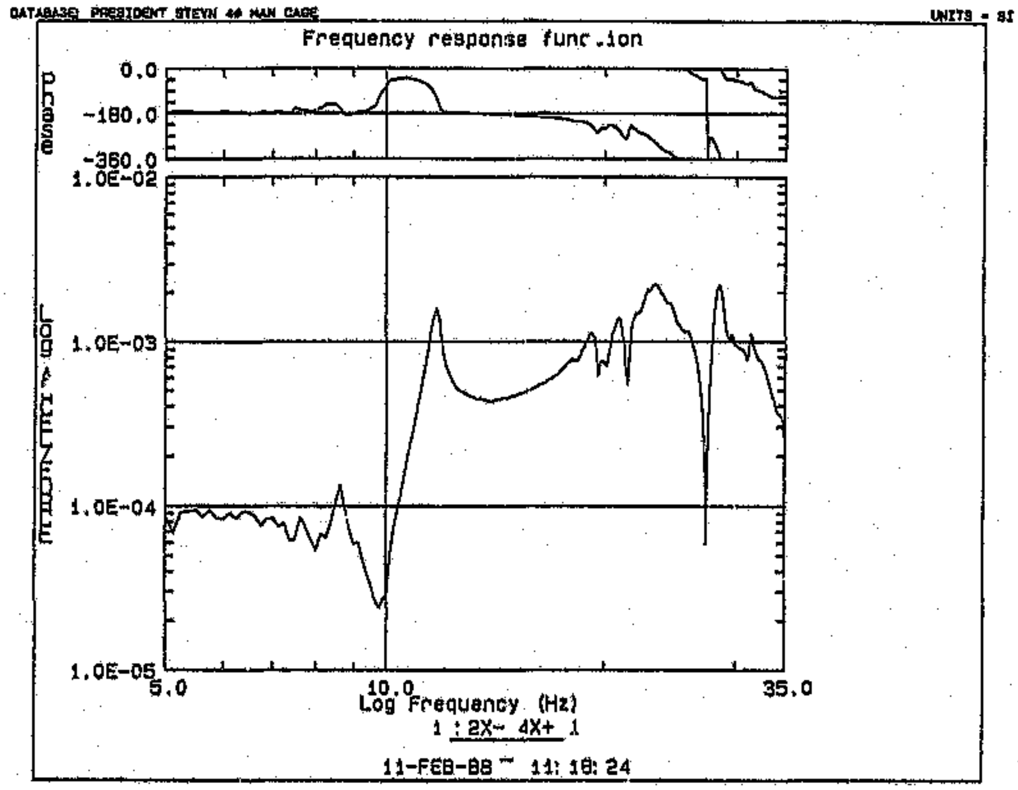

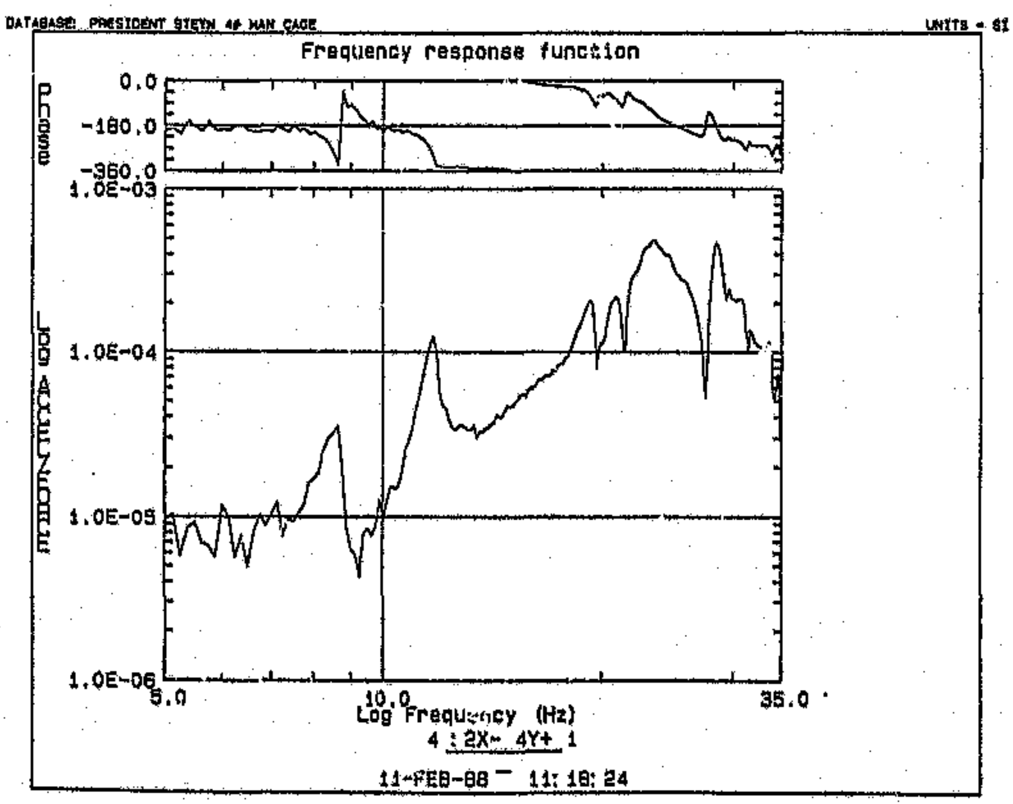

Figure 5.5: FRF's measured in the x- and y-directions

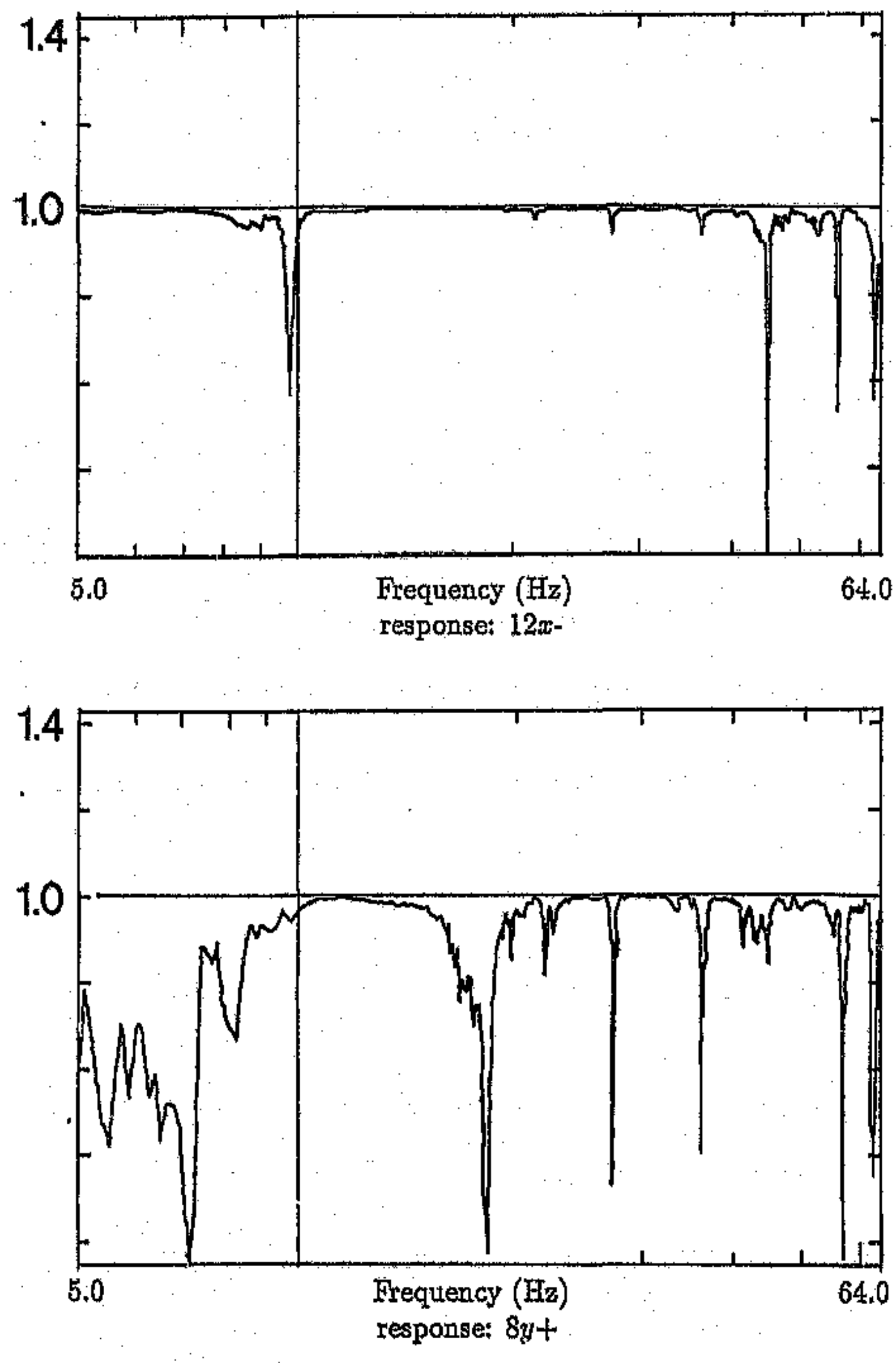

Figure 5.6: Coherence functions for two measurements

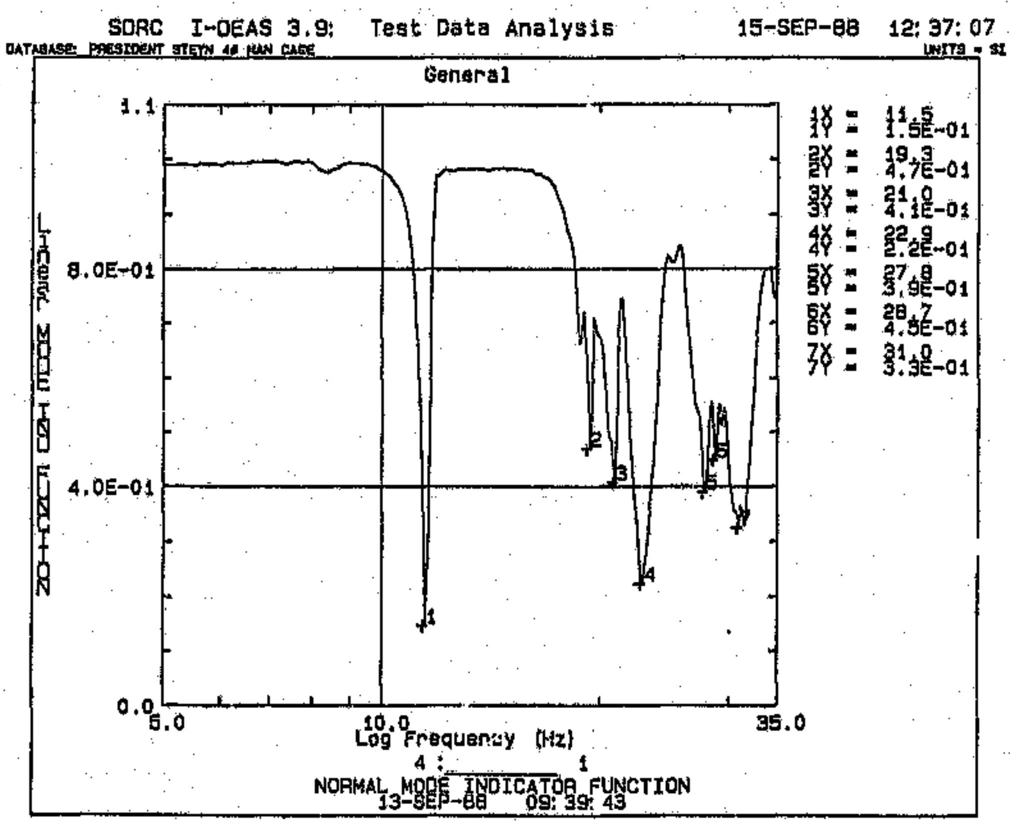

Figure 5.7: Mode indicator function (MIF)

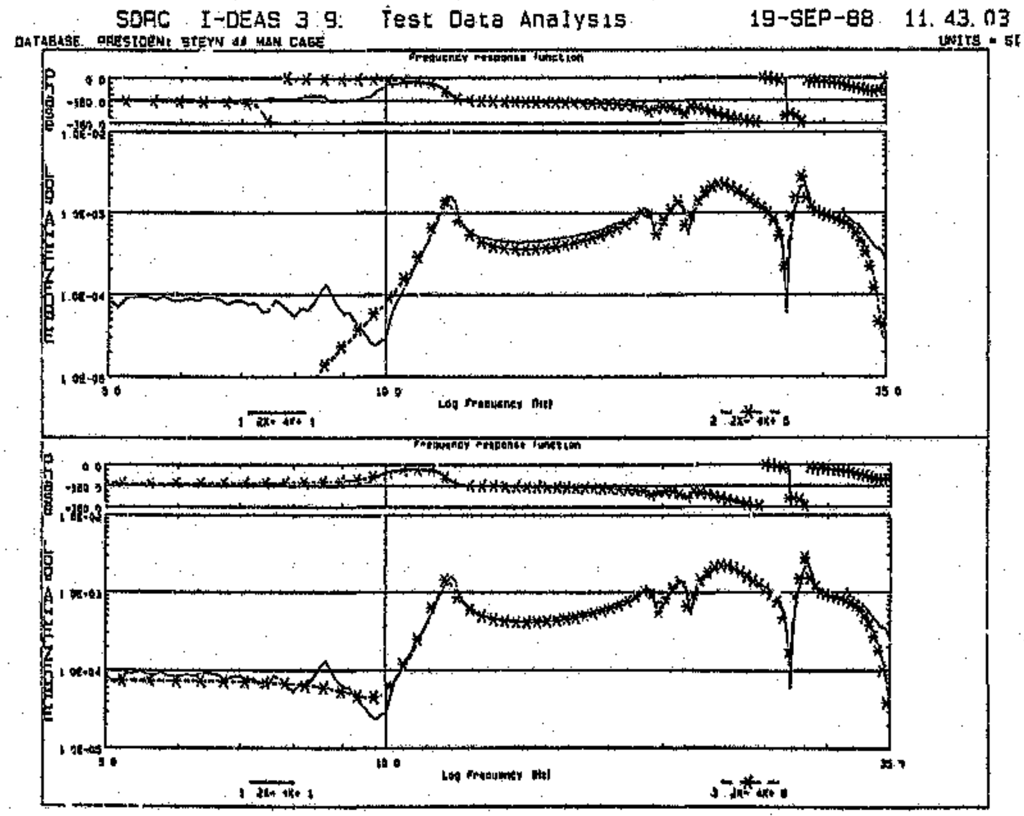

Figure 5.8: Measured and analytic frequency response functions

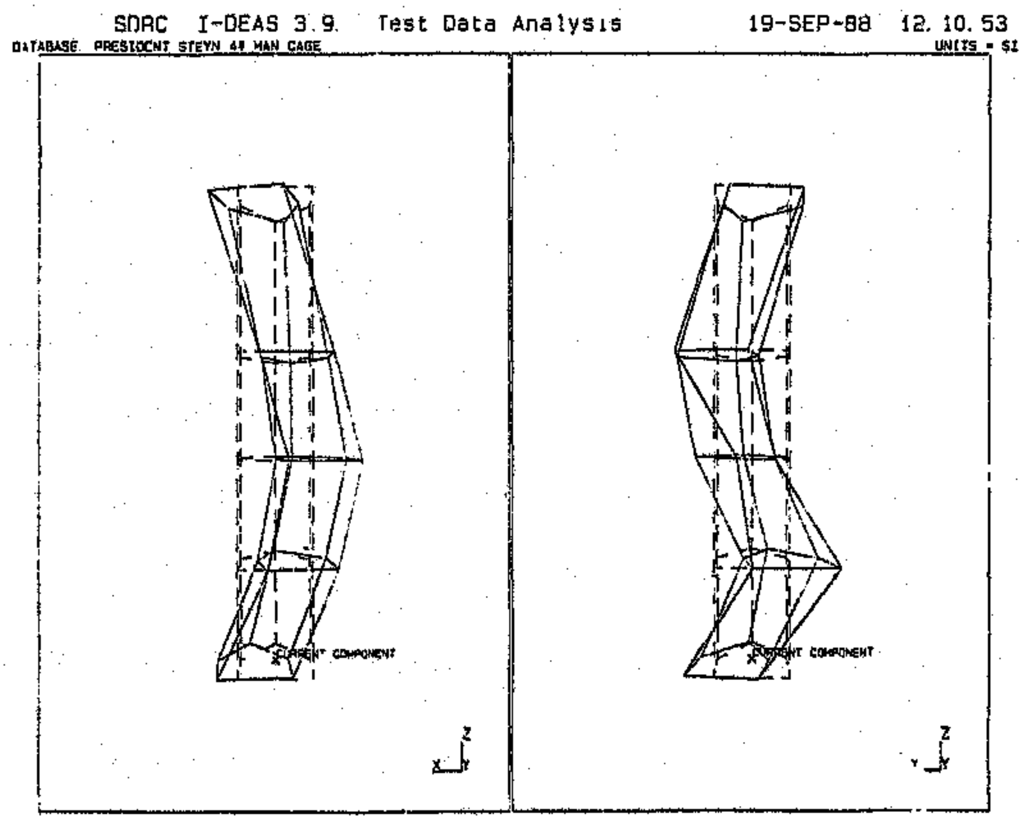

First bending: 11.58 Hz

Second bending: 19.51 Hz

Figure 5.9: EMA: Cage modes 1 and 2

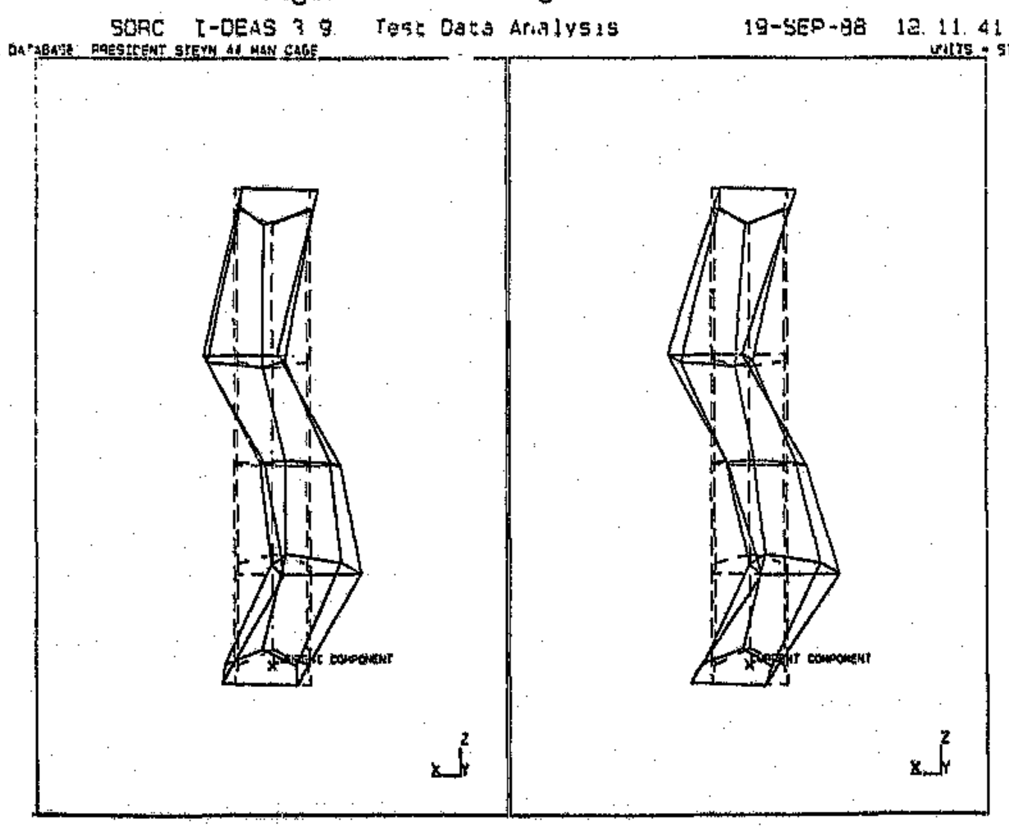

Second bending: 21.27 Hz

Second bending: 23.16 Hz

Figure 5.10: EMA: Cage modes 3 and 4

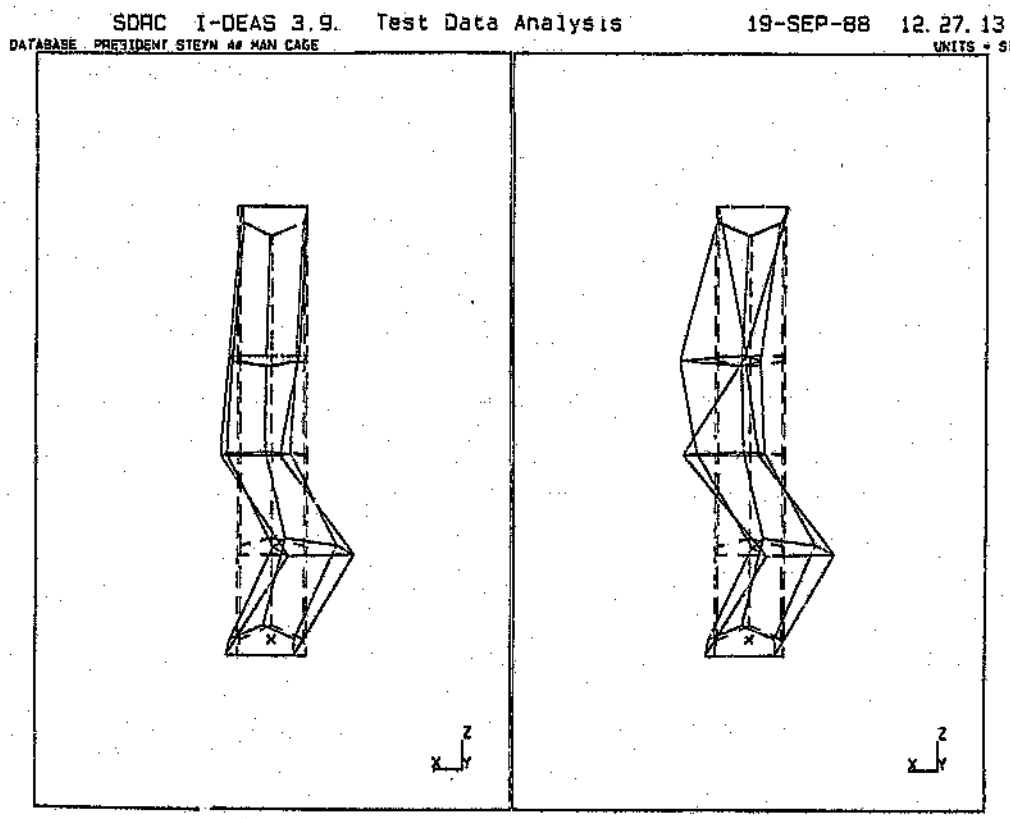

Bending of bottom: 27.53 Hz   Bending of bottom: 28.46 Hz

Figure 5.11: EMA: Cage modes 5 and 6

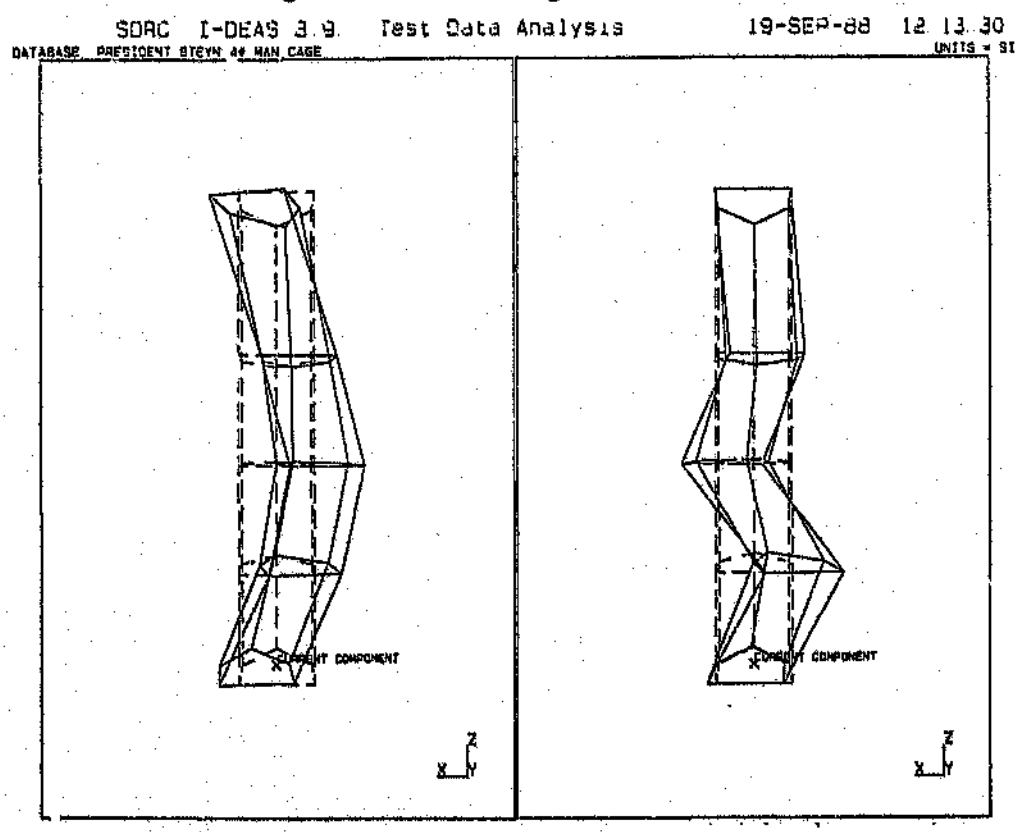

First bending: 11.58 Hz   Third bending: 23.16 Hz

Figure 5.12: EMA: Cage modes 1 and 7

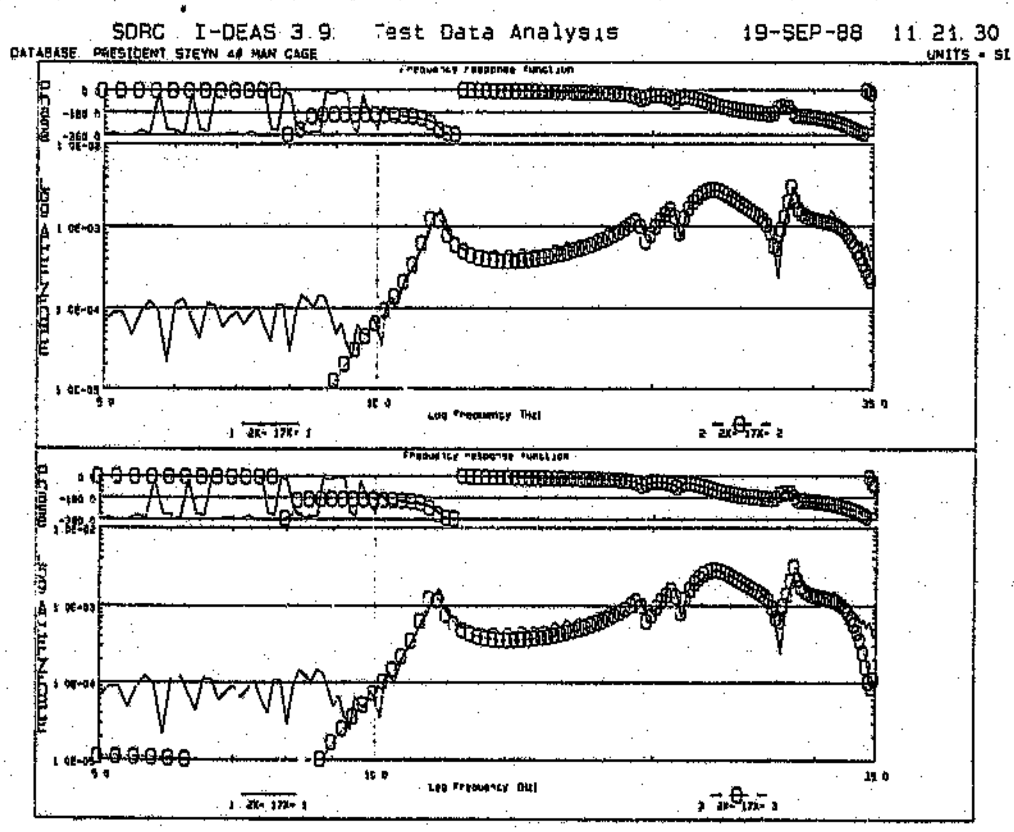

Figure 5.13: Measured and synthesized frequency response functions

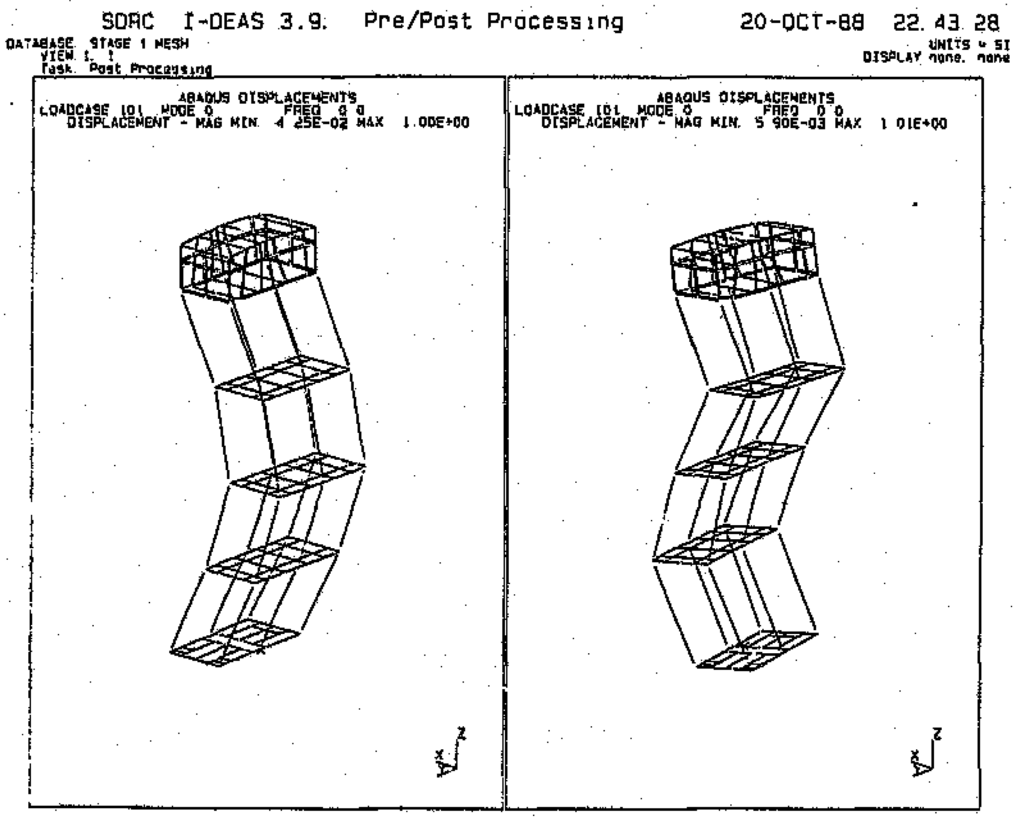

First bending: 7.36 Hz

Second bending: 10.69 Hz

Figure 5.14: ABAQUS: Cage modes 7 and 8

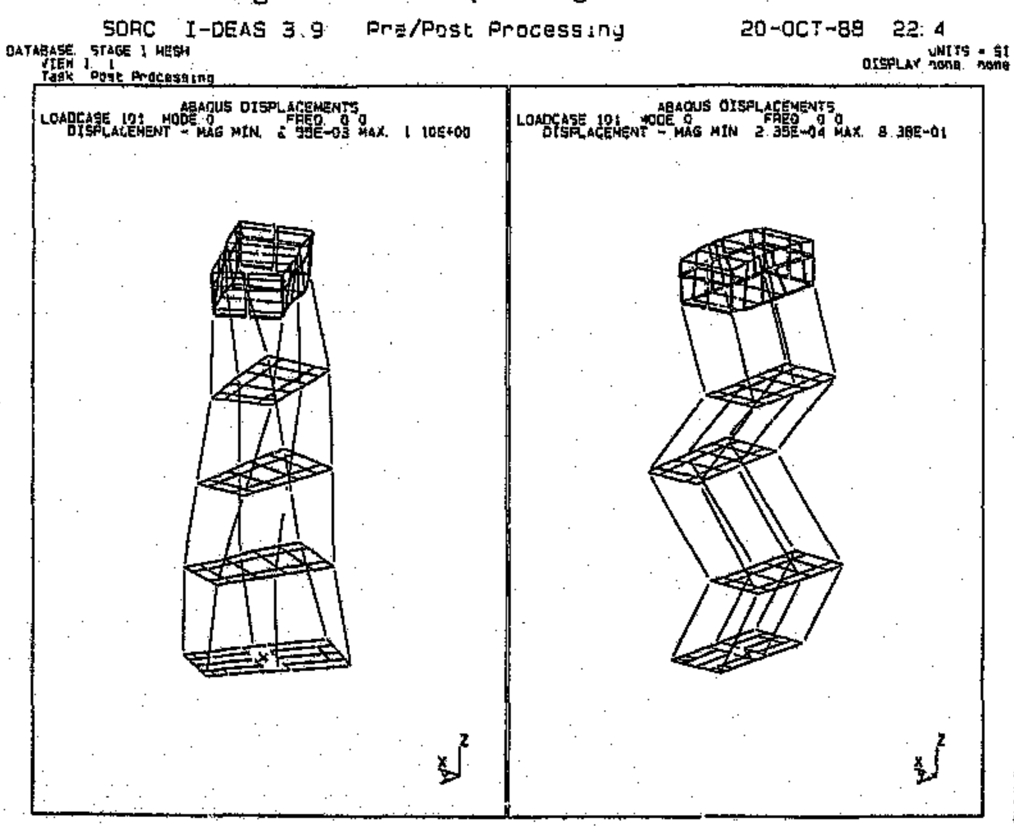

First torsion: 11.05 Hz

Third bending: 14.04 Hz

Figure 5.15: ABAQUS: Cage modes 9 and 10

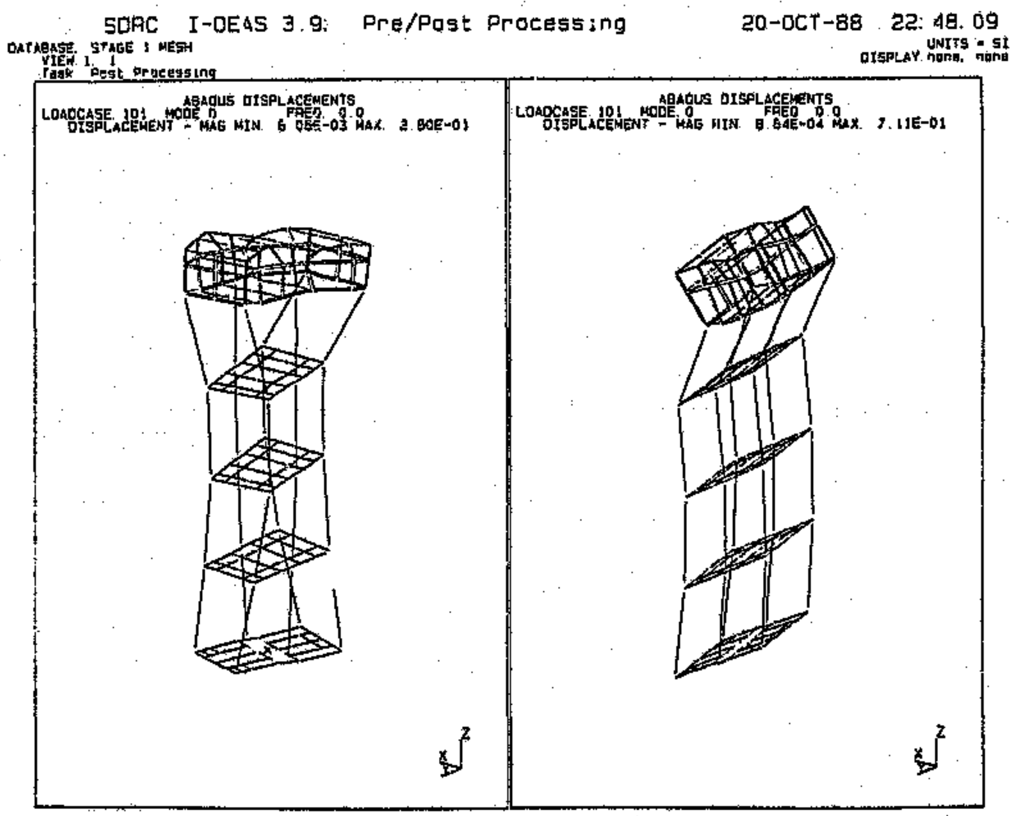

Motion of top transoms: 19.21 Hz Motion of top section

Figure 5.16: ABAQUS: Cage modes 11 and 12

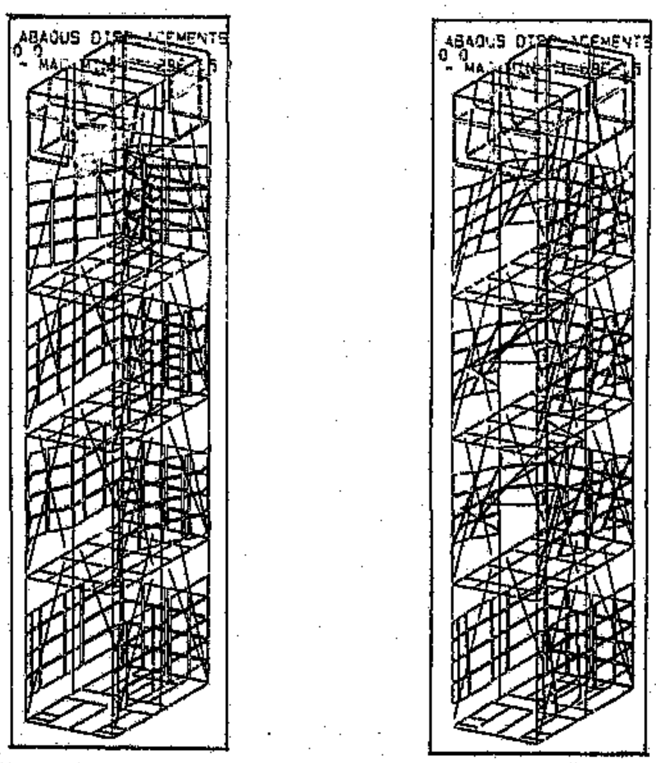

Bending of screens: 8.5 Hz Bending of screens: 10.0 Hz

Figure 5.17: ABAQUS: Cage screen modes

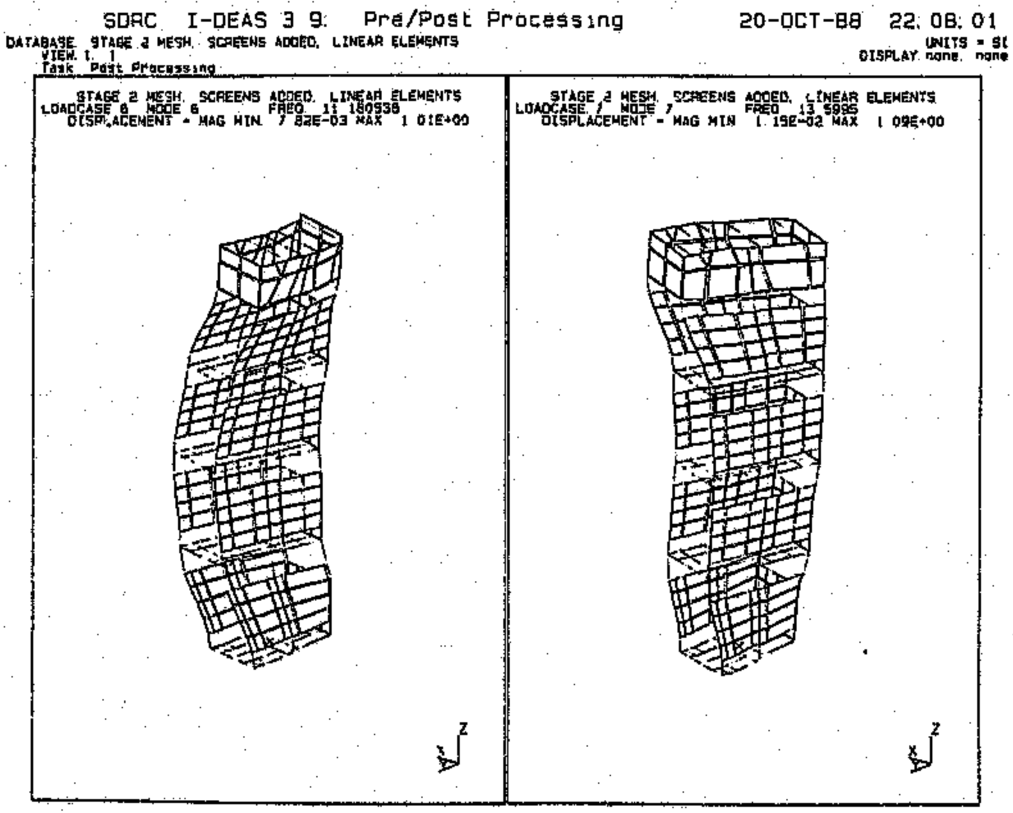

First bending: 11.18 Hz Twisting of top section: 13.60 Hz

Figure 5.18: MODEL SOLUTION: Cage modes 6 and 7

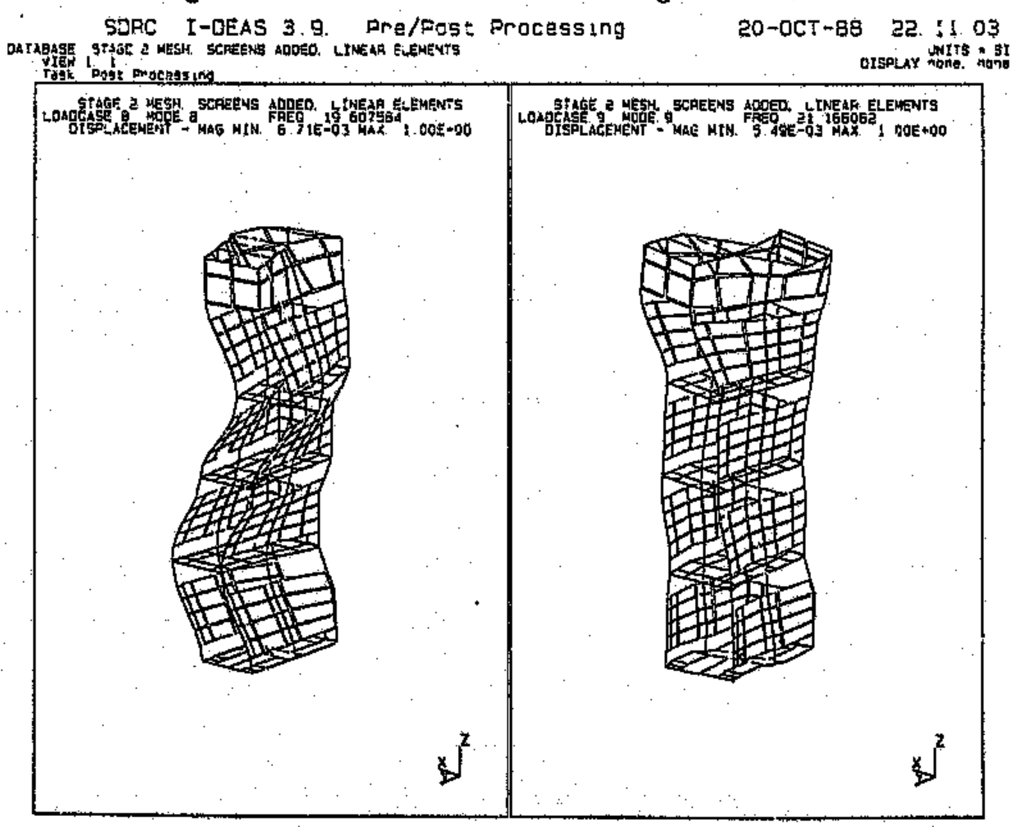

Second bending: 19.61 Hz Motion of top transoms: 21.16 Hz

Figure 5.19: MODEL SOLUTION: Cage modes 8 and 9

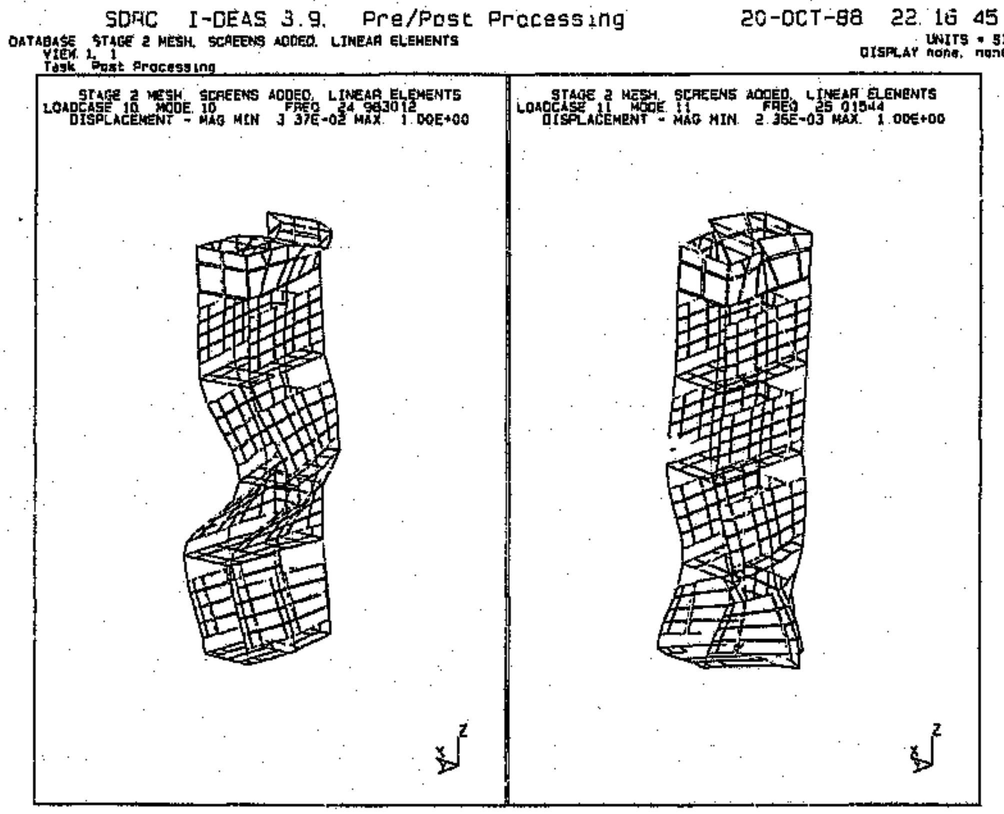

Bending of mid section: 24.96 Hz   Motion of top transoms: 25.01 Hz

Figure 5.20: MODEL SOLUTION: Cage modes 10 and 11

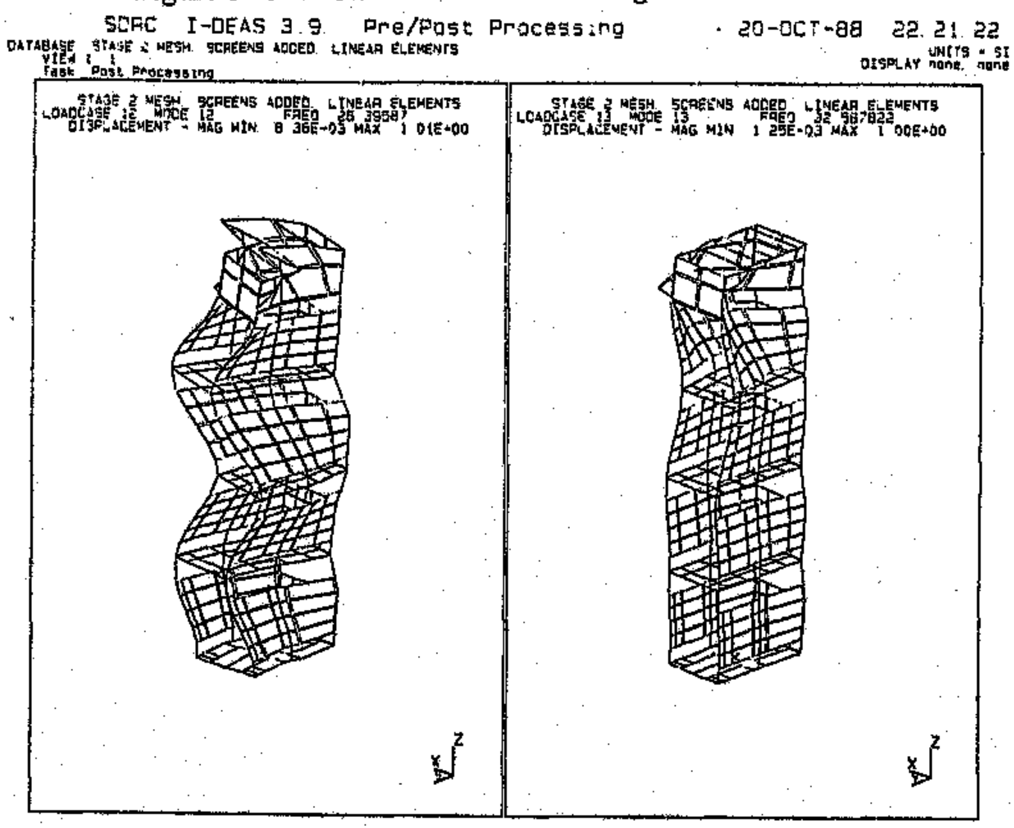

Third bending: 26.39 Hz   Bending of top plates: 32.57 Hz

Figure 5.21: MODEL SOLUTION: Cage modes 12 and 13

Chapter 6

DISCUSSION

Widespread structural problems in the mining industry, both overseas and locally, have lead to extensive investigations into the dynamic behaviour of shaft steelwork and conveyance systems. In South Africa, work has been concentrated on the behaviour of skips operating in gold mines. Little work has been carried out in the area of mine cages, probably because the problems encountered have been of a less serious nature. With increasing production needs, the size and hoisting speed of both skips and cages must increase. While these aspects may be considered from the early stages of the design of new shafts, the effects of increased hoisting speed in existing shafts must be evaluated before speeds may be increased. The phenomenon of slamming, investigated by COMRO and SDRC, becomes more severe as the mass and speed of the conveyance increase. Slamming can be reduced by reducing the variability of the guide stiffness and by introducing flexibility into the conveyance. This is is also shown to be the case by Schmidt and Tondl, who also show the existence of parametric resonances, which, if encountered, can lead to catastrophic failure of the steelwork. The President Steyn 4 shaft skip and cage both operate well below parametric resonance and it should be possible to increase the hoisting speed of both these conveyances without encountering a parametric resonance, although the forces induced by slamming will probably be the limiting factor.

One of the aims of this work was to investigate the dynamic characteristics of a mine cage in order to increase the understanding of the behaviour of cages. This was to be achieved by determining the natural frequencies and mode shapes of the cage via a dual FEM and EMA approach. In order to gain familiarity with the equipment and techniques used in a dual FEM-EMA approach, a simple structure, in the form of a flat steel plate, was selected for analysis. Some theoretical frequencies of this structure could be calculated from results in the literature to assess the accuracy of both the FEM and EMA results. The impact testing method with a GenRad 2515 CAT system was used for the EMA and the FEM models were analyzed using a main frame version of ABAQUS. Apart from developing the necessary skills for a dual FEM-EMA analysis, the exercise served as a baseline test, demonstrating the levels of accuracy that could be attained for the analysis of a simple structure. The exercise showed that while very good correlation between the mode shapes of the FEM and EMA models could be obtained easily, good correlation between frequencies was more difficult to achieve. For the simplest model of the plate and MAC correlation greater than 90 %, the FEM frequencies were 8–68 % lower than those predicted by the EMA. For the most complex model and MAC correlation greater than 90 %, the FEM frequencies were 9–17% higher than those predicted by the EMA. Good correlation between mode shapes does not therefore guarantee good correlation between natural frequencies.

The experimental modal analysis of the mine cage employed the technique of impact excitation. Of the numerous methods available, this technique required the simplest (and cheapest) equipment, least effort in setting up the equipment and preparing the structure and produced results in the shortest time. The entire process of preparing and testing the structure took less than two days. The test data was recorded on an FM tape recorder and processed to produce a set of Frequency Response Functions using a GenRad 2515 Computer Aided Test System. The database of FRF's was passed to a MicroVax II computer where I-Deas modal analysis software was used to carry out the curve fitting and mode shape extraction phases of the analysis.

Generally, the impact excitation is unsuitable for use in large structures since high impact forces are required to inject sufficient energy into the structure, without damaging the structure. However, in the case of the mine cage, the point of impact, namely a guide shoe, allowed the high forces necessary to be achieved without damaging the structure. The rubber tip used allowed responses up to a frequency of 40 Hz to be excited. The quality of data acquired by the impact excitation method is not of the same standard that may be achieved by other methods. However, as the ultimate aim of the experimental analysis was the validation of a FEM model, the speed and ease with which reasonably reliable data could be obtained was considered of greater importance. The possibility of carrying out a more sophisticated test was not ruled out, but the availability of the necessary equipment, the cage itself and time constraints eventually made this option unattractive. The fact that a successful analysis was carried out on a large structure, using a "home-made" hammer and transducer illustrates that sophisticated equipment and techniques are not always necessary. The experimental modal analysis indicated that there were seven modes in the frequency range up to 35 Hz. However, some of the mode shapes appeared to be very similar, indicating a deficiency in the model. More measurement points are required to allow differentiation between such mode shapes. Some peaks in the FRF's were not very sharp, indicating high damping or high modal density in that region. Local resonances of the screens could not be evaluated because no measurements on the screens were taken. These resonances could account for the high modal density suspected in some areas of the FRF plots. They could also explain why several mode shapes appeared to have the same shape. While the model was less than perfect, it did describe adequately the major flexural modes and thus would be useful for comparison with FEM models.

FEM modelling of the cage was done with the ABAQUS code as well as the MODEL SOLUTION code available within I-Deas, all on the MicroVax II. The first FEM model of the structure employed the smallest possible number of linear beam and shell elements possible to define the network of beams and plates making up the cage. The ABAQUS FEM code was used. The screens covering the sides and back of the cage, plates covering the floors of the cage and the roller shutter doors were not modelled. The first finite element model of the cage was not a satisfactory one and clearly indicates that a significant amount of skill and experience are required for successful modelling of real structures. The first flexural mode had a frequency of 7.36 Hz, compared with the 11.58 Hz measured in the EMA. The omission of the screens covering the sides of the cage was a result of the lack of experience of the modeller. The screens had a significant stiffening effect on the structure and affected the natural frequencies of the flexural modes of vibration. Development of the FEM model from a position of very little experience highlighted the need for some means of validating the FEM model.

The experimental modal analysis allowed the FEM model to be developed and tuned to produce results in line with those actually measured. With the aid of modern pre-processing software, the FEM model was easily upgraded and modified. A second ABAQUS model included the screens and a denser mesh to allow a better spatial description of the main modes. The floors and roller shutter doors were not modelled as their contribution to the bending and torsional stiffness of the model was considered to be small. Quadratic rather than linear elements were used. However it was found that the size of the model, as represented by the number of degrees of freedom, exceeded the practical capabilities of the hardware. Eigenvalue extraction is a computationally expensive process and by increasing the size of the model to over 8 000 degrees of freedom, excessively long run-times were required to extract the eigen solution. Numerous modes depicting the vibration of the screens were extracted, rather than the more important main structural modes. In particular, modes of vibration of the screens at 8.5 Hz and 10 Hz were found. These problems were overcome by reverting to linear elements and using the technique proposed by Guyan to reduce the size of the mass and stiffness matrices. The MODEL SOLUTION FEM code, with the facility for implementing the Guyan reduction was used on the third model. The mass matrix was condensed to one having only 221 degrees of freedom, significantly reducing the required computing effort. Appropriate selection of the 221 degrees of freedom in the reduced model ensured that the main structural modes would be represented while the costly extraction of numerous modes depicting the local vibration of the screens was avoided.

Mode shapes from the FEM and EMA studies were passed from the MicroVax to a personal computer for comparison by means of the Modal Assurance Criteria, using a program written in PASCAL. The MAC provided a quantitative means of comparing mode shapes from the EMA and FEM studies. While MAC correlations in excess of 90 % were obtained for the plate analysis, correlation for the cage analysis varied between 69 % and 83 %. FEM natural frequencies differed from EMA frequencies by 3–20 % for the cage analysis.

Use of the dual approach led to a better understanding of the structure than would otherwise have been possible. It became clear that the screens contribute significantly to the bending and torsional stiffness of the cage. The occurrence of a small peak on some of the FRF's at about 8.5 Hz could be explained by noting that a mode of vibration of the screens (as determined by the FEM analysis) occurred at approximately that frequency. The EMA failed to identify a torsional mode of vibration of the cage in the frequency rang 0–35 Hz. The EMA alone could not allow a conclusion to be drawn with regard to the presence of a torsional mode: either it did not exist in the frequency range of the analysis, or else it was simply not sufficiently excited to show on the EMA. The FEM analysis proved that there was no such mode in the frequency range of the analysis.

The analysis has shown that the cage exhibits lower natural frequencies than the skip, even in the empty condition, indicating that it is more flexible. Its mass is also much lower than that of the skip, hence slamming effects will be less severe. The lowest flexural natural frequency of the cage (11.58 Hz) is far higher than the bunton passing frequency of 2.5 Hz, hence flexural resonance should not be encountered. In addition, the cage appears to operate further from parametric resonance than the skip, so an increase in hoisting speed can be more safely accommodated with the cage. The analysis of Schmidt and Tondl assumes that the conveyance behaves as a rigid body. While the work of COMRO and SDRC has shown that this is a reasonable assumption for the President Steyn skip, it is not necessarily the case for all conveyances. Further research should investigate the effects of flexible conveyances on the position of the parametric resonance.

Chapter 7

CONCLUSIONS

1. The impact method of modal testing can provide a very quick and simple method for estimating the natural modes of vibration of large structures.

2. The finite element method used for the extraction of eigenvalues from problems with many degrees of freedom requires considerable skill. The capabilities of the computer hardware can be exceeded easily by attempting to model the structure too finely.

3. EMA provides an important means of validating a dynamic FEM model of a complex structure.

4. Using a dual FEM-EMA approach, the analyst can gain a greater understanding of the dynamics of the structure than would be possible using either of the two techniques in isolation from one another.

5. Seven natural modes of vibration of the President Steyn 4 shaft mine cage were identified in the 0–35 Hz range. These included the first, second and third bending modes, in the plane of the guides.

6. The lowest of the cage flexural frequencies (11.58 Hz) is too far from the bunton passing frequency (2.50 Hz) for resonance to be encountered.

7. The screens on a cage contribute significantly to its bending and torsional stiffness.

8. The President Steyn 4 shaft cage is more flexible and lighter than the skip, hence slamming effects will be less pronounced. The cage operates further from parametric resonance than the skip. Hence an increase in hoisting speed can be more safely accommodated with the cage than with the skip.

Chapter 8

RECOMMENDATIONS

1. A more sophisticated EMA should be carried out on the cage to investigate in detail the reason for several modes having the same shape. Such testing should include more measurement points on the bridles as well as some measurement points on the screens. An electromagnetic shaker should be used and positioned in such a way as to excite flexural and torsional modes.

2. Further FEM modelling to evaluate the effects of the cage payload should be undertaken. Other improvements in the model could include the plates covering the floors and the roller shutter doors. These features can probably be modelled as point masses as it is unlikely that they affect the stiffness of the cage in bending.

3. The effect of conveyance flexibility should be incorporated into the model of Schmidt and Tondl to investigate its influence on the position of parametric resonance.

Bibliography

[1] Greenway ME. *Future Trends in the Design of Shaft Steelwork and Conveyances*. Anglo American Corporation of South Africa Report.

[2] Krige GJ, Kemp AR. The behaviour and design of mineshaft steelwork and conveyances: a summary of a current research programme. *The South African Mechanical Engineer*, Vol 32, July 1982, pp 163–169.

[3] Krige GJ, Kemp AR, Alport B, Fotopoulos M. The behaviour and design of mineshaft steelwork and conveyances. *The Structural Engineer*, Vol 63B No 3, September 1985, pp 41–49.

[4] SDRC[1] Final Report No 11964. *Shaft Steelwork Design Guidelines*. Submitted to the Chamber of Mines, January 1987.

[5] SDRC Final Report No 12207. *An Investigation into the Slamming Behaviour of Flexible Skips* Submitted to the Chamber of Mines, May 1985.

[6] Ewins DJ. *Modal Testing: Theory and Practice*. Research Studies Press, Hertfordshire, 1985.

[7] Lang GF. *Modal Testing Principles*. Solartron Instruments, Hampshire, Technical Report Number 023/87.

[8] I-Deas Level 4, User guide. SDRC, Ohio, 1988.

[9] ABAQUS Version 4.5, Theory manual. Hibbitt, Karlson and Sorenson, Inc., Providence, 1984.

[10] Tse FS, Morse IE, Hinkle RT. *Mechanical Vibrations*. Allyn and Bacon Inc., Massachusetts, 1980.

[11] Schmidt G, Tondl A. *Non-Linear Vibrations*. Cambridge University Press, Cambridge, 1986.

[1] SDRC is a service mark of Structural Dynamics Research Corporation

[12] Newland DE. *An Introduction to Random Vibrations and Spectral Analysis*. John Wiley and Sons, Second Edition, New York, 1987.

[13] Bathe KJ. *Finite Element Procedures in Engineering Analysis*. Prentice-Hall, New Jersey, 1982.

[14] Bathe KJ, Wilson EL. *Numerical Methods in Finite Element Analysis*. Prentice-Hall, New Jersey, 1976.

[15] Cook RD. *Concepts and Applications of Finite Element Analysis*. John Wiley and Sons, New York, 1974.

[16] Deblauwe F, Brown DL, Allemang RJ. The polyreference time domain technique. *Proceedings of the Fifth International Modal Analysis Conference*, London, April 1987.

[17] Crowley JR, Thomas Rocklin G, Hunt DL, Vold H. The practical use of the polyreference modal parameter estimation method. *Proceedings of the Third International Modal Analysis Conference*, Florida, January 1985.

[18] Smiley RG, Wei YS, Hogg KD. A simplified frequency domain MDOF curve-fitting process. *Proceedings of the Second International Modal Analysis Conference*, Florida, February 1984.

[19] Ibrahim SR. Modal identification techniques assessment and comparison. *Proceedings of the Third International Modal Analysis Conference*, Florida, January 1985.

[20] Guyan RJ. Reduction of stiffness and mass matrices. *AIAA Journal*, Vol 3 No 2, 1965, pp 380.

[21] Rieger NF. The relationship between finite element analysis and modal analysis. *Sound and Vibration*, Vol 20 No 1, January 1986, pp 16–18,23–31.

[22] Petrick LJ, Benz AD. Case study in the correlation of analytical and experimental analysis. *Sound and Vibration*, Vol 20 No 4, April 1986, pp 24–31.

[23] Stevens KK. Modal analysis — an old procedure with a new look. *Mechanical Engineering*, Vol 107 No 6, December 1985, pp 52–56.

[24] Mitchell LD. A perspective view of modal analysis. *Proceedings of the Sixth International Modal Analysis Conference*, Florida, February 1988.

[25] Ewins DJ. Uses and abuses of modal testing. *Sound and Vibration*, Vol 21 No 1, January 1987, pp 32–37.

[26] Sohaney RC, Nieters JM. Proper use of weighting functions for impact testing. *Proceedings of the Third International Modal Analysis Conference*, Florida, January 1985.

[27] Blevins RD. *Formulas for Natural Frequency and Mode Shape*. Van Nostrand Reinhold Company, New York, 1979.

[28] Morley A. *Strength of Materials*. 11th Edition, Longmans, Green and Co., New York, 1954.

Appendix A

EXPERIMENTAL EQUIPMENT

This chapter describes briefly the equipment used in the modal tests of the mine cage and flat plate.

A.1 GENRAD 2515 COMPUTER AIDED TEST (CAT) SYSTEM

This instrument is a four channel structural and signal analysis machine. It provides 320 alias free frequency lines for 1.25 Hz to 20.48 kHz bandwidths and 400 alias free lines for a 25.6 kHz bandwidth. Software is available for a wide range of applications, from signal analysis to structural and acoustic analysis to rotating machinery vibration analysis. The software used in this project was SDRC's[1] MODAL-PLUS, a package designed specifically for modal analysis and DATM, software to capture FRF's for processing by MODAL-PLUS. All acquisition of FRF's and some of the extraction of modal parameters was carried out using this system. Some of the specifications are shown below:

Manufacturer: GenRad Inc

Model: GR 2515

No Channels: 4 baseband or 2 zoom

Disc Storage: 20 Mb hard disc and 0.5 Mb $5\frac{1}{4}$" floppy disc

[1]SDRC is a service mark of Structural Dynamics Research Corporation

Frequency accuracy: ±0.45 dB

Amplitude accuracy: ±0.01 %

Sensitivity: 8 ranges from 62.5 mV to 8 V

Sampling rate: 65 536 Hz maximum per channel

Anti-Alias Filters: One at 25.6 kHz in cascade with 13 others below 25 kHz

A.2 ACCELEROMETERS

Accelerometers used for both the plate and mine cage tests were of the piezo electric type and were used in conjunction with charge amplifiers. Accelerometer specifications are listed below:

A.2.1 Accelerometers

Manufacturer: PCB Piezotronics International, Inc.

Model: B02 and B10

Type: Piezoelectric

Sensitivity: B02=989 mV/g and B10= 99.7mV/g

Serial No: B02=7317 and B10=7723

A.2.2 Amplifiers

Manufacturer: PCB Piezotronics International, Inc.

Model: 4838A08

Type: Charge amplifier

Serial No: 286

A.3 INSTRUMENTED HAMMERS

The hammer used for exciting the flat plate was a small custom made unit equipped with a PCB force transducer. A nylon tip was found to be suitable. The hammer used for exciting the mine cage was a "home made" unit equipped with a specially built proving ring load cell (see Appendix B). A large rubber tip was used. The specifications of the hammers are listed below.

A.3.1 PCB Hammer Kit

Manufacturer: PCB Piezotronics International, Inc.

Model: GK291B05

Transducer Type: Piezoelectric

Frequency Range: 5 kHz

Force Range: 22 000 N

Resonant Frequency: 28 kHz

Sensitivity: 0.22 mV/N

Mass: 0.45 kg + 0.20 kg extender

Serial No: 831

A.3.2 Large Hammer Kit

The large hammer was used in conjunction with strain gauge amplifier and the two were calibrated as a unit (see Appendix B.

Hammer

Manufacturer: N/A

Transducer Type: Strain gauge

Force Range: 50 kN

Sensitivity: 51 000 N/V

Mass: 72.5 kg + 3ɔ.5 kg extender

Serial No: N/A

A.3.3 Amplifier

Manufacturer: Measurements Group Instruments Division

Model: P-3500

Serial No: 50550

A.4 TAPE RECORDER

A 7 channel FM tape recorder was used to record all transducer signals.

Manufacturer: TEAC

Model: R71

Type: FM cassette recorder

Serial No: 160475

A.5 COMPUTER FACILITIES

The computer facilities used can be divided into four main areas as follows:

1. Main frame computer — ABAQUS finite element code. This facility was used for the modelling of the flat plate and initial modelling of the cage. For the most part version 4-4 was used, but version 4-6 became available later.

2. MicroVax II computer — this computer was equipped with SDRC's Integrated Design Engineering Analysis Software (I-DEAS), and ABAQUS version 4-5. I-DEAS is an extensive software package comprising modules for solid modelling, finite element pre-and post-processing, finite element analysis and analysis of test data. In this study the MODEL SOLUTION linear finite element code and ABAQUS version 4-5 were used to analyze the cage. The pre- and post-processing

module was used to examine the results from both codes. The test data analysis option was used to extract modal parameters and mode shapes from the FRF's captured by the GenRad 2515 CAT system.

3. GenRad 2515 CAT System — this system was equipped with SDRC's MODAL-PLUS modal analysis and DATM data capture software. It was used to capture data from both the tests on the plate and the cage. It was also used to extract the modal parameters and mode shapes from the plate data.

4. Personal computer — a program was written in PASCAL to compare the experimental and analytical results. This program may be found in Appendix F. Results from the mainframe, MicroVax and GenRad were all passed to this computer via various emulation software.

Appendix B

LOADCELL DESIGN FOR A 70 KG HAMMER

B.1 INTRODUCTION

As funds for the purchase of a loadcell were not available, a loadcell had to be designed for the large impact hammer. The hammer was essentially a 150 mm diameter steel shaft with fittings for a rubber tip, extension mass and suspension arm. The loadcell was designed to fit between the tip and the hammer body. The following constraints and criteria were considered to be important:

- Size — the loadcell would have to be small enough to fit between the massive body of the hammer and its light tip without protrusions which could easily be damaged. No dimension could thus exceed 150 mm.
- Ease of construction — the loadcell would have to be constructed from cheap materials using simple machining methods.
- Transduction — strain gauges were to be used as the load detecting elements as they were freely available, as were the required amplifiers.
- Ease of calibration — the transducer should be easy to calibrate and re-calibrate.
- Use of different tips — it should be easy to attach a variety of tips of different stiffness.
- Sensitivity — To ensure that the transducer would have a reasonable output for loads in the design range, the stress induced by the

maximum load at the strain gauge location was set at a minimum of 100 MPa.

- Sensitivity to eccentric loading — sensitivity to eccentric loads should be minimal.
- Linearity — transducer output should be linearly related to load.

B.2 ESTIMATION OF LOADCELL CAPACITY

To estimate the capacity of the required load cell, it was assumed that the hammer of mass M would be allowed to swing pendulum-like from a height h and impact, through a rubber tip of stiffness k, a rigid body with zero rebound velocity. It was expected that these assumptions would result in a conservative design because there would always be a rebound velocity and the body impacted would not be rigid. The magnitude of the impact force is determined by the stiffness of the rubber tip and is given by:

$$F = ke \tag{B.1}$$

The work done on the rubber tip is equal to the change in potential energy of the mass:

$$Mgh = \frac{1}{2}ke^2 \tag{B.2}$$

from which it can be seen that:

$$F = \sqrt{2Mghk} \tag{B.3}$$

The stiffness k of the rubber tip was experimentally estimated by compressing it in an Amsler universal tester. In the range 0-13 KN it was found to be approximately 800 kN/m. For a worst case analysis, the hammer of mass $M = 110$ kg (including a 35 kg extender mass), was allowed to swing from a height of h=1 m. This resulted in an impact force of $F = 41552$ N. The final design capacity for the loadcell was selected as 50 kN.

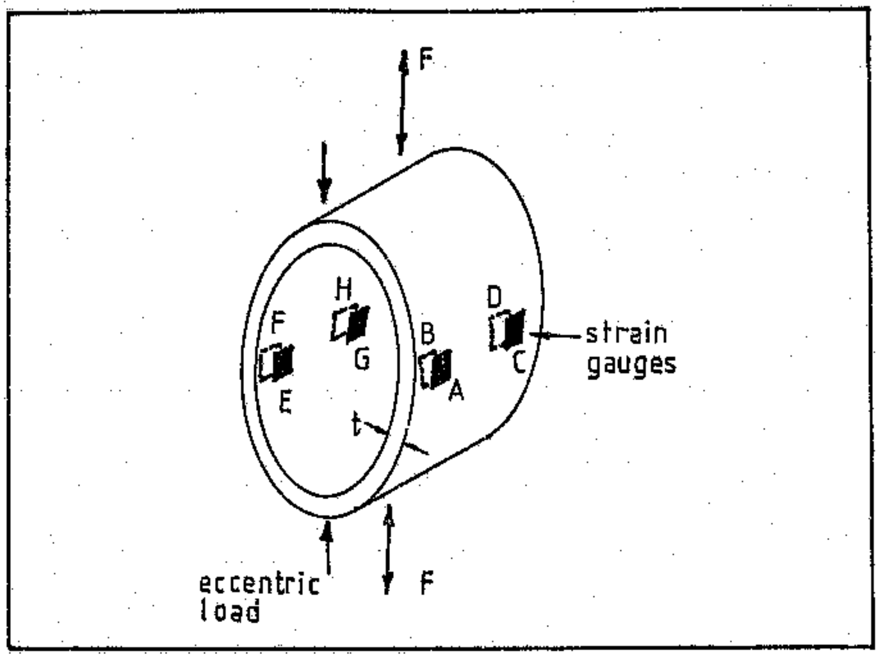

Figure B.1: Proving-ring Loadcell

B.3 TRANSDUCER DESIGN

A proving ring loadcell was chosen because it could satisfy most of the constraints and criteria set out above. It is essentially a short section of cylinder, to which strain sensitive devices may be attached in order to determine the loading on the ring. If situated correctly, and provided the cylinder is "thin-walled", then the strain measured bears a linear relationship to the load applied. It is easy to construct and calibrate and its open construction would facilitate the attachment of different tips. The stress in the proving ring at the locations indicated in Figure B.1 is given by [28]:

$$\sigma = \frac{1.08Fr}{wt^2} \tag{B.4}$$

By choosing a ring of the following dimensions:

inside diameter=100 mm
outside diameter = 130 mm
width (w) = 120 mm

and using a load of 50 kN, the stress at the location of the gauges was $\sigma = 115$ MPa. The dimensional requirements of the transducer were thus satisfied, as were the sensitivity requirements.

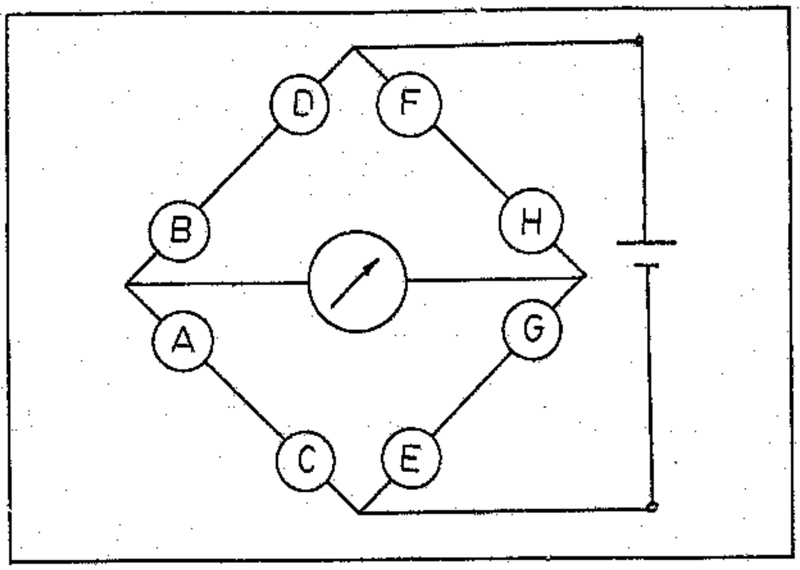

Figure B.2: Wheatstone Bridge circuit

B.4 STRAIN GAUGE WHEATSTONE BRIDGE

Strain gauges were glued to the ring in the locations shown in Figure B.1 and wired into a wheatstone bridge, using two gauges per arm as shown in Figure B.2. The gauges were connected in this way for two reasons:

- the use of two gauges per arm doubles the sensitivity of the wheatstone bridge.
- the gauges are arranged in such a way that the effects of an eccentric loading will be averaged out (see Figures B.1 and B.2).

B.5 CALIBRATION

The loadcell was set up in an Amsler Universal Testing Machine and subjected to a compressive load in the range 0-45 kN. The strain indicator used in the calibration was also used in the actual tests, ie. the loadcell and strain indicator were to be used as a calibrated system. Figure B.3 shows the result of the calibration exercise. It is evident that the loadcell's characteristics are linear as required. The equation relating the load on the transducer to the system output was found to be:

$$F = -0.1118 + 48.7323\, V \tag{B.5}$$

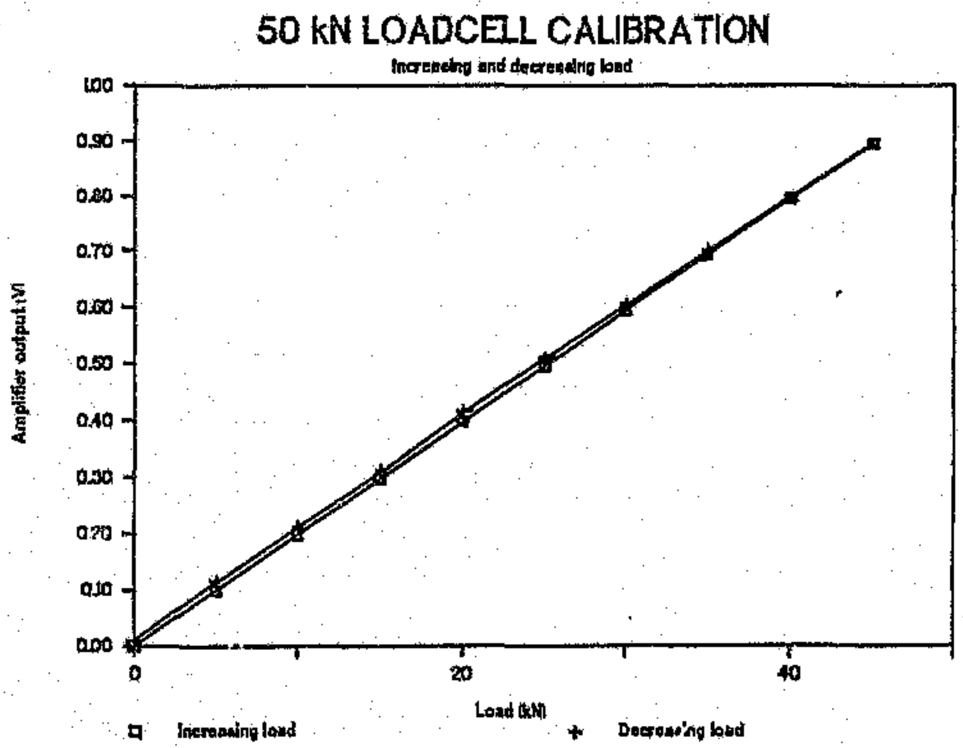

Figure B.3: Calibration of loadcell-strain indicator system

where:
F = load on transducer (kN)
V = system output voltage (V)

Figure B.4 shows the hammer, loadcell and tip assembled as for use. The extender mass is not shown.

Figure B.4: Hammer, loadcell and tip

Appendix C

RESULTS OF PLATE ANALYSIS

The mode shapes and MAC tables obtained for the plate analysis are presented in this Appendix.

C.1 MODE SHAPES

Mode shapes for the first (FEM 1) and fifth (FEM 5) FEM studies are presented along with the mode shapes for the EMA in Figures C.1 – C.32.

C.2 CROSS-MAC BETWEEN FEM AND EMA STUDIES

Cross-MAC tables for the FEM-EMA analysis are presented. Only tables corresponding to the second (FEM 2), third (FEM 3) and fourth (FEM 4) FEM models are shown (Tables C.1 – C.3). The tables for the first and fifth models are presented in Chapter 4.

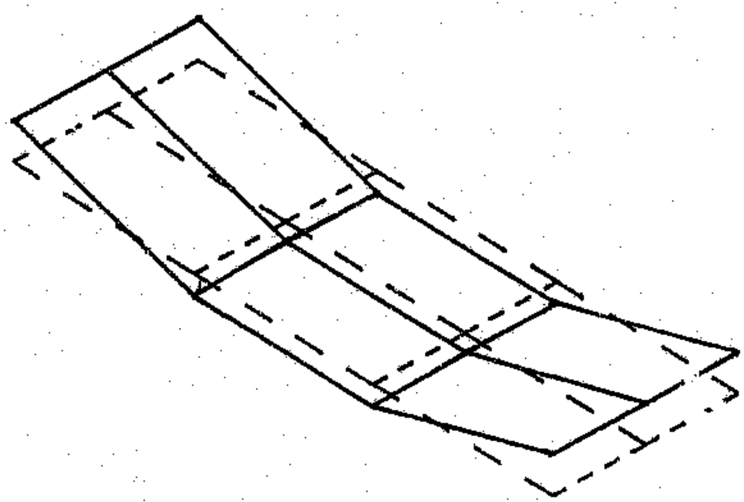

Figure C.1: FEM 1 – plate mode 8: 25.1 Hz

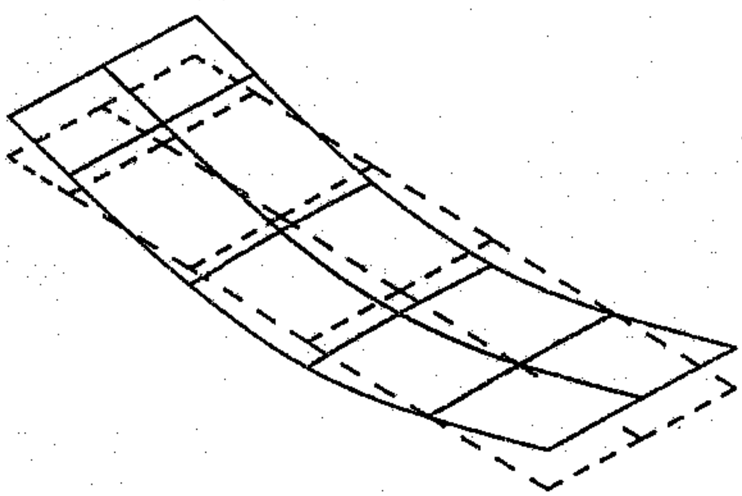

Figure C.2: FEM 5 – plate mode 7: 31.4 Hz

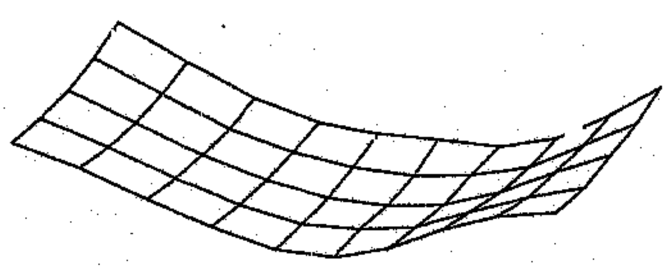

Figure C.3: EMA – plate mode 1: 27.4 Hz

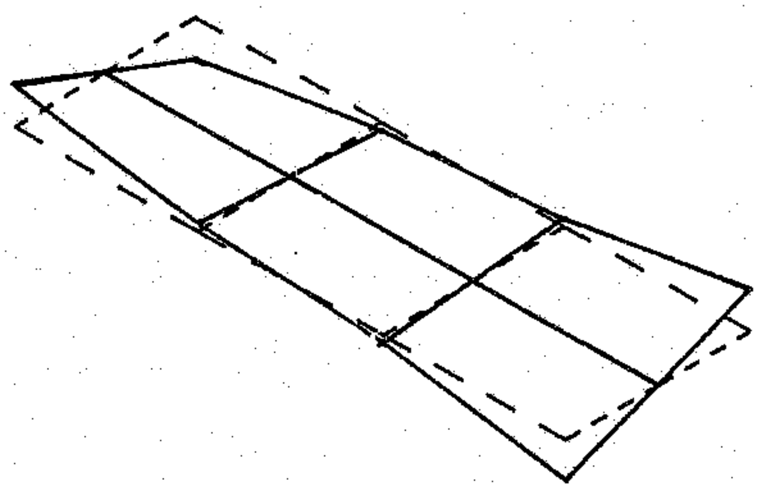

Figure C.4: FEM 1 – plate mode 9: 42.2 Hz

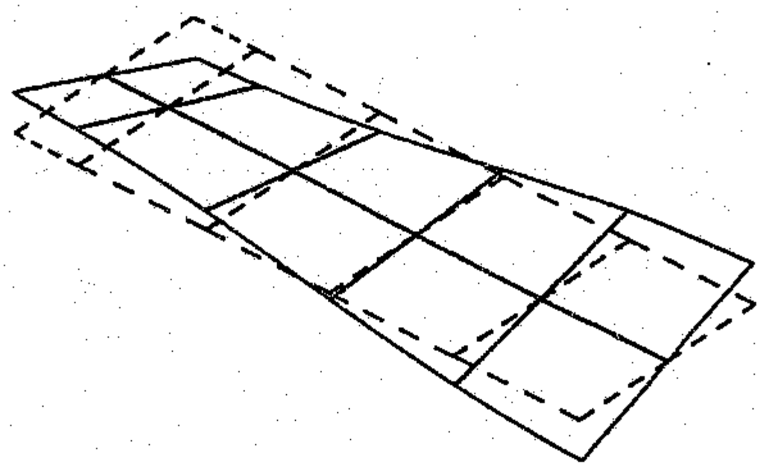

Figure C.5: FEM 5 – plate mode 8: 57.0 Hz

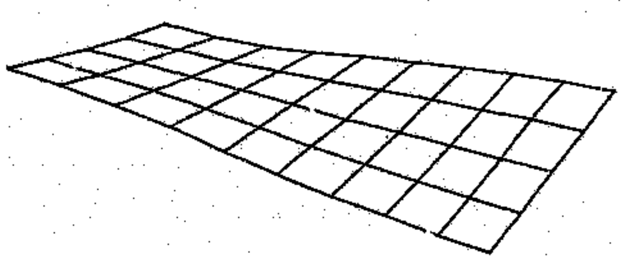

Figure C.6: EMA – plate mode 2: 49.4 Hz

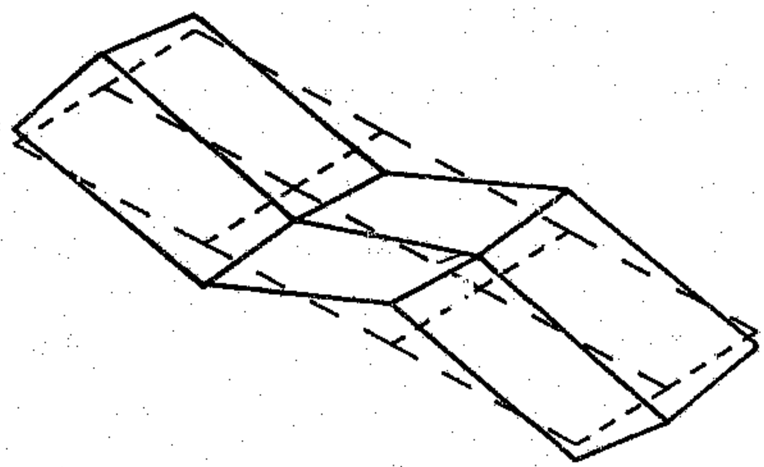

Figure C.7: FEM 1 – plate mode 12: 82.0 Hz

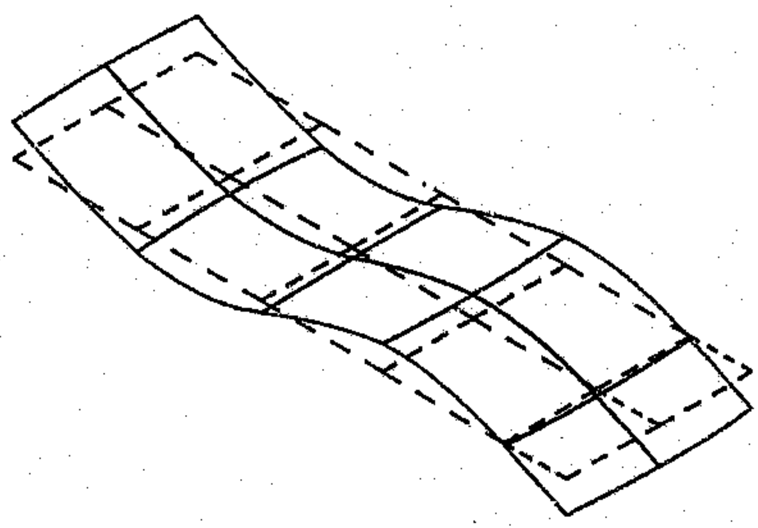

Figure C.8: FEM 5 – plate mode 10: 87.7 Hz

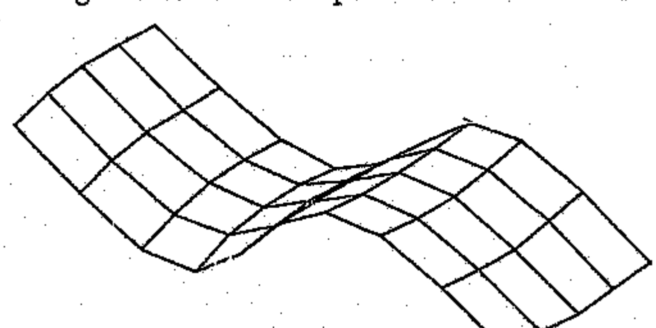

Figure C.9: EMA – plate mode 3: 80.1 Hz

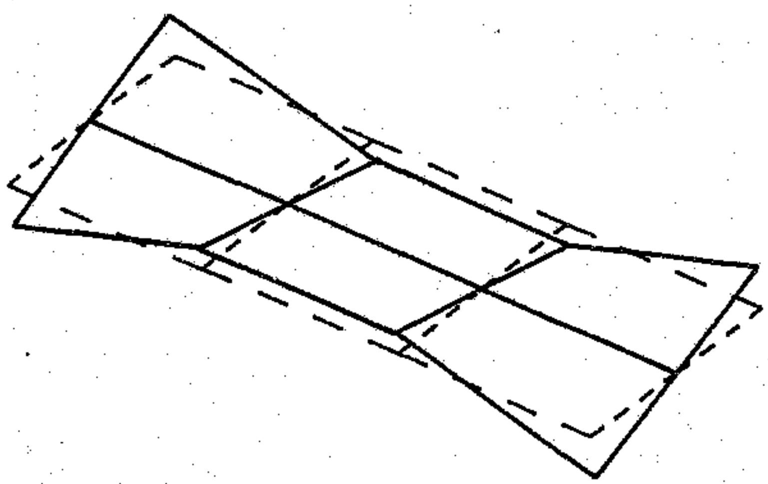

Figure C.10: FEM 1 – plate mode 11: 77.5 Hz

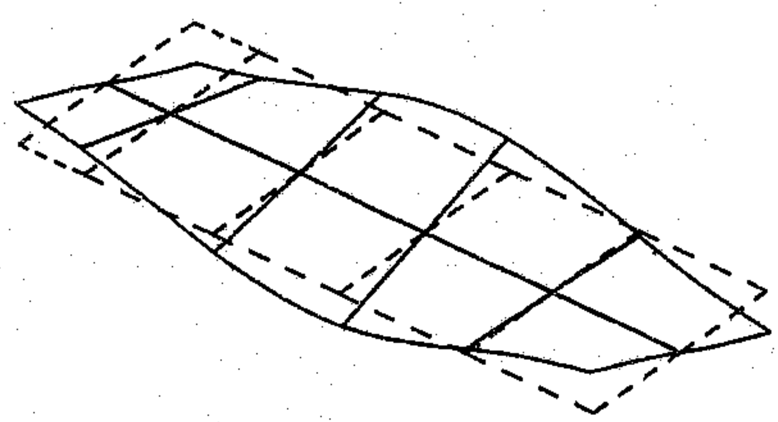

Figure C.11: FEM 5 – plate mode 12: 121.1 Hz

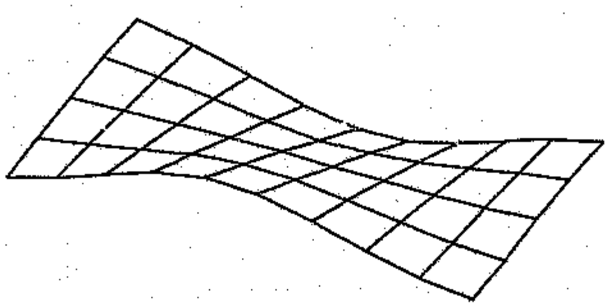

Figure C.12: EMA – plate mode 4: 103.6 Hz

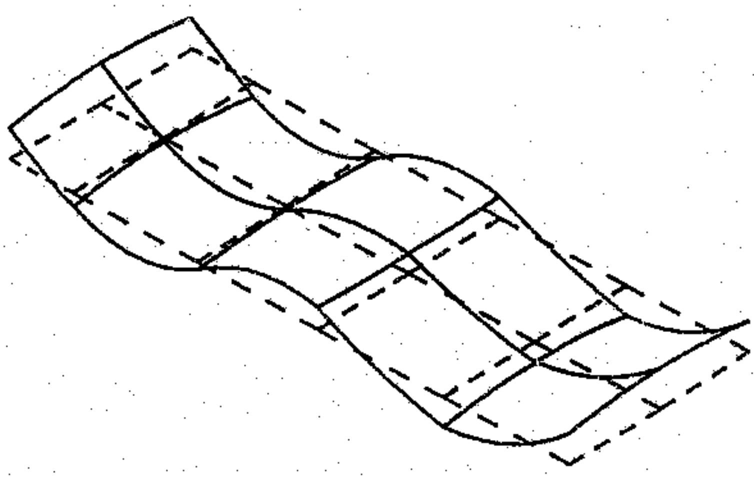

Figure C.13: FEM 5 – plate mode 13: 174.9 Hz

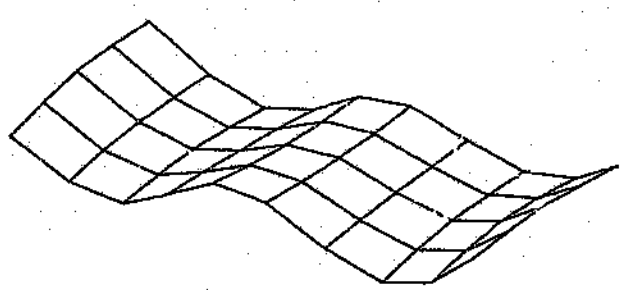

Figure C.14: EMA – plate mode 5 157.3 Hz

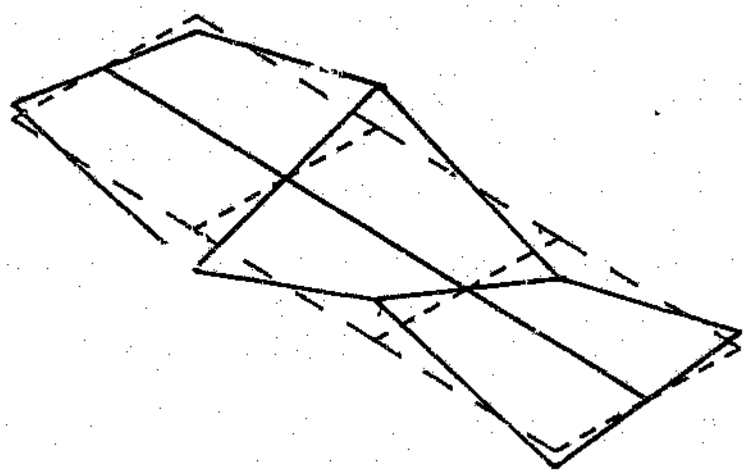

Figure C.15: FEM 1 – plate mode 10: 59.9 Hz

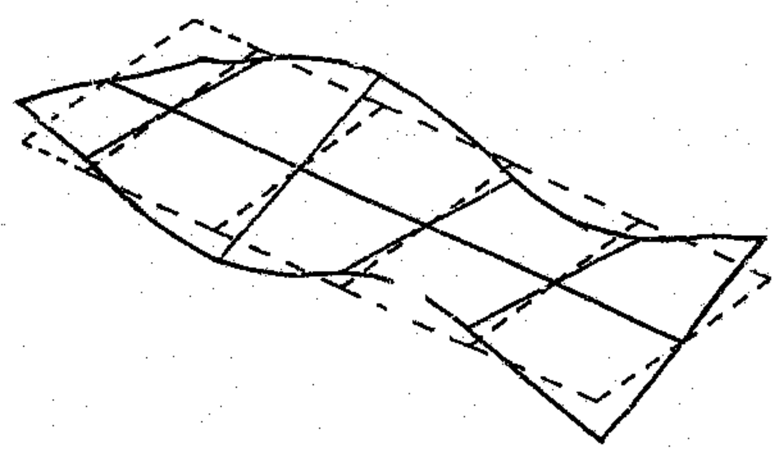

Figure C.16: FEM 5 – plate mode 14: 198.2 Hz

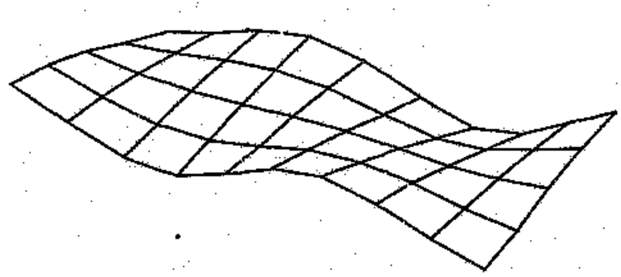

Figure C.17: EMA – plate mode 6 173.1 Hz

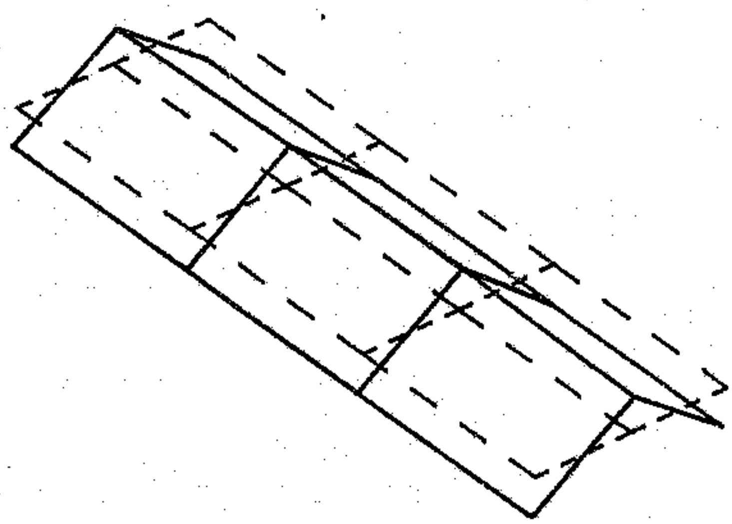

Figure C.18: FEM 1 – plate mode 16: 211.5 Hz

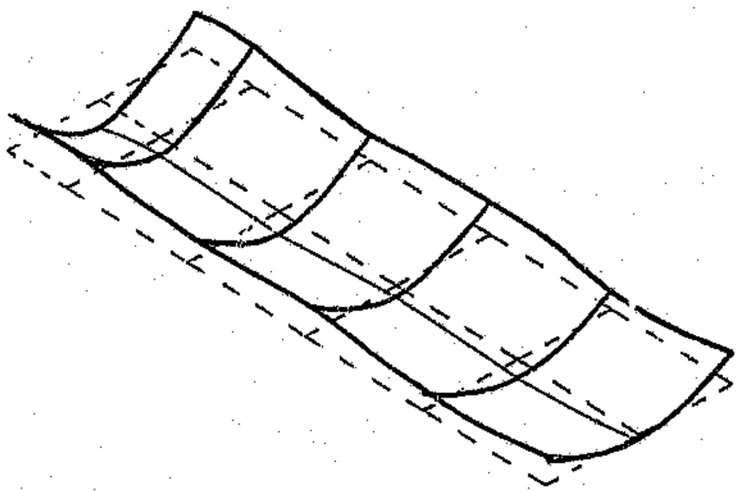

Figure C.19: FEM 5 – plate mode 17: 303.6 Hz

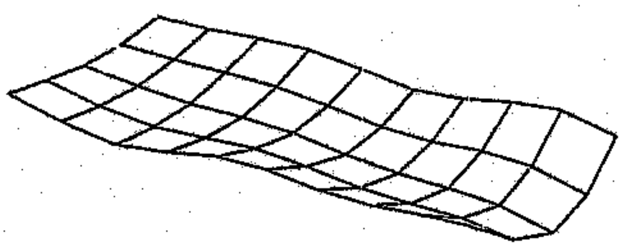

Figure C.20: EMA – plate mode 7 245.8 Hz

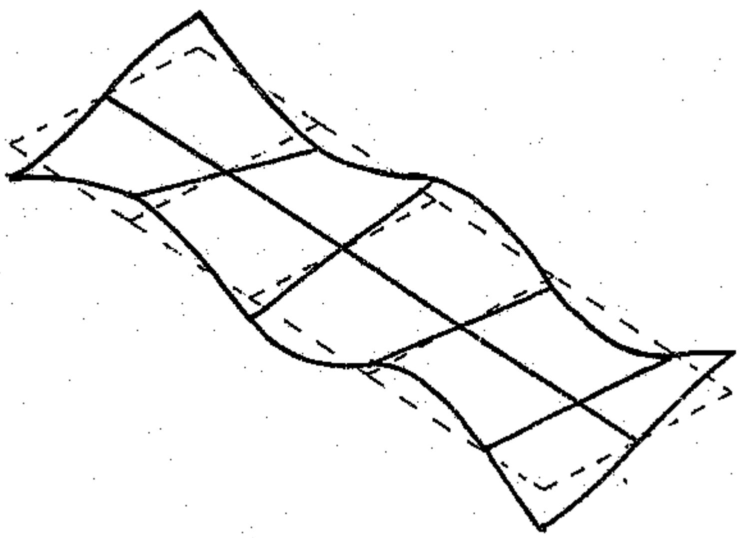

Figure C.21: FEM 5 – plate mode 16: 294.5 Hz

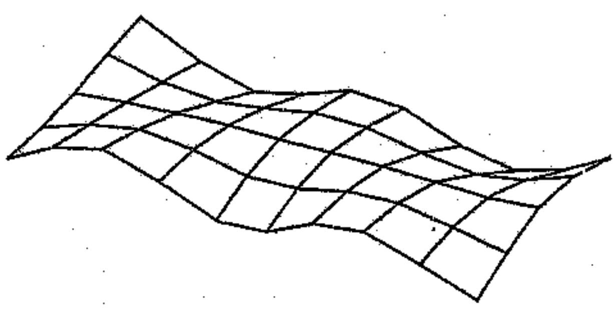

Figure C.22: EMA – plate mode 8 254.5 Hz

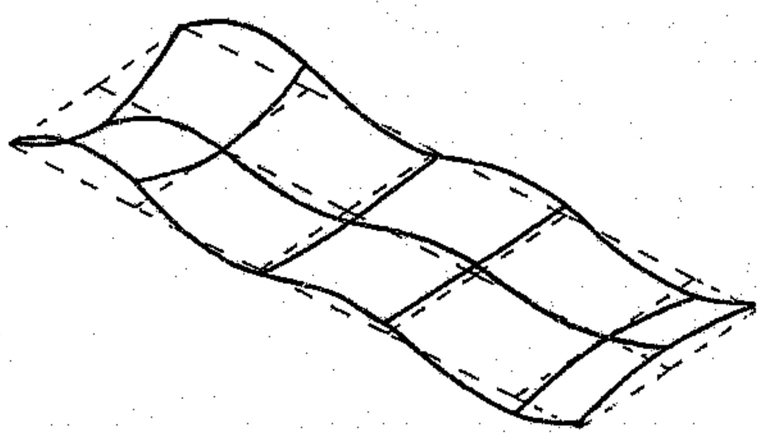

Figure C.23: FEM 5 – plate mode 15: 286.7 Hz

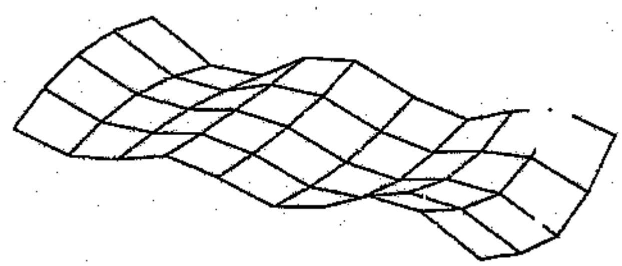

Figure C.24: EMA – plate mode 9 258.7 Hz

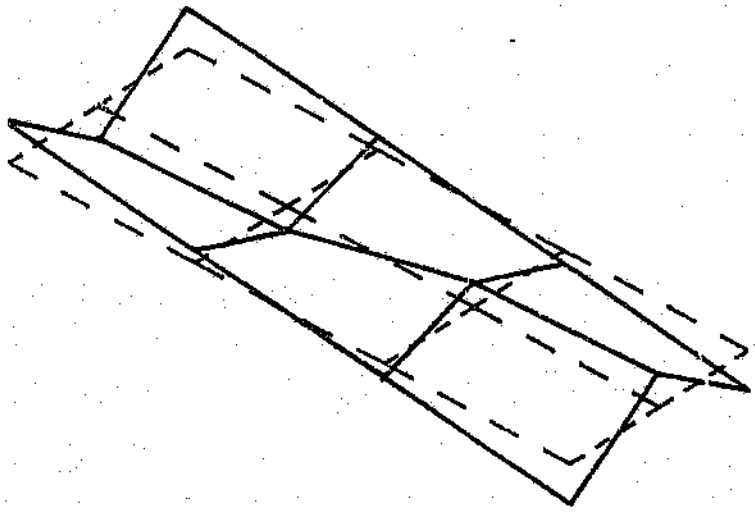

Figure C.25: FEM 1 – plate mode 15: 186.9 Hz

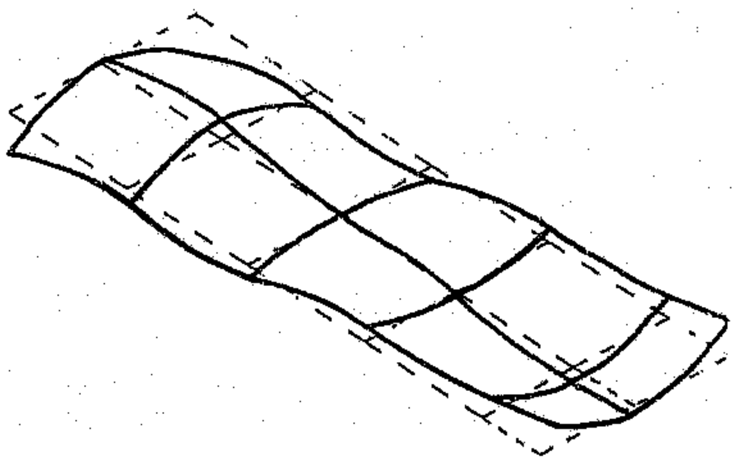

Figure C.26: FEM 5 – plate mode 18: 335.6 Hz

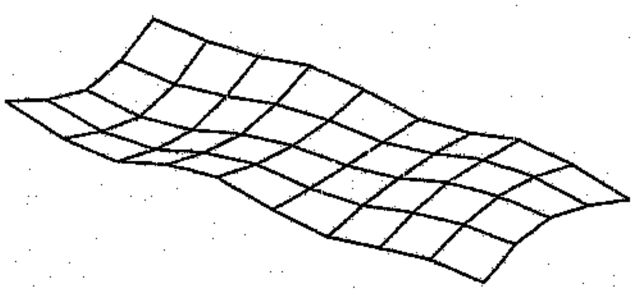

Figure C.27: EMA – plate mode 10 279.4 Hz

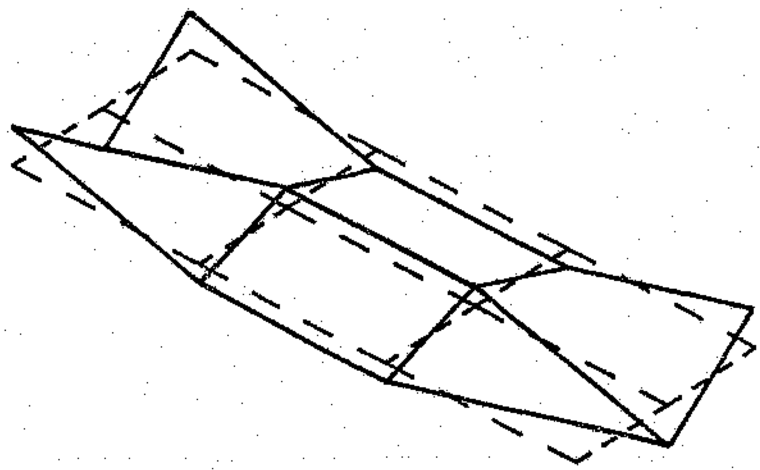

Figure C.28: FEM 1 – plate mode 13: 101.1 Hz

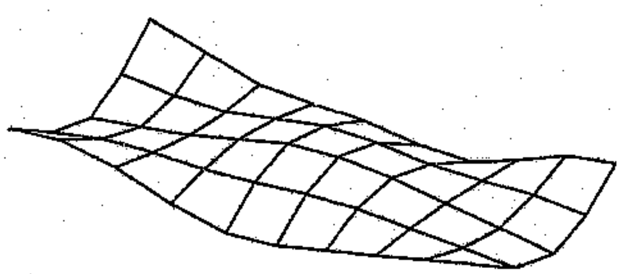

Figure C.29: EMA – plate mode 11 321.4 Hz

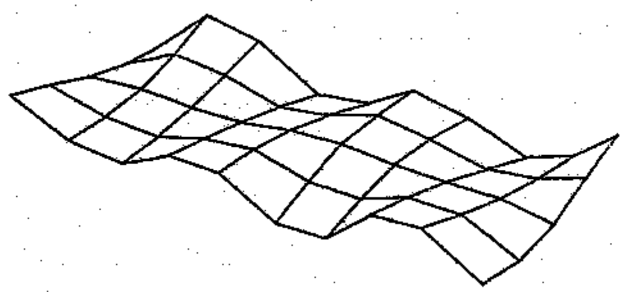

Figure C.30: EMA – plate mode 12 365.5 Hz

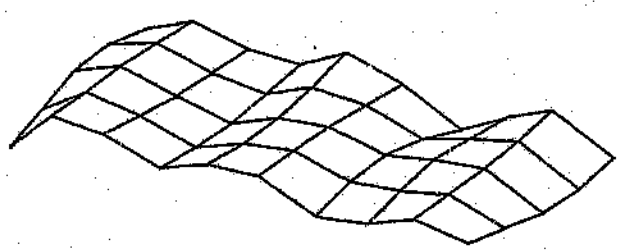

Figure C.31: EMA – plate mode 13 400.2 Hz

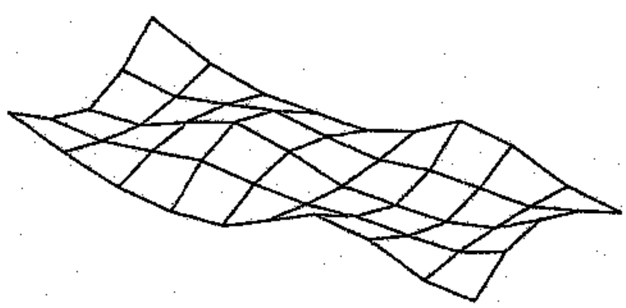

Figure C.32: EMA – plate mode 14 414.5 Hz

Table C.1: Cross-MAC for plate: FEM 2 vs EMA

Modal Assurance Criteria (%)								
Mode no		1	2	3	4	5	6	7
Freq (Hz)		27.39	49.37	80.10	103.59	157.26	173.10	245.83
7	8.77	0.0	0.0	0.4	0.0	0.0	0.0	0.3
8	30.20	**95.9**	0.4	0.1	0.0	3.9	0.4	0.6
9	43.47	1.1	0.0	0.0	0.0	0.9	0.0	2.0
10	46.08	0.0	**98.9**	0.4	0.2	0.0	1.9	0.2
11	71.10	0.0	0.0	1.1	0.0	0.0	0.0	0.6
12	81.73	0.0	0.0	**97.8**	0.4	0.1	0.0	0.2
13	95.11	0.1	0.0	0.0	**98.2**	1.5	1.4	0.0
14	101.60	1.2	0.0	0.0	0.0	1.6	0.0	2.1
15	128.71	0.0	0.0	0.9	0.0	0.0	0.0	0.2
16	142.23	2.3	0.0	0.0	0.0	**63.6**	2.0	0.4
17	148.09	0.0	5.6	0.0	0.3	3.4	**93.4**	1.6
18	166.37	1.6	0.1	0.0	0.0	17.4	1.1	12.3

Mode no		8	9	10	11	12	13	14
Freq (Hz)		254.51	258.65	279.36	321.44	365.48	400.22	414.52
7	8.77	0.2	0.1	2.3	0.0	0.1	0.5	2.7
8	30.20	0.0	0.0	0.0	17.6	1.6	4.8	2.2
9	43.47	0.1	0.2	0.0	4.6	0.0	2.3	0.4
10	46.08	0.0	0.3	0.0	0.0	2.0	0.5	0.0
11	71.10	0.3	0.0	5.0	0.0	0.1	1.2	4.9
12	81.73	0.1	1.6	1.2	0.1	0.2	3.0	22.4
13	95.11	2.3	0.2	1.1	0.0	0.2	0.1	0.0
14	101.60	0.1	0.3	0.0	4.0	0.0	12.4	1.4
15	128.71	0.2	3.1	14.0	0.0	0.1	0.7	4.7
16	142.23	0.0	0.0	0.2	0.0	0.0	0.1	0.2
17	148.09	0.2	0.9	0.1	0.0	4.3	0.9	0.0
18	166.37	0.8	1.3	0.1	37.0	5.0	4.0	0.0

Table C.2: Cross-MAC for plate: FEM 3 vs EMA

Modal Assurance Criteria (%)								
Mode no		1	2	3	4	5	6	7
Freq (Hz)		27.39	49.37	80.10	103.59	157.26	173.10	245.83
7	17.21	0.0	0.0	0.2	0.0	0.0	0.0	0.0
8	30.36	**96.6**	0.3	0.1	0.0	5.7	0.7	0.0
9	53.35	0.0	**99.0**	0.3	0.2	0.0	2.3	0.3
10	83.51	0.0	0.0	**98.8**	0.5	0.1	0.0	0.8
11	111.13	0.1	0.0	0.0	**98.2**	1.1	1.4	0.0
12	164.57	3.2	0.0	0.0	0.1	**94.9**	4.3	0.8
13	174.80	0.0	5.3	0.0	0.3	2.6	**92.7**	1.9
14	252.18	1.4	0.1	0.3	4.9	0.0	0.1	6.0
15	255.17	0.0	0.0	0.1	0.0	0.0	0.1	20.1
16	258.01	3.4	0.2	0.1	0.1	0.8	0.2	**68.8**
17	294.95	0.0	0.0	0.5	0.1	0.0	0.0	0.7
18	300.13	8.4	0.1	0.1	0.0	0.2	0.0	3.7
Mode no		8	9	10	11	12	13	14
Freq (Hz)		254.51	258.65	279.36	321.44	365.48	400.22	414.52
7	17.21	0.0	0.0	0.5	0.0	0.0	0.1	0.5
8	30.36	0.1	0.0	0.1	3.9	0.3	5.4	2.2
9	53.35	0.1	0.3	0.0	0.0	2.6	0.8	0.1
10	83.51	0.3	3.4	1.8	0.0	0.0	0.4	5.0
11	111.13	3.5	0.2	1.5	0.1	0.2	0.1	0.1
12	164.57	0.1	0.2	0.2	0.8	0.3	5.4	0.5
13	174.80	0.2	0.7	0.2	0.0	6.3	1.4	0.0
14	252.18	**72.7**	9.7	8.5	3.9	1.5	0.4	0.1
15	255.17	5.4	**62.6**	16.5	1.0	0.0	0.8	5.1
16	258.01	17.4	6.3	5.0	1.6	0.1	0.7	0.3
17	294.95	0.4	9.5	**72.5**	1.6	0.3	0.4	1.8
18	300.13	0.1	0.1	0.0	**86.5**	7.4	0.0	2.1

Table C.3: Cross-MAC for plate: FEM 4 vs EMA

Modal Assurance Criteria (%)								
Mode no		1	2	3	4	5	6	7
Freq (Hz)		27.39	49.37	80.10	103.59	157.26	173.10	245.83
7	31.41	**96.5**	0.3	0.0	0.0	9.4	1.0	0.0
8	57.00	0.0	**99.0**	0.3	0.1	0.0	3.3	0.3
9	88.44	0.0	0.0	**98.2**	0.6	0.2	0.0	0.9
10	120.94	0.1	0.1	0.0	**98.2**	1.1	1.1	0.0
11	180.31	13.6	0.1	0.0	0.0	**94.7**	4.4	0.2
12	201.01	0.0	8.0	0.0	0.4	2.6	**92.7**	1.8
13	304.08	1.5	0.0	0.3	10.2	0.0	0.2	5.4
14	305.69	0.0	0.0	8.2	0.1	1.0	0.0	4.7
15	311.03	2.8	0.2	0.1	0.1	0.1	0.4	**83.7**
Mode no		8	9	10	11	12	13	14
Freq (Hz)		254.51	258.65	279.36	321.44	365.48	400.22	414.52
7	31.41	0.0	0.0	0.2	5.6	0.3	8.1	3.2
8	57.00	0.0	0.3	0.0	0.0	3.5	1.0	0.1
9	88.44	0.4	4.9	2.8	0.0	0.0	0.0	8.1
10	120.94	4.5	0.3	1.7	0.1	0.2	0.1	0.1
11	180.31	0.1	0.8	0.8	0.2	0.2	7.9	1.2
12	201.01	0.1	0.8	0.2	0.0	5.3	1.4	0.1
13	304.08	**71.7**	9.7	8.9	3.9	2.3	0.4	0.1
14	305.69	10.1	**84.3**	5.7	1.2	0.0	0.0	2.9
15	311.03	12.9	0.2	2.4	1.5	0.2	0.6	0.0

Appendix D

PRESIDENT STEYN NUMBER 4 SHAFT CHARACTERISTICS

The shaft steelwork parameters and calculations are presented in this section.

D.1 SHAFT STEELWORK

The stiffness of the guide-bunton system varies from a maximum at one of the buntons to a minimum at the mid span of the buntons. The maximum stiffness k_{max}, is that of the bunton, k_b. The minimum stiffness k_{min}, is the effective stiffness of the bunton and guide, in parallel:

$$k_{max} = k_b$$

$$\frac{1}{k_{min}} = \frac{1}{k_b} + \frac{1}{k_g}$$

where k_g is the stiffness at mid span of the guide mounted on rigid supports. The average stiffness k_0, is given by:

$$k_0 = \frac{1}{2}(k_{max} + k_{min})$$

and the variation above and below this average stiffness is:

$$\mu = \frac{(k_{max} + k_{min})}{2k_0}$$

For President Steyn number 4 shaft, $k_b = 26\ 330$ Nmm^{-1} and $k_g = 810$ Nmm^{-1} (figures taken from [4]), therefore:

$$k_0 = 13\ 558\ Nmm^{-1}$$

$$\mu = 0.942$$

The hoisting speed is 15.24 ms^{-1} and the bunton spacing, l_0 is 6.1 m, resulting in a bunton passing frequency of 2.5 Hz or 15.7 rads^{-1}.

D.2 SKIP

The mass m_s of the fully loaded skip is approximately 27 800 kg. The distance between the two extreme guide shoes, l is approximately 11 m. The average natural frequencies of translation and rotation, Ω_1 and Ω_2 respectively, of the skip-steelwork system are given by [11]:

$$\Omega_1 = \sqrt{\frac{2k_0}{m_s}} = 31.2\ rads^{-1}$$

$$\Omega_2 = \frac{l}{r}\sqrt{\frac{k_0}{m_s}} = 53.6\ rads^{-1}$$

where r is the radius of gyration of the skip in the plane of the guides. The ratios of the bunton passing frequency to the skip frequencies are as follows:

$$\eta_1 = \frac{15.7}{31.2} = 0.50$$

$$\eta_2 = \frac{15.7}{53.6} = 0.29$$

The stability intervals of the first kind, first order are:

$$2\Omega_s - \frac{1}{2}\mu a_{ss} < \omega < 2\Omega_s + \frac{1}{2}\mu a_{ss}$$

and of the second kind, first order:

$$|\Omega_1 + \Omega_2| - \frac{1}{2}\mu\sqrt{a_{12}a_{21}} < \omega < |\Omega_1 + \Omega_2| + \frac{1}{2}\mu\sqrt{a_{12}a_{21}}$$

where $a_{11} = a_{22} = \frac{1}{2}\sqrt{2(1+\cos\psi)}$ and $a_{12} = a_{21} = \frac{1}{2}\sqrt{2(1-\cos\psi)}$ and ψ is the phase difference between the guide shoes: $\psi = \frac{l-l_0}{l}$.

For the skip, these intervals (in rads^{-1}) are:

of the first kind:
$62.3 < \omega < 62.5$
$107.1 < \omega < 107.3$

of the second kind:
$84.3 < \omega < 85.2$

D.3 CAGE

The mass of a fully loaded cage is approximately 15000 kg. The distance between the two extreme guide shoes is approximately 10 m. The resulting natural frequencies for the cage are found using the equations shown above:

$$\Omega_1 = 42.5 \quad rads^{-1}$$

$$\Omega_2 = 72.8 \quad rads^{-1}$$

The ratios of the bunton passing frequency to the cage frequencies are as follows:

$\eta_1 = \frac{15.7}{42.5} = 0.37$

$\eta_2 = \frac{15.7}{72.8} = 0.22$

The stability intervals are:

of the first kind:

$84.9 < \omega < 85.2$
$145.5 < \omega < 145.8$

of the second kind:
$114.9 < \omega < 115.8$

D.4 COMPARISON OF COMRO/SDRC DESIGN GUIDELINES WITH THE RESONANCE CURVE OF SCHMIDT/TONDL

In this section, an attempt is made to correlate the findings of the COMRO/SDRC with those of Schmidt and Tondl. The dimensionless parameters of the COMRO/SDRC design guidelines are manipulated to become analogous to those defined by Schmidt/Tondl. Scaling factors are ignored as the trends that are observed that are of interest. An explanation of the parameters discussed may be found in Chapter 3 and references [11] and [4].

The "dimensionless skip displacement" $\bar{h}$ of COMRO/SDRC is analogous to the parameter A defined by Schmidt/Tondl.

The "dimensionless bunton stiffness" of the COMRO/SDRC design guidelines is defined as:

$$\bar{k_b} = \frac{k_b l_0^2}{m_e v^2}$$

where k_b, l_0 and v are as defined above and m_e is the "effective" mass of the conveyance at the guide shoe. It is the effective mass that acts at the guide shoe during an impact. The square root of $\bar{k}_b$ is a frequency of the conveyance-steelwork system, although it requires correct scaling before it becomes either the translation or rotational natural frequency. If the term is then inverted, it becomes analogous to the variable η defined by Schmidt and Tondl.

The following data was read off the plot for dimensionless bunton displacement in [4], for a value of bunton-to-guide stiffness ratio of 32.5 (President Steyn number 4 shaft):

This data is plotted in Figure D.1:

Table D.1: $\bar{h}$ and $\bar{k}_b$: bunton-to-guide stiffness ratio = 32.5

h	.004	.003	.002	.0015	.001
k_b	19	61	180	350	810

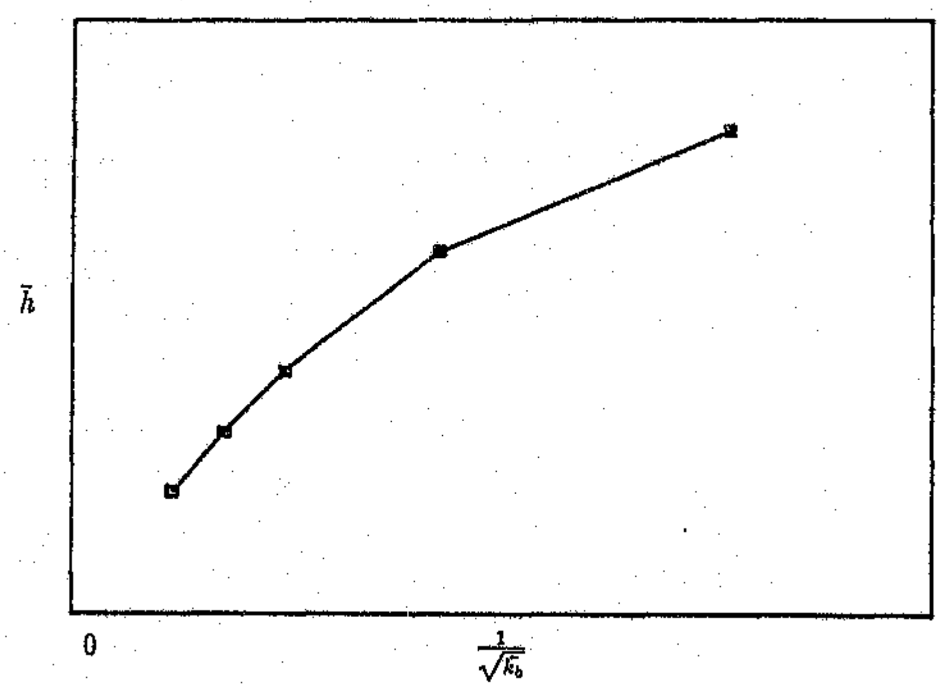

Figure D.1: $\bar{h}$ versus $\bar{k}_b$

Appendix E

CAGE FEM MODEL DATA

The properties of the beam and shellelements used in the FEM models are presented here. The material properties used are given in Table E.1. Different beam cross-sections are associated with a particular element "set". Each element set is given a code name to enable quick identification and for use in the FEM model. Beams and shells belonging to these element sets are indicated in Figures E.1 – E.3. Figure E.1 is a general arrangement of the cage Figures E.2 – E.3 are cross sections through the cage at the levels indicated in Figure E.1, showing the network of beams at each level. The properties defining the beams and shells are given in Tables E.2 and E.3. Table E.4 indicates which beams belong to the element sets.

In cases where the beam centroidal axes were offset from the required or chosen node position, the properties about an axis through this position were calculated. This is equivalent to using a rigid offset to offset the beam axis from a node position.

Table E.1: Material Properties

Material	Young' Modulus GPa	Shear Modulus GPa	Density kg^{-3}
Steel	206	79	7850
Aluminium	79	26	2770

The properties listed in Table E.2 are:

A: Cross-section area

$\mathbf{I}_x$: First moment of area about local beam x-axis

$\mathbf{I}_y$: First moment of area about local beam y-axis

Table E.2: Beam Section Properties

Code (Material)	A m^2	I_x m^3	I_y m^3	I_{xx} m^4	I_{xy} m^4	I_{yy} m^4	J m^4
1 Steel	6.855 x10^{-3}	0	0	1.0190 x10^{-5}	0	1.8670 x10^{-4}	1.9689 x10^{-4}
2 Aluminium	8.214 x10^{-3}	4.2915 x10^{-5}	1.0432 x10^{-3}	3.4704 x10^{-6}	-3.3168 x10^{-6}	2.7388 x10^{-4}	2.7735 x10^{-4}
3 Aluminium	5.230 x10^{-3}	-2.6150 x10^{-5}	-7.4005 x10^{-4}	1.7433 x10^{-7}	3.7002 x10^{-6}	2.2393 x10^{-4}	2.2410 x10^{-4}
4 Aluminium	6.800 x10^{-3}	3.5474 x10^{-5}	-6.4769 x10^{-4}	2.9695 x10^{-6}	-2.0551 x10^{-6}	1.4757 x10^{-4}	1.5054 x10^{-4}
5 Aluminium	4.500 x10^{-3}	0	-4.7250 x10^{-4}	3.7500 x10^{-8}	0	1.2555 x10^{-4}	1.2559 x10^{-4}
6 Aluminium	2.299 x10^{-3}	5.7974 x10^{-5}	1.7519 x10^{-4}	2.8195 x10^{-6}	4.4146 x10^{-6}	2.2022 x10^{-5}	2.4841 x10^{-5}
7 Aluminium	1.150 x10^{-3}	-2.5272 x10^{-5}	6.2339 x10^{-5}	1.1854 x10^{-6}	-1.7427 x10^{-6}	4.01 x10^{-6}	5.1954 x10^{-6}
8 Aluminium	7.864 x10^{-3}	4.4665 x10^{-8}	-1.0791 x10^{-6}	3.4588 x10^{-6}	-3.1374 x10^{-6}	2.7017 x10^{-4}	2.7363 x10^{-4}
9 Aluminium	6.769 x10^{-3}	3.5624 x10^{-5}	-7.9428 x10^{-4}	2.9685 x10^{-6}	-1.3222 x10^{-6}	1.8220 x10^{-4}	1.8516 x10^{-4}
10 Aluminium	2.299 x10^{-3}	5.7974 x10^{-5}	5.7519 x10^{-4}	2.8195 x10^{-6}	4.416 x10^{-6}	2.2022 x10^{-5}	2.4841 x10^{-5}
11 Aluminium	1.240 x10^{-2}	2.0198 x10^{-7}	-2.4452 x10^{-6}	1.5767 x10^{-5}	-6.1304 x10^{-5}	7.7238 x10^{-4}	7.8814 x10^{-4}
12 Aluminium	2.984 x10^{-3}	6.907 x10^{-5}	-9.0952 x10^{-4}	3.2961 x10^{6}	-2.105 x10^{-5}	2.9637 x10^{-4}	2.9967 x10^{-4}
13 Aluminium	2.181 x10^{-3}	0	-1.6617 x10^{-4}	1.1147 x10^{-6}	0	2.1002 x10^{-5}	2.2116 x10^{-5}
14 Aluminium	2.299 x10^{-3}	5.7974 x10^{-5}	-1.7519 x10^{-4}	2.8195 x10^{-6}	-4.4177 x10^{-6}	2.2022 x10^{-5}	2.4841 x10^{-5}
15 Aluminium	8.534 x10^{-3}	0	-5.103 x10^{-5}	2.9241 x10^{-6}	0	7.8438 x10^{-5}	8.1362 x10^{-5}
16 Aluminium	7.619 x10^{-3}	0	8.9462 x10^{-5}	2.0875 x10^{-6}	0	3.6498 x10^{-5}	3.8585 x10^{-5}
17 Aluminium	1.919 x10^{-3}	0	9.2612 x10^{-5}	3.7307 x10^{-7}	0	5.9426 x10^{-6}	6.3157 x10^{-6}
18 Aluminium	3.696 x10^{-3}	0	-3.7556 x10^{-4}	1.9513 x10^{-6}	0	6.2942 x10^{-5}	6.4894 x10^{-5}
19 Steel	1.388 x10^{-2}	0	-1.6288 x10^{-3}	2.9390 x10^{-5}	0	8.5914 x10^{-4}	8.8852 x10^{-4}
BRIDLE Aluminium	7.320 x10^{-3}	1.1153 x10^{-4}	0	4.4982 x10^{-6}	0	3.1369 x10^{-4}	3.1819 x10^{-4}
RANGLE Aluminium	1.844 x10^{-3}	5.3308 x10^{-5}	5.3308 x10^{-5}	3.3546 x10^{-6}	4.6572 x10^{-7}	3.3546 x10^{-6}	6.7092 x10^{-6}
FANGLE Aluminium	3.294 x10^{-3}	-2.4891 x10^{-5}	-1.1513 x10^{-4}	2.5786 x10^{-6}	3.6681 x10^{-6}	1.1014 x10^{-5}	1.3593 x10^{-5}

I_{xx}: Second moment of area about local beam x-axis

I_{xy}: Product of area about local beam x- and y-axes

I_{yy}: Second moment of area about local beam y-axis

J: Torsional constant

Table E.3: Shell Properties

Code	Material	Thickness mm
BOX	Aluminium	10
SCREENS	Aluminium	3

Table E.4: Allocation of beams to element sets

Code	Points defining beams in element sets (refer to Figures E.1 – E.3)
1	[4–24] [5–25]
2	[1–4] [5–6] [6–11] [20–26] [21–24] [25–26]
3	[4–5] [24–25]
4	[31–35] 35–47] [43–47]
5	[30–31] [42–43]
6	[51–53] 56–58] [51–56] [50–55]
7	[54–59] [53–54] [58–59] [60–62] [63–64] [66–68] [69– 70]
8	[1–21]
9	[30–42]
10	[60–66] [61–67] [64–70] [65–71]
11	[11–20]
12	[2–8] [3–9] [17–22] [18–23] [10–19]
13	[32–44] [33–45] [34–46] [52–57] [53–60]
14	[31–43]
15	[7–11] [16–20]
16	[37–38] [40–41]
17	[36–37] [39–40]
18	[12–13] [14–15]
19	[62–68] [63–69]

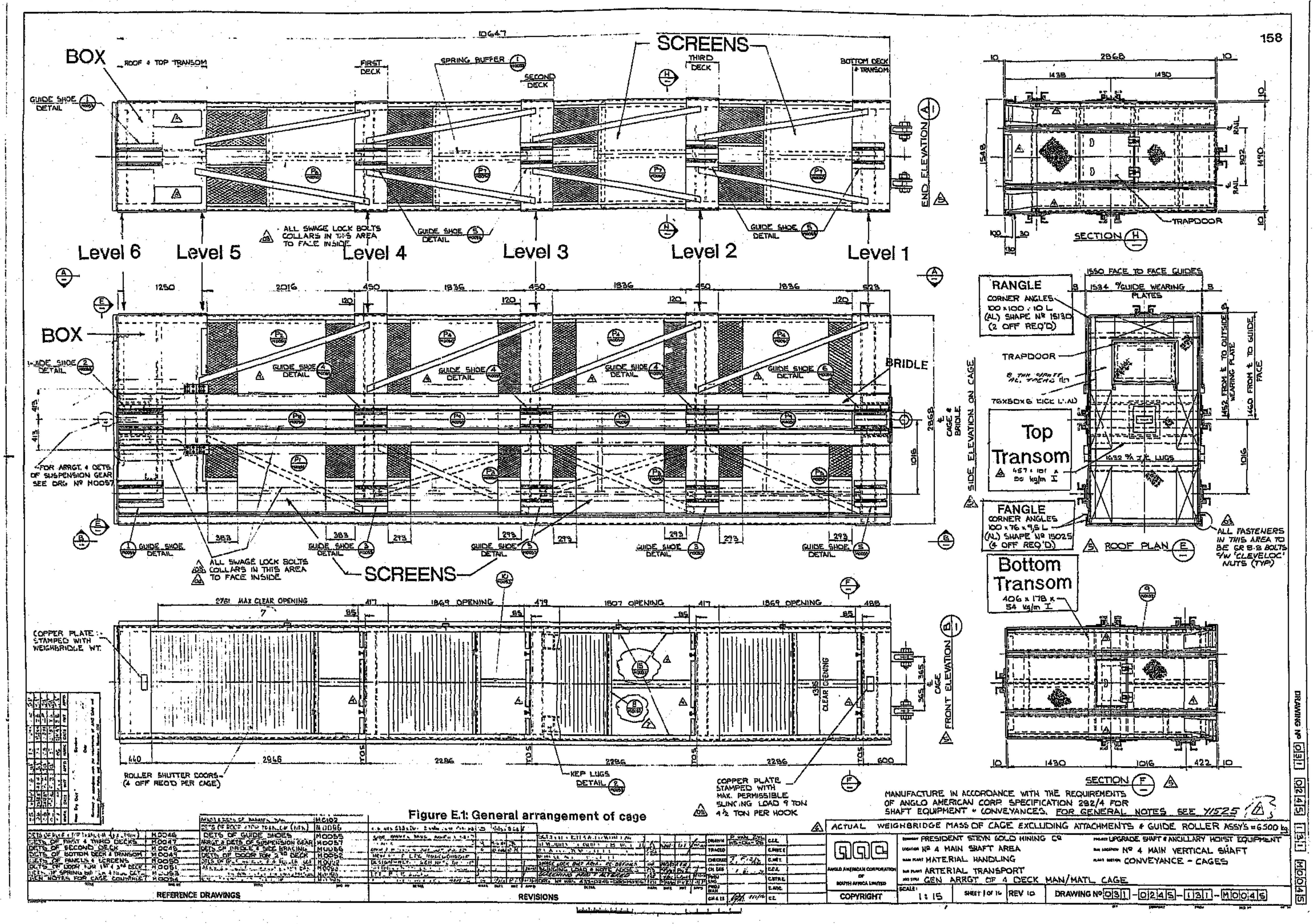

Figure E.1: General arrangement of cage

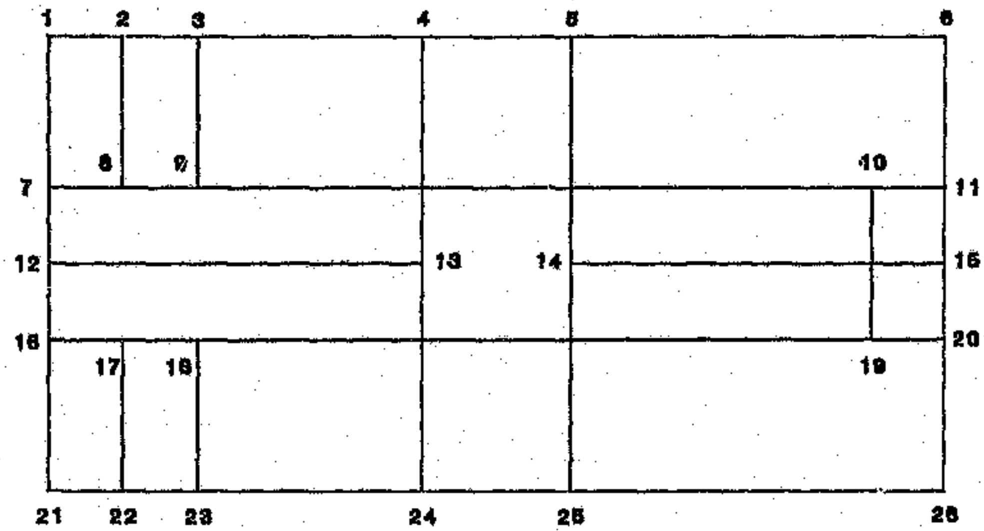

Level "1"

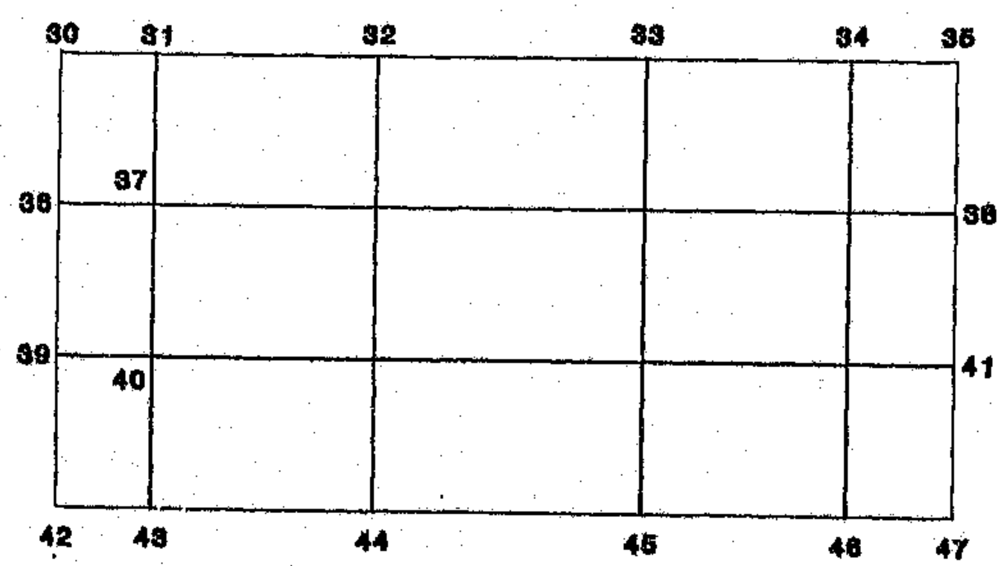

Levels "2","3" and "4"

Figure E.2: Element sets for deck beams

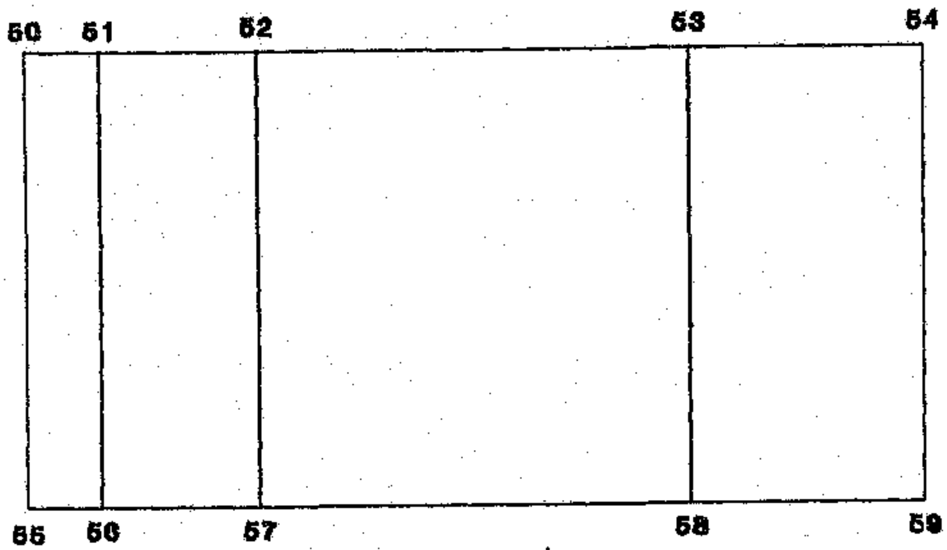

Level "5"

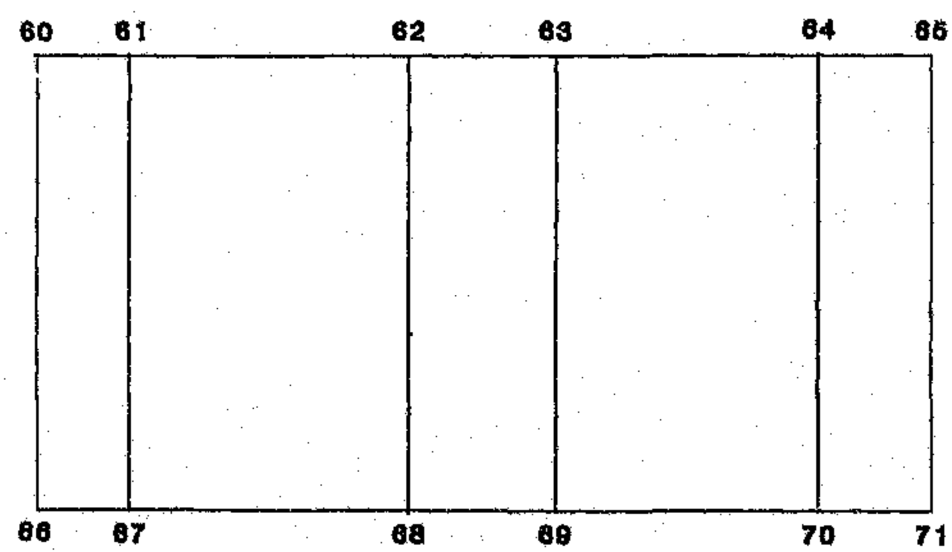

Level "6"

Figure E.3: Element sets for beams at top of cage

Appendix F

COMPUTER PROGRAMME LISTING

F.1 PROGRAMME "MAC"

This programme, written in Turbopascal 4.0, was used to calculate the modal assurance criteria, co-ordinate modal assurance criteria from two separate analyses.

```
{$M 60000,0,655360}
program modal_assurance_criteria;
{********************** *********************************************
   THIS PROGRAM CALCULATES THE MODAL ASSURANCE CRITERIA AND
   CO-ORDINATE MODAL ASSURANCE CRITERIA BETWEEN DATA FROM
   TWO ANALYSES.

   WRITTEN BY
                      STEVEN ROBERT GROBLER
                          29 JUNE 1988
********************************************************************}
uses
    crt,Graph,Printer;
const
     maxnn=50;        {maximum number of nodes}
     maxnm=15;        {maximum number of modes}

type
    array1=array[1..15] of integer;
    array2=array[1..15] of real;
    array3=array[1..15,1..50,1..4] of real;
    array4=array[1..15,1..15] of real;
    array5=array[1..50,1..3] of real;
    array6=array[1..15,1..50,1..3] of real;
var
   no_nodes                :integer;     {no nodes in comparison}
   no_amodes,no_bmodes     :integer·     {no A,B  modes to compare}
   lmax                    :integer;     {no node pairs to compare}
   amode_no,bmode_no       :array1;      {no's of the modes compared}
   amode_freq,bmode_freq   :array2;      {frequencies of modes compared}
   amode,bmode             :array3;      {mode shape array}
   mac                     :array4;      {modal assurance criteria}
   comac                   :array5;      {coord modal assurance crit}
   mag_dif                 :array6;      {mod difference between modes}
   namea,nameb             'string[15]; {names of A and B data files}
   name_out                :string[15]; {name of MAC output file}
   menu                    :pointer;     {pointer for main menu}
   MaxX                    :word;        {maximum screen X-coord}
   MaxY                    :word;        {maximum screen Y-coord}
   GraphDriver             :integer;     {graphics device driver}
   GraphMode               ;integer;     {graphics mode value}
   H                       :word;        {height of text for graphics}
   W                       :word;        {width of text for graphics}
{********************************************************************}
```

```
{$F+}
procedure Quit;
begin
     CloseGraph;
end;
{$F-}
{*******************************************************************}
function int2str(l:longint):string;  {conv  ts an integer to a string}
var
   s:string;
begin
     str(l,s);
     int2str:=s;
end;
{*******************************************************************}
function real2str(l:real):string; {converts a real number to a string}
var
   s:string[3];
   a:integer;
begin
     a:=trunc(l);
     str(a,s);
     real2str:=s;
end;
{*******************************************************************}
procedure Wait;                        {pauses until a key is struck}
var
   ch:Char;
begin
     ch:=ReadKey;
end;
{*******************************************************************}
procedure Initialize;                          {initializes graphics}
begin
     DirectVideo:=False;
     Graphdriver:=Detect;
     initGraph(GraphDriver,GraphMode,'');
     MaxX:=GetMaxX;
     MaxY:=GetMaxY;
end;
{*******************************************************************}
procedure Status(msg:string);     {status line on the graphics screen}
begin
     SetUserCharSize(4,5,3,5);
```

```
     SetLineStyle(0,0,1);
     SetTextStyle(1,0,UserCharSize);
     SetTextJustify(1,1);
     SetFillStyle(0,0);
     H:=Textheight('H'
     Bar(MaxX div 10,MaxY-H,MaxX div 10*9,MaxY);
     Rectangle(MaxX div 10,MaxY-H,MaxX div 10*9,MaxY);
     OutTextXY(MaxX div 2,MaxY-H*3 div 5,msg);
end;
{*****************************************************************}
procedure MenuBlock(var menu:pointer);              {draws the main menu}
var
   Size:word;
   x1  :word;
   x2  :word;
   y1  :word;
   y2  :word;
begin
     SetUserCharSize(5,5,4,6);
     SetLineStyle(0,0,1);
     SetTextStyle(1,0,UserCharSize);
     SetTextJustify(0,1);
     SetFillStyle(0,0);
     W:=Textwidth('H');
     H:=TextHeight('H');
     x1:=MaxX div 10;
     y1:=MaxY div 10;
     x2:=MaxX div 10*9;
     y2:=MaxY div 10+9*H;
     Bar(x1,y1,x2,y2+4);
     Rectangle(x1,y1,x2,y2+4);
     Line(x1+2*W,y1,x1+2*W,y2+4);
     OutTextXY(x1+W,y1+H div 2,'1  Read Modal Data');
     OutTextXY(x1+W,y1+3*H div 2,'2  Calculate MAC');
     OutTextXY(x1+W,y1+5*H div 2,'3  Calculate COMAC');
     OutTextXY(x1+W,y1+7*H div 2,'4  Display MAC');
     OutTextXY(x1+W,y1+9*H div 2,'5  Display COMAC');
     OutTextXY(x1+W,y1+11*H div 2,'6  Display Mod Diff Plot');
     OutTextXY(x1+W,y1+13*H div 2,'7  Print COMAC, MAC');
     OutTextXY(x1+W,y1+15*H div 2,'8  Output MAC to File');
     OutTextXY(x1+W,y1+17*H div 2,'Q  Quit');
     Size:=imageSize(x1,y1,x2,y2+4);
     getmem(menu,Size);
     GetImage(x1,y1,x2,y2+4,menu^);
```

```
end;
{*******************************************************************}
procedure Read_Modal_Data(var no_modes,no_nodes:integer;var mode_no:
array1;var mode_freq:array2;var mode:array3;name:string);
var
   filevar:Text;
   i,j,k:integer;
begin
     assign(filevar,name);
     reset(filevar);
     Read(filevar,no_modes);
     if no_modes > maxnm then
     begin
          RestoreCrtMode;
          WriteLn(#10,#10,'Max number of modes (15) exceeded',#10,
          #10);
          WriteLn(#7,'PROGRAM TERMINATED !!!!!!',#7,#10,#10,#10);
          halt;
     end;
     Read(filevar,no_nodes);
     if no_nodes > maxnn then
     begin
          RestoreCrtMode;
          WriteLn(#10,#10,'Max number of nodes (50) exceeded',
          #10,#10);
          WriteLn(#7,'PROGRAM TERMINATED !!!!!!',#7,#10,#10,#10);
          halt;
     end;
     for i:=1 to no_modes do
     begin
          ReadLn(filevar,mode_no[i],mode_freq[i]);
          for j:=1 to no_nodes do
          begin
               for k:=1 to 4 do
               begin
                    Read(filevar,mode[i,j,k]);
               end;
               ReadLn(filevar);
          end;
     end;
     close(filevar);
end;
{*******************************************************************}
procedure normalize_Data(var mode:array3;no_modes,no_nodes:integer);
```

```
var
   maxdef:array[1..15] of real;
   i,j,k:integer;
begin
     for i:=1 to no_modes do
     begin
          maxdef[i]:=0.0;
          for j:=1 to no_nodes do
          begin
               for k:=2 to 4 do
               begin
                    if abs(mode[i,j,k]) > maxdef[i] then
                    maxdef[i]:=abs(mode[i,j,k]);
               end;
          end;
     end;
     for i:=1 to no_modes do
     begin
          for j:=1 to no_nodes do
          begin
               for k:=2 to 4 do
               begin
                    mode[i,j,k]:=mode[i,j,k]/maxdef[i];
               end;
          end;
     end;
end;
{*********************************************************************}
procedure Calc_MAC(var mac:array4;no_amodes,no_bmodes:integer;amode,
bmode:array3;no_nodes:integer);
var
   a_b_conj:real;
   a_a_conj:real;
   b_b_conj:real;
   i,j,k,l:integer;
begin
     for i:=1 to no_amodes do
     begin
          for l:=1 to no_bmodes do
          begin
               a_b_conj:=0.0;
               a_a_conj:=0.0;
               b_b_conj:=0.0;
               for j:=1 to no_nodes do
```

```
                begin
                     for k:=2 to 4 do
                     begin
                          a_b_conj:=a_b_conj+amode[i,j,k]*bmode[l,j,k];
                          a_a_conj:=a_a_conj+sqr(amode[i,j,k]);
                          b_b_conj:=b_b_conj+sqr(bmode[l,j,k]);
                     end;
                end;
                mac[i,l]:=100*sqr(a_b_conj)/a_a_conj/b_b_conj;
            end;
      end;
end;
{*****************************************************************}
procedure Write_MAC(mac:array4;no_amodes,no_bmodes:integer;bmode_no,
amode_no:array1;amode_freq,bmode_freq:array2);
var
   i,j:integer;
begin
     clrscr;
     WriteLn('                             Modal Assurance Criteria',#10,#10);
     WriteLn('                                      mode no / freq (Hz)');
     Write('               ');
     for i:=1 to no_bmodes do
     begin
         Write(bmode_no[i]:3,'    ');
     end;
     Write(#10,#13,'               ');
     for i:=1 to no_bmodes do
     begin
         Write(bmode_freq[i]:6:2,' ');
     end;
     Write(#10,#13,'mode  freq ',#10,#13,' no    (Hz)',#13);
     for i:=1 to no_amodes do
     begin
          Write(#10,#13,amode_no[i]:3,' ',amode_freq[i]:6:2,' ');
          for j:=1 to no_bmodes do
          begin
               Write(mac[i,j]:5:1,'  ');
          end;
     end;
end;
{*****************************************************************}
procedure Calc_COMAC(var comac:array5;var mag_dif:array6;no_amodes,
no_bmodes:integer;amode,bmode:array3;no_nodes:integer;var lmax:
```

```
integer);
type
    array1=array[1..4] of real;
var
   pair:array[1..15,1..2] of integer;
   a_b:array1;
   a_a:array1;
   b_b:array1;
   i,j,k,l,m,n:integer;
begin
     Write(#13,#10,#10,'Input number of modes for comparison (>1)..');
     ReadLn(lmax);
     for i:= 1 to lmax do
     begin
          Write('row no. and column no. of the mode pair (i j)');
          Read(pair[i,1],pair[i,2]);
     end;
     for i:=1 to no_nodes do
     begin
          for k:=2 to 4 do
          begin
               a_b[k]:=0.0;
               a_a[k]:=0.0;
               b_b[k]:=0.0;
          end;
          for j:=1 to lmax do
          begin
               m:=pair[j,1];
               n:=pair[j,2];
               for k:=2 to 4 do
               begin
                    a_b[k]:=a_b[k]+abs(amode[m,i,k]*bmode[n,i,k]);
                    a_a[k]:=a_a[k]+sqr(amode[m,i,k]);
                    b_b[k]:=b_b[k]+sqr(bmode[n,i,k]);
                    mag_dif[j,i,k-1]:=abs(abs(amode[m,i,k])-
                    abs(bmode[n,i,k]));
               end;
          end;
          for k:=2 to 4 do
          begin
               comac[i,k-1]:=0.0;
               if a_a[k] > 0.0 then
               begin
                    if b_b[k] > 0.0 then
```

```
                    begin
                         comac[i,k-1]:=sqr(a_b[k])/a_a[k]/b_b[k];
                    end;
               end;
          end;
     end;
end;
{*********************************************************************}
procedure Write_comac(comac:array5;no_nodes:integer);
var
   i,j:integer;
begin
     clrscr;
     WriteLn('Co-ordinate Modal Assurance Criterion',#13,#10);
     WriteLn('                  ',' x-dir  ',' y-dir  ',' z-dir  ');
     for i:=1 to no_nodes do
     begin
          if (i = 21)
          or (i = 41) then
          begin
               wait;
          end;
          WriteLn('node no ',amode[1,i,1]:3:0,'  ',comac[i,1]:6:4,' ',
          comac[i,2]:6:4,'  ',comac[i,3]:6:4);
     end;
     Wait;
end;
{*********************************************************************}
procedure Display_Mod_Dif(mag_dif:array6;no_nodes,lmax:integer;amode:
array3);
var
   deltaX:word;
   deltaY:word;
   yaxis:word;
   XAxisLength:word;
   YAxisLength:word;
   i,j,k:integer;
begin
     SetUserCharSize(5,6,5,6);
     SetTextStyle(2,0,UserCharSize);
     SetTextJustify(1,1);
     H:=Textheight('H');
     W:=Textwidth('H');
     deltaX:=(GetMaxX-5*W-4) div (no_nodes-1);
```

```
XAxisLength:=(no_nodes-1)*deltaX;
YAxis:=(GetMaxY -14*H) div 3;
deltaY:=YAxis div 10;
YAxisLength:=deltay*10;
Setviewport(0,0,GetMaxX,GetMaxY,clipon);

for k:=1 to lmax do                      {loop over pairs - x-dir}
begin
     MoveTo(4*W,YAxisLength+H-Round(mag_dif[k,1,1]*YAxisLength));
     for i:=2 to no_nodes do      {loop over nodes}
     begin
          LineTo(4*W+(i-1)*deltaX,YAxisLength+H-
          Round(mag_dif[k,i,1]*YAxisLength));
     end;
end;

for k:=1 to lmax do                      {loop over pairs - y-dir}
begin
     MoveTo(4*W,YAxisLength*2+5*H-Round(mag_dif[k,1,2]*
     YAxisLength));
     for i:=2 to no_nodes do      {loop over nodes}
     begin
          LineTo(4*W+(i-1)*deltaX,YAxisLength*2+5*H-
          Round(mag_dif[k,i,2]*YAxisLength));
     end;
end;

for k:=1 to lmax do                      {loop over pairs - z-dir}
begin
     MoveTo(4*W,YAxisLength*3+9*H-Round(mag_dif[k,1,3]*
     YAxisLength));
     for i:=2 to ro_nodes do      {loop over nodes}
     begin
          LineTo(4*W+(i-1)*deltaX,YAxisLength*3+9*H-
          Round(mag_dif[k,i,3]*YAxisLength));
     end;
end;

Rectangle(4*W,H,XAxisLength+4*W,YAxisLength+H);
for i:=1 to no_nodes do
begin {x-axis ticks}
     line(4*W+(i-1)*deltaX,YAxisLength+H-H div 2,
     4*W+(i-1)*deltaX,YAxisLength+H+H div 2);
     OutTextXY(4*W+(i-1)*deltaX,YAxisLength+2*H,
```

```
    real2str(amode[1,i,1]));
end; {x-axis ticks}
OutTextXY(GetMaxX div 2,yaxislength+7*H div 2,'x-direction');
for i:=1 to 10 do
begin {y-axis ticks}
     line(W*7 div 2,YAxisLength+H-i*deltaY,
     W*9 div 2,YAxisLength+H-i*deltaY);
     OutTextXY(W*5 DIV 2,YAxisLength+H-i*deltaY,int2str(i*10));
end; {y-axis ticks}

Rectangle(4*W,YAXISLENGth+5*H,XAxisLength+4*W,YAxisLength*2+5*H);
for i:=1 to no_nodes do
begin {x-axis ticks}
    line(4*W+(i-1)*deltaX,YAxisLength*2+5*H-H div 2,
    4*W+(i-1)*deltaX,YAxisLength*2+[illegible] div 2);
    OutTextXY(4*W+(i-1)*deltaX,YAxisLength*2+5*H+H,
    real2str(amode[1,i,1]));
end; {x-axis ticks}
OutTextXY(GetMaxX div 2,yaxislength*2+15*H div 2,'y-direction');
for i:=1 to 10 do
begin {y-axis ticks}
     line(W*7 div 2,YAxisLength*2+5*H-i*deltaY,
     W*9 div 2,YAxisLength*2+5*H-i*de[illegible]);
     OutTextXY(W*5 DIV 2,YAxisLength*[illegible]H-i*deltaY,
     int2str(i*10));
end; {y-axis ticks}

Rectangle(4*W,yaxislength*2+9*H,XAxisLength+4*W,YAxisLength
*3+9*H);
for i:=1 to no_nodes do
begin {x-axis ticks}
    line(4*W+(i-1)*deltaX,YAxisLength*3+9*H-H div 2,
    4*W+(i-1)*deltaX,YAxisLength*3+9*H+H div 2);
    OutTextXY(4*W+(i-1)*deltaX,YAxisLength*3+10*H,
    real2str(amode[1,i,1]));
end; {x-axis ticks}
OutTextXY(GetMaxX div 2,yaxislength*3+23*H div 2,'z-direction');
for i:=1 to 10 do
begin {y-axis ticks}
     line(W*7 div 2,YAxisLength*3+9*H-i*deltaY,
     W*9 div 2,YAxisLength*3+9*H-i*deltaY);
     OutTextXY(W*5 DIV 2,YAxisLength*3+9*H-i*deltaY,
     int2str(i*10));
end; {y-axis ticks}
```

```
end;
{****************************************************************}
procedure Print_comac(comac:array5;no_nodes:integer);
var
   i,j:integer;
begin
     WriteLn(lst,'Co-ordinate Modal Assurance Criterion',#13,#10);
     WriteLn(lst,'                  ',' x-dir  ',' y-dir  ',' z-dir  ');
     for i:=1 to no_nodes do
     begin
          WriteLn(lst,'node no ',amode[1,i,1]:3:0,'    ',comac[i,1]
          :6:4,'  ',comac[i,2]:6:4,'  ',comac[i,3]:6:4);
     end;
     WriteLn(Lst);
end;
{****************************************************************}
procedure Print_MAC(mac:array4;no_amodes,no_bmodes:integer;bmode_no,
amode_no:array1;amode_freq,bmode_freq:array2);
var
   i,j:integer;
begin
     Writeln(Lst,'                              Modal Assurance Criteria',
     #10,#10);
     Writeln(Lst,'                                mode no / freq (Hz)');
     Write(Lst,'          ');
     for i:=1 to no_bmodes do
     begin
         Write(Lst,bmode_no[i]:3,'    ');
     end;
     Write(Lst,#10,#13,'            ');
     for i:=1 to no_bmodes do
     begin
         Write(Lst,bmode_freq[i]:6:2,' ');
     end;
     Write(Lst,#10,#13,'mode  freq ',#10,#13,' no   (Hz)',#13);
     for i:=1 to no_amodes do
     begin
          Write(Lst,#10,#13,amode_no[i]:3,' ',amode_freq[i]:6:2,' ');
          for j:=1 to no_bmodes do
          begin
               Write(Lst,mac[i,j]:5:1,'  ');
          end;
     end;
     WriteLn(Lst,#13);
```

```
     WriteLn(Lst,#13);
end;
{*****************************************************************}
procedure Write_MAC_File(mac:array4;no_amodes,no_bmodes:integer;
bmode_no,amode_no
:array1;amode_freq,bmode_freq:array2;name_out:string);
var
   filevar:text;
   i,j:integer;
begin
     Assign(filevar,name_out);
     ReWrite(filevar);
     Writeln(filevar,                          Modal Assurance Criteria',
     #10,#10);
     Writeln(filevar,'                             mode no / freq (Hz)');
     Write(filevar,'          ');
     for i:=1 to no_bmodes do
     begin
         Write(filevar,bmode_no[i]:3,'    ');
     end;
     Write(filevar,#10,#13,'          ');
     for i:=1 to no_bmodes do
     begin
         Write(filevar,bmode_freq[i]:6:2,' ');
     end;
     Write(filevar,#10,#13,'mode  freq ',#10,#13,' no   (Hz)',#13);
     for i:=1 to no_amodes do
     begin
          Write(filevar,#10,#13,amode_no[i]:3,' ',amode_freq[i]
          :6:2,' ');
          for j:=1 to no_bmodes do
          begin
               Write(filevar,mac[i,j]:5:1,'  ');
          end;
     end;
     Close(filevar);
end;
{*****************************************************************}
procedure Main_Menu(menu:pointer);forward;
{*****************************************************************}
procedure Option_1; {read modal data}
begin
     RestoreCrtMode;
     Assign(input,'');reset(input);
```

```
     WriteLn('Input "A" filename...');ReadLn(namea);
     WriteLn('Input "B" filename...');ReadLn(nameb);
     SetGraphMode(GraphMode);
     Status('Reading Modal Data');
     Read_Modal_Data(no_amodes,no_nodes,amode_no,amode_freq,amode,
     namea);
     Read_Modal_Data(no_bmodes,no_nodes,bmode_no,bmode_freq,bmode,
     nameb);
     normalize_Data(amode,no_amodes,no_nodes);
     normalize_Data(bmode,no_bmodes,no_nodes);
     Main_Menu(menu);
end;
{*****************************************************************}
procedure Option_2; {calculate MAC}
begin
     ClearDevice;
     Status('Calculating Modal Assurance Criteria');
     Calc_MAC(mac,no_amodes,no_bmodes,amode,bmode,no_nodes);
     Main_Menu(menu);
end;
{*****************************************************************}
procedure Option_3; {calculate COMAC}
begin
     ClearDevice;
     RestoreCrtMode;
     Write_MAC(mac,no_amodes,no_bmodes,bmode_no,amode_no,amode_freq,
     bmode_freq);
     Calc_COMAC(comac,mag_dif,no_amodes,no_bmodes,amode,bmode,
     no_nodes,lmax);
     SetGraphMode(GraphMode);
     Main_Menu(menu);
end;
{*****************************************************************}
procedure Option_4; {display MAC}
begin
     ClearDevice;
     RestoreCrtMode;
     Write_Mac(mac,no_amodes,no_bmodes,bmode_no,amode_no,amode_freq,
     bmode_freq);
     Wait;
     SetGraphMode(GraphMode);
     Main_Menu(menu);
end;
{*****************************************************************}
```

```
procedure Option_5; {display COMAC}
begin
     ClearDevice;
     RestoreCrtMode;
     Write_COMAC(comac,no_nodes);
     SetGraphMode(GraphMode);
     Main_Menu(menu);
end;
{**********************************************************************}
procedure Option_6; {display Modulus Difference graphically}
begin
     ClearDevice;
     Status('Mod Diff Plot  Hit a key to continue');
     Display_Mod_Dif(mag_dif,no_nodes,lmax,amode);
     Wait;
     Main_Menu(menu);
end;
{**********************************************************************}
procedure Option_7; {print COMAC or MAC}
label 1,3;
var
   Ch  :Char;
begin
     ClearDevice;
     Status('C=COMAC  M=MAC  R=Main menu');
1:   Ch:=ReadKey;
     Case Ch of
     'C','c' :Print_COMAC(comac,no_nodes);
     'M','m' :Print_MAC(mac,no_amodes,no_bmodes,bmode_no,amode_no,
     amode_freq,bmode_freq);
     'R','r' :goto 3;
     else goto 1;
     end;
     goto 1;
3:   Main_Menu(menu);
end;
{**********************************************************************}
procedure Option_8; {write MAC to a file}
begin
     RestoreCrtMode;
     WriteLn('Enter the name of the output file...');ReadLn(name_out);
     Write_MAC_File(mac,no_amodes,no_bmodes,bmode_no,amode_no,
     amode_freq,bmode_freq,name_out);
     SetGraphMode(GraphMode);
```

```
    Main_Menu(menu);
end;
{************************************************************************}
procedure Main_Menu(menu:pointer);
label 2;
var
   Ch :Char;
   x1 :word;
   y1 :word;
begin
    x1:=MaxX div 10;
    y1:=MaxY div 10;
    ClearDevice;
    Status('Select An Option');
    putimage(x1,y1,menu^,0);
2:  Ch:=ReadKey;
    Case Ch of
    '1' :Option_1;  {read modal data}
    '2' :Option_2;  {calculate MAC}
    '3' :Option_3;  {calculate COMAC}
    '4' :Option_4;  {display MAC}
    '5' :Option_5;  {display COMAC}
    '6' :Option_6;  {display COMAC graphically}
    '7' :Option_7;  {print COMAC}
    '8' :Option_8;  {output MAC to file}
    'q','Q' :Quit;
    else goto 2
    end;
end;
{************************************************************************}
begin {main program}
     clrscr;
     Initialize;
     MenuBlock(menu);
     Main_Menu(menu);
     closeGraph;
 end. {main program}
 {************************************************************************}
```